

Midterm Report

Design Synthesis Exercise

Group 15 - Manned Martian Aircraft

May 24, 2023

Javier Alonso Garcia	5228530	Adrian Beňo	5338514
Freek Braspenning	5291526	Joachim Bron	5259754
Pedro Coimbra Dos Santos	4682335	Sebastian Harris	5277418
Timo de Kemp	5310474	Patrick Kostelac	5238676
Thomas van de Pavoordt	5312329	Dominik Stiller	5253969

Midterm Report

Design Synthesis Exercise

by

Group 15 - Manned Martian Aircraft

May 24, 2023

Javier Alonso Garcia	5228530	Adrian Beňo	5338514
Freek Braspenning	5291526	Joachim Bron	5259754
Pedro Coimbra Dos Santos	4682335	Sebastian Harris	5277418
Timo de Kemp	5310474	Patrick Kostelac	5238676
Thomas van de Pavoordt	5312329	Dominik Stiller	5253969

Version Control			
Version	Date	Author(s)	Description
1.0	24-05-2023	All	First draft
2.0	05-06-2023	All	Final version

Project duration: April 24, 2023 – June 30, 2023

Thesis committee: Dr. A. Sciacchitano, TU Delft, tutor
Dr. S. J. Paardekooper, TU Delft, coach
Dr. ir. J. A. Pascoe, TU Delft, coach

Cover image credit: adapted from NASA/JPL-Caltech, "Daybreak at Gale Crater".

Executive Overview

Humans have been exploring Earth for centuries, and as technology advanced, this curiosity extended beyond our planet. The most promising target for making humanity interplanetary is our neighbor Mars. A manned Martian mission could be of interest in the search for life, and understanding the planet's formation, and it could form the beginning for humans as interplanetary species. Without any means of transportation on Mars, the mission would be constrained by the landing site, and the ability of the astronauts to walk. The Apollo program carried out by NASA is the only program that conducted manned space missions to other extraterrestrial bodies. The Apollo program sent people to the Moon in the 60s and 70s. To improve efficiency, the final three Apollo missions included the Lunar Roving Vehicle (LRV) which greatly extended the range of the mission. A vehicle on Mars would offer the astronauts a great increase in reach, which will improve the scientific value of the mission. This scientific gain is beneficial, especially for a mission to Mars, since the travel duration is much greater than to the Moon. This need for transport formed the mission statement:

MS: Transport two astronauts with payload quickly over a long range on Mars.

In order to reach a long-range quickly, airborne transport was considered. While a rover-like vehicle is a working proof-of-concept, their maximum speeds are rather low and are limited by terrain accessibility. The scientific gain of increasing the cruise speed and range by means of airborne transport was considered to outweigh the associated possible risks.

In combination with the client, the driving requirements were developed and subsequently frozen. The driving requirements formed the foundation for the Design Option Tree. From the Design Option Tree, three means of producing were discovered: passive lift generation by means of buoyancy, fixed lifting surfaces, and rotating lifting surfaces. These shaped the five design concepts which were viable for further development. The design concepts were: the flying wing, the biplane, the tiltrotor, the multicopter, and the airship. Illustrations for each of the concepts are given in Figure E.1.

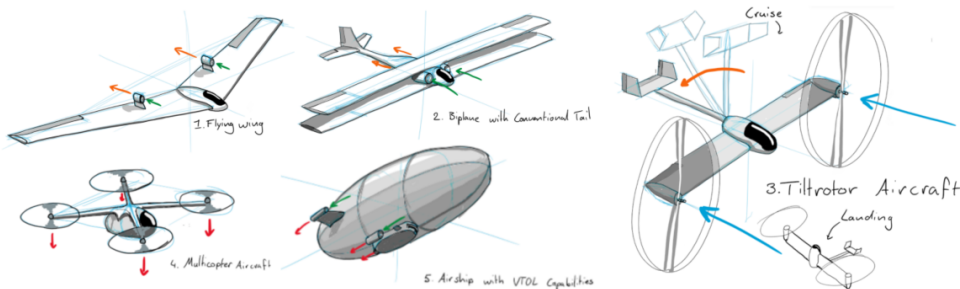


Figure E.1: Artist's impression of design concepts

E.1. Design Concepts

The design concepts were formed in accordance with the driving requirements. The preliminary sizing served the purpose of gaining an initial idea of the performance of the aircraft, size, and viability of each of the design concepts. The sizing of each of the design concepts was done in sub-teams, each aiming to produce the best possible aircraft which meets the requirements. With the preliminary sizing, assumptions had to be made. These assumptions were always documented and accounted for in either providing margin or adding to the uncertainty of the design.

E.2. Trade-off

Each of the design concepts had distinct advantages and disadvantages, for which the optimal design concept was selected. The trade-off process began by forming the criteria of interest which would differentiate each of the designs. Among a variety of potential criteria, the final selected ones were:

- **Range at 350 kg payload:** Although the minimum range is of 1000km, improvements in this department will allow for longer missions and increased mission performance.

- **Landing/Take-off distance:** Longer distances in these maneuvers lead to increased risk of colliding with rocks or other topographical features. Vertical Take-off and Landing, VTOL, would negate this risk along with removing the need for extended, flat areas of land to perform these maneuvers.
- **Sustainability:** The sustainability criterion was broken down into a rubric with 4 categories:
 - Emission of foreign molecules from the engine
 - Emission of foreign molecules from the lift system
 - Recyclability of the systems' structure
 - Use of batteries, as this technology is simultaneously applicable to Earth, sources its energy from renewable sources and, when degraded, can be used as static energy storage.
- **Feasibility:** The feasibility of the design is broken down mainly into the Technology Readiness Level, assessing at what development stage a technology is. This scale from 1 to 9 could lead to draws between designs, in which case the number of designs produced will be used to separate these draws.

In all of these criteria, the designs were scored from 0 to 4, with the latter being the highest, leading to a maximum achievable score of 16. This score was stretched to 100 to allow for comparison. The results of the trade-off can be found in Table E.1

Table E.1: Trade-off summary including criteria values and scores. The total weighted score in the last column indicates the overall goodness of the design. The tiltrotor design has the highest score and is selected.

Weight	Range at 350 kg payload [km]		Landing/take-off distance [m]		Feasibility		Sustainability		Score
	1		1		1		1		
Blended wing	1779	GREAT	2000	ACCEPTABLE	Min. TRL of 4 (Power) and <1000 existing designs	ACCEPTABLE	Emits carbon, and the energy source is not renewable	GOOD	44
Biplane aircraft	2157	EXCEPTIONAL	2000	ACCEPTABLE	Min. TRL of 4 (Power) and >1000 existing designs	GOOD	Emits carbon, and the energy source is not renewable	GOOD	56
✓ Tiltrotor	1885	GREAT	0	EXCEPTIONAL	Min. TRL of 6 (Control)	GREAT	Rotor blades are not recyclable, but uses batteries	GREAT	81
Multicopter	1270	GREAT	0	EXCEPTIONAL	Min. TRL of 4 (Power) and <1000 existing designs	ACCEPTABLE	The energy source is not renewable, and rotor blades are not recyclable	GOOD	62
Airship	480	UNACCEPTABLE	0	EXCEPTIONAL	Min. TRL of 4 (Power) and <1000 existing designs	ACCEPTABLE	Emits carbon and hydrogen, and the energy source is not renewable	ACCEPTABLE	38

E.3. Market Analysis

The costs of manned space missions are high. The cost for each of the lunar missions was 20[B]USD, and a manned Martian mission is estimated to be 150[B]USD in 2035.¹ The cost of this project is estimated to be 6.6[B]USD based on the costs of similar missions. The cost is justifiable because this mission offers the opportunity to perform several manned Martian missions in one due to the high range of the aircraft together with great in-situ recharge capabilities. The aircraft will be designed for 1500 flights of 1000km, giving the possibility of 1500 unique landing sites in one launch.

E.4. Operations and Logistics

The flow in Figure E.2 shows what needs to be done to get the aircraft flying on Mars. It also shows the operations on Mars needed for doing the operations, this includes recharging, checkouts, and maintenance. Checkouts will be done with the same equipment that is used to check and assemble the parts shipped to Mars. The system will not be dependent on regular shipments from Earth, only for big fixes or battery life problems leading to limited performance.

¹URL: <http://theconversation.com/are-astronauts-worth-tens-of-billions-of-dollars-in-extra-costs-to-go-to-mars-11> [cited 2023-06-02]

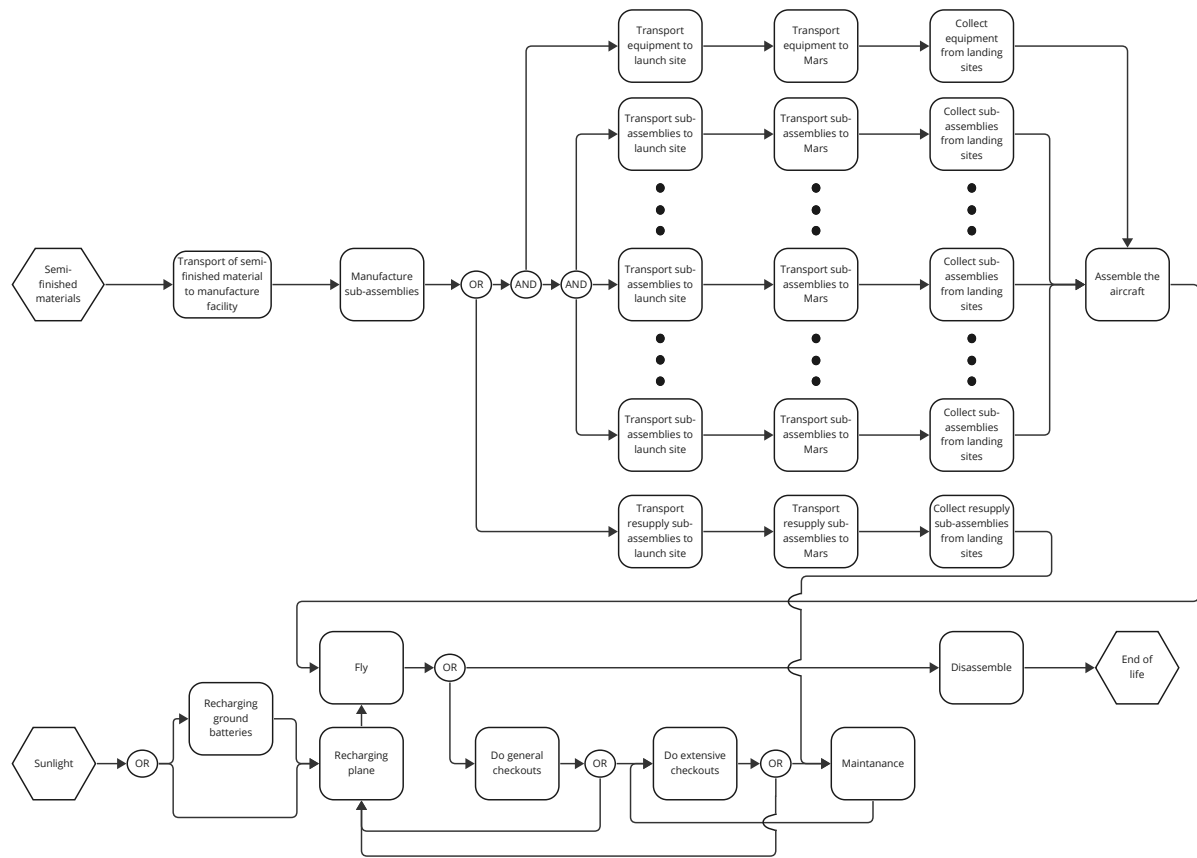


Figure E.2: Operations and logistics flow chart

E.5. Sustainable Development Strategy

The sustainable development strategy slowly moves towards a more technical and detailed approach. Whereas before sustainability was mainly focused on organizational sustainability within the group and ensuring that a definition was chosen for sustainability to comply with, the sustainability strategy now focuses on how the designs approach sustainability and how sustainability is enforced during the detailed conceptual design phase. Each concept has to result in a design that will at least fulfill the customer's requirement to only use in-situ available resources. Furthermore, during the trade-off, sustainability was also considered one of the final trade-off criteria. This meant that every concept strived for the highest score possible in this category.

For the next phase of the project, sustainability will become increasingly important. Each subsystem will have to consider sustainability and comply with the requirements set earlier. This includes but is not limited to, material choice, recyclability, manufacturing processes, assembly process, and end-of-life plan. The sustainability manager will ensure these goals are met and that the sustainability strategy is enforced.

Contents

Executive Overview	i
Abbreviations	v
1 Introduction	1
2 Organization Update	3
3 Turbojet Propulsion System	4
3.1 Propulsion system characteristics estimation	4
3.2 Verification	6
4 Preliminary Sizing	7
4.1 Design concept 1 & 2: Fixed-wing aircraft	7
4.2 Design concept 3: Tiltrotor aircraft	15
4.3 Design concept 4: Multicopter	21
4.4 Design concept 5: Airship	28
5 Verification and Validation of Design Concepts	32
5.1 Fixed-Wing Aircraft: Flying Wing & Biplane	32
5.2 Tiltrotor	34
5.3 Multicopter	39
6 Verification and Validation Plan Preliminary Design	44
6.1 Responsibilities.	44
6.2 Verification and Validation methods	44
6.3 Model Verification and Validation.	44
6.4 Product Verification and Validation.	45
7 Trade-Off	46
7.1 Methodology	46
7.2 Results.	49
8 Technical Risk Assessment	52
8.1 Methodology	52
8.2 Risks from previous reports	52
8.3 Additional risks.	53
9 Sustainable Development Strategy	56
10 Project Logic	58
10.1 Project description & development logic	58
10.2 Operations and logistics description	58
10.3 N^2 charts	59
10.4 Work Breakdown Structure	60
10.5 Work Flow Diagram	60
10.6 Gantt chart	60
Bibliography	66

Abbreviations

- AC** aerodynamic centre.
- CFRP** Carbon Fiber-Reinforced Polymer.
- CG** center of gravity.
- EEE** Equivalent Earth Engine.
- HTOL** Horizontal Take-Off and Landing.
- IQR** inter-quartile range.
- ISRU** in-situ resource utilization.
- LCA** Life Cycle Assessment.
- LCM** Life Cycle Management.
- LCT** Life Cycle Thinking.
- LRV** Lunar Roving Vehicle.
- MAC** mean aerodynamic chord.
- MTOM** maximum take-off mass.
- OEW** Operational Empty Weight.
- PD&DL** Project Description & Development Logic.
- RC** Rate of Climb.
- SFC** Specific Fuel Consumption.
- TRL** Technology Readiness Level.
- VTOL** Vertical Take-Off and Landing.
- WBS** Work Breakdown Structure.
- WF** Fuel Weight.
- WFD** Work Flow Diagram.
- WPL** Payload Weight.

Introduction

By Thomas van de Pavoordt

Private and public organizations have the goal of making humanity a multi-planetary species. Mars as our next neighbor will be our first destination possibly as soon as a decade. The first astronauts will be scientists, which will explore wide regions of the red planet. Currently, no feasible solution exists for human transportation on Mars over vast ranges and in a fast manner. While surface rovers may be adapted for human transportation, only airborne transportation will be able to meet the need of true mobility. This midterm report is the third in a series of reports to describe the conceptual design of a two-astronaut Martian aircraft.

Previously, the project plan showed the organizational aspects of this project, including task division and scheduling. The baseline report represented the first technical report of the project. It outlined the functional description of the system that should fulfill the mission and inventoried all requirements. From this, the design option tree was created, exploring every possible option of the design. The baseline report concluded with 5 different feasible options, to be further explored in this midterm report. The goal for this phase was to evaluate the options quantitatively, perform high-level estimations on the trade-off criteria, and decide on the preferred design option.

The design options remaining from the baseline report were limited to 5 concepts, summarized in a Design Option Tree (Figure 1.2). The first two options consider an aircraft with a wing, where one explores a flying wing or a tailless option and the other explores a more conventional type of aircraft with a tail. The third option considers a blend between a helicopter and an aircraft, more conventionally known as a tiltrotor. The fourth investigates the possibility of a drone-style aircraft, with multiple rotors placed around the main body. The final design option that is considered is an airship, which utilizes a lighter-than-air gas to produce lift. Artist's impressions of all design options can be seen in Figure 1.1.

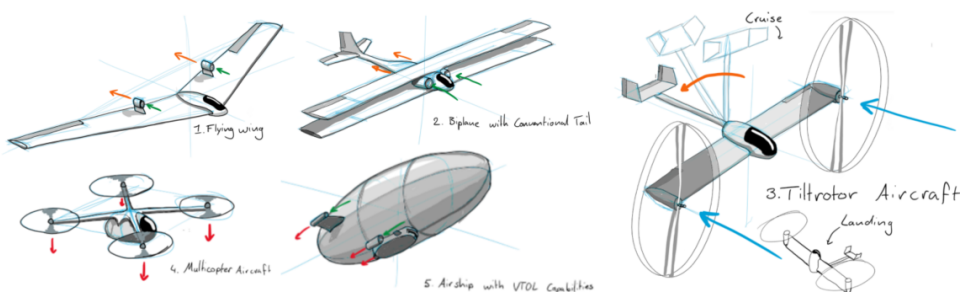
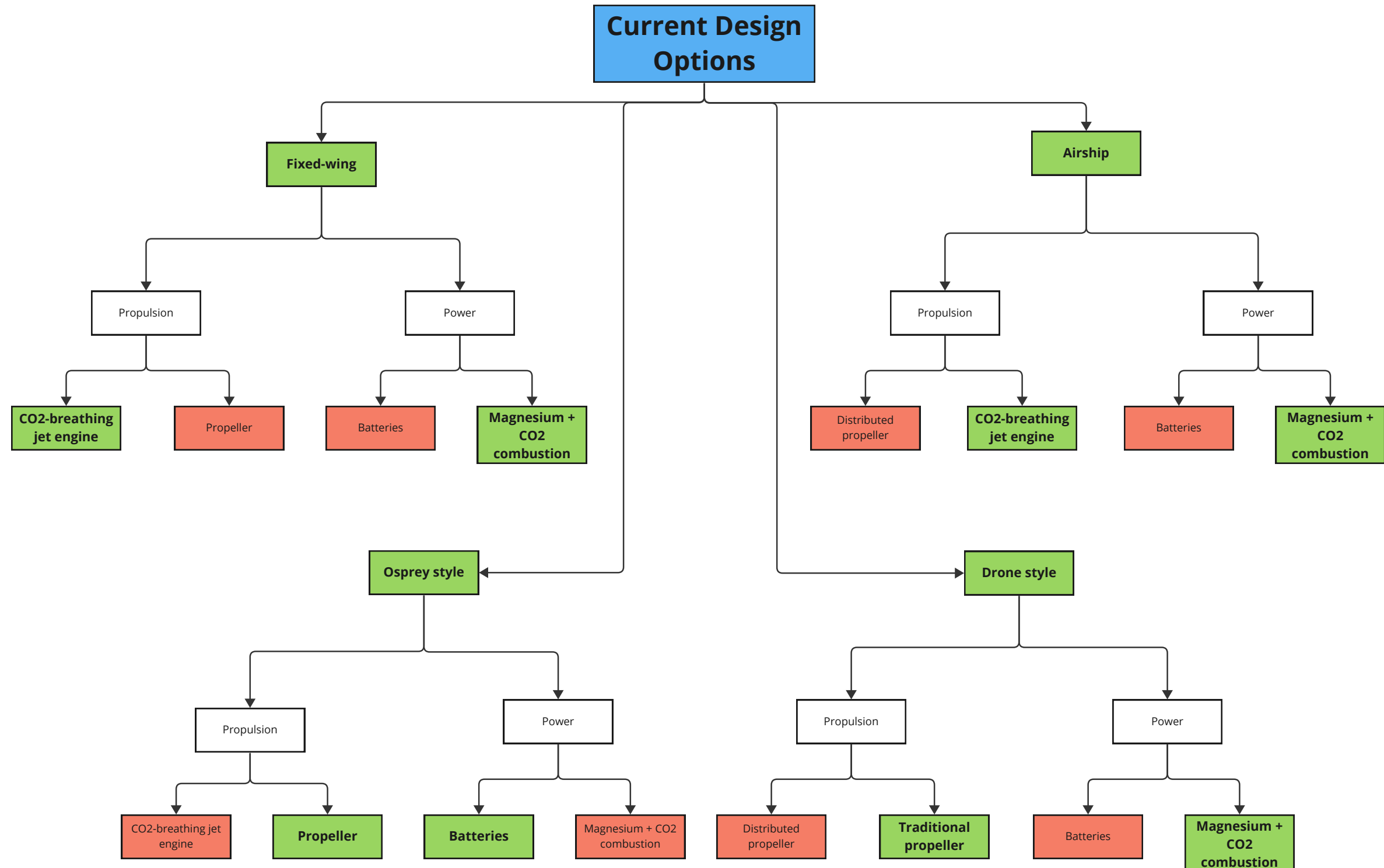


Figure 1.1: Artist's impression of design concepts.

This midterm report is structured as follows. Chapter 2 readdresses the team roles for the final phases of the project. Chapter 3 dives into a literature review on the Magnesium-CO₂ engine in preparation for the analysis of each design concept, which is done in Chapter 4. Naturally, before a trade-off between the concepts can be done, they need to be verified and validated, which is done in Chapter 5. Chapter 6 briefly describes the verification and validation plan for during and after the final design phase. Thereafter, a trade-off is performed in Chapter 7 to determine the most optimal concept. Closing off, Chapter 8 will assess the technical risks associated with the final design and proposes mitigation measures. Chapter 9 will review the sustainability approach and, finally, Chapter 10 will show the updated Project Description & Development Logic with all associated diagrams, including the N2-chart purposed to guide the iteration of the final design phase.

Source code for Chapters 4 to 7 can be found at <https://github.com/DominikStiller/tudelft-dse>.



Legend



Figure 1.2: Summary of the Design Option Tree

Organization Update

By Freek Braspenning

This chapter documents the changes in organizational and technical roles within the team, previously defined in the organogram in Figure 2.1. Table 2.1 shows the switch of graphics design manager and the sustainability manager, Table 2.2 the switch of power and hydraulics engineer and the materials engineer. The new role division is summarized in Table 2.3.

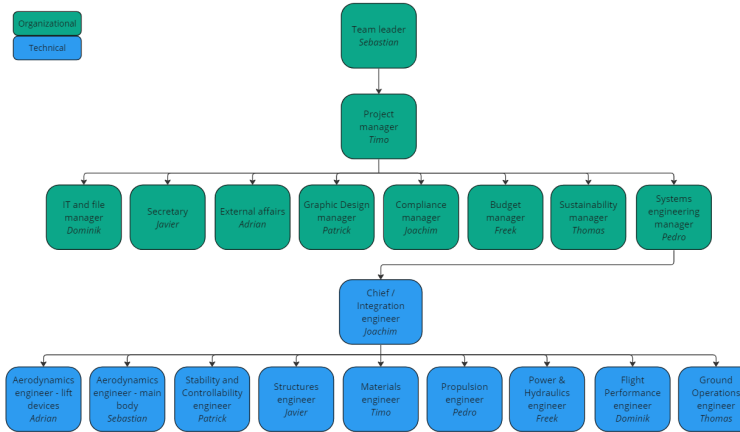


Figure 2.1: Organogram showing the pre-midterm organization of management and technical roles.

Table 2.1: Overview of the changes for organizational/ roles.

Organizational Role	Pre-midterm	Post-midterm	Description
Graphics Design Manager	Patrick	Thomas	Responsible for compliance and consistency regarding the visual elements of all deliverables. The individual shall ensure all graphics are of the same style and of high quality.
Sustainability Manager	Thomas	Patrick	Ensures that all aspects of the group's work and the development of the product are performed in a sustainable manner (e.g. using sustainable materials, being ethically sustainable, operational sustainability, etc.).

Table 2.2: Overview of the changes for technical roles.

Technical Role	Pre-midterm	Post-midterm	Description
Power and Hydraulics Engineer	Freek	Timo	Responsible for the design's power, electrical systems and hydraulics.
Materials Engineer	Timo	Freek	Responsible for the selection of suitable materials for the design's different components.

Table 2.3: Technical and organizational roles (post-midterm) for each of the team members

Name	Organizational Role	Technical Role	Deputy Technical Role
Dominik	IT and File Manager	Flight Performance Engineer	Ground Operations Engineer
Sebastian	Team Leader	Aerodynamics Engineer - Main Body	Power and Hydraulics Engineer
Freek	Budget Manager	Materials Engineer	Propulsion Engineer
Joachim	Deliverable Compliance Manager	Chief/Integration Engineer	Aerodynamics Engineer - Main Body
Javier	Secretary	Structures Engineer	Materials Engineer
Pedro	Systems Engineer	Propulsion Engineer	Chief/Integration Engineer
Adrian	External Affairs Manager	Aerodynamics Engineer - Lift Devices	Flight Performance Engineer
Patrick	Sustainability Manager	Stability and Controllability Engineer	Structures Engineer
Timo	Project Manager	Power and Hydraulics Engineer	Aerodynamics Engineer - Lift Devices
Thomas	Graphics Design Manager	Ground Operations Engineer	Stability and Controllability Engineer

Turbojet Propulsion System

By Pedro Coimbra Dos Santos

The Martian atmosphere is predominantly composed of CO₂, hence a Martian turbojet engine could use CO₂ as oxidizer. Many fuels might be possible, but a jet engine that uses magnesium as fuel and CO₂ as oxidizer is the one with the most research data available, albeit quite old data [1]. While this technology was quite in its infancy back then, some advantages and disadvantages can already be identified:

Table 3.1: Advantages and disadvantages of using a Mg-CO₂ engine.

Advantages	Disadvantages
<ul style="list-style-type: none"> • High thrust-to-weight ratio. • Martian regolith can be processed into Mg powder, which ensures ISRU. 	<ul style="list-style-type: none"> • Only small prototypes have been tested. • Jet engines typically need more maintenance than electric engines. • During tests, soft carbon flakes clogged the engine, as seen in Figure 3.2. Scaling up the prototype may mitigate this. • A carrier gas is needed to pump the Mg powder to the combustion chamber [2]. Different gases are considered in Figure 3.1.

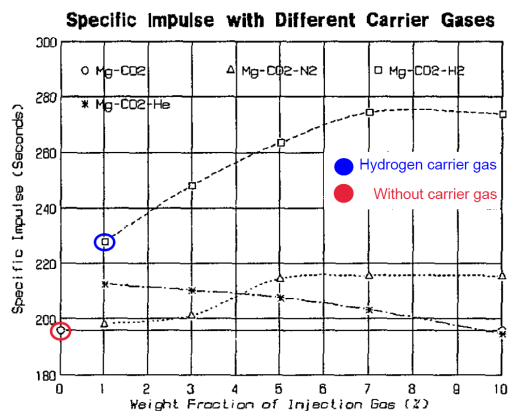


Figure 3.1: Influence of carrier gas on specific impulse [2].

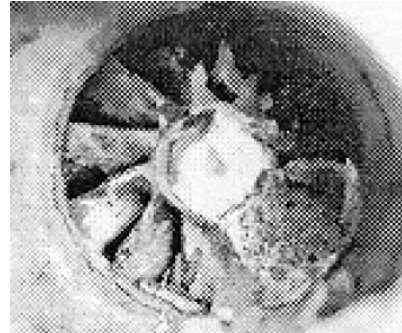


Figure 3.2: Clogged rear blades after engine test due to the accumulation of carbon flakes [2].

3.1. Propulsion system characteristics estimation

A computational tool for estimating the propulsion system's size and performance has been developed in MS Excel, with the objective of being rapidly iterable, where methods and equations found in literature have been implemented. This methodology will be discussed in this chapter.

3.1.1. Engine sizing

The first step was to size the engine itself, then use its characteristics in order to size the rest of the propulsion system.

Estimating in- and outlet size Figure 3.3 below shows the expected inlet and outlet diameter that such a Martian engine would have, depending on its maximum thrust [1]. The tool has been programmed to use this table's underlying formula in order to estimate those parameters.

Estimating fuel consumption and thrust The Specific Fuel Consumption (SFC) has been estimated with the help of Figure 3.4 from the same paper (the image has been edited by the authors of this report), where an Mg + CO₂ engine is compared with an Earth engine using JP-4 + O₂. It can be noted that,

between Mach 0.5 and 0.7, the SFC of the Martian engine is roughly 4 times larger than its Earth counterpart. Considering that the F135 (the engine that powers the F-35) is one of the most advanced turbojets there are and that its SFC is 2.5×10^{-5} kg/Ns, the Martian engine's SFC can confidently be assumed to be 10×10^{-5} kg/Ns [3]. The F135 is ideal for such comparison due to it being optimized for thrust-to-weight ratio, while also focusing on SFC. More efficient engines all have high by-pass ratios and such. Something we can not hope to use on Mars for now.

I _a [s]	80.4			
SFC [kgf/(hr·kgf)]	5.06			
F [N]	1500	1000	500	100
\dot{m}_{CO_2} [kg/s]	1.38	0.921	0.460	0.0921
D _i [cm]	83.6	68.2	48.2	21.6
D _n [cm]	78.6	64.2	45.4	20.3

Figure 3.3: Diameters and mass flow estimation for a certain thrust [1]. Where I_a is the specific thrust, SFC the specific fuel consumption, F is the thrust force, m_{CO₂} is the mass flow of CO₂ through the engine, and D_i and D_n are the inlet and outlet diameters respectively.

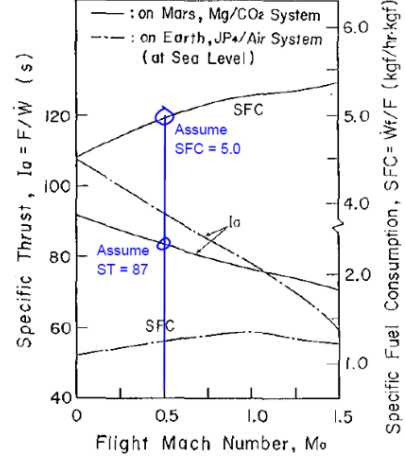


Figure 3.4: Comparison of specific thrust and specific fuel consumption of turbojet engines used in the atmospheres of Mars and the Earth as a function of Mach number adapted from [1].

By looking at Figure 3.4 again for the values between Mach 0.5 and 0.7, it can also be noted that the specific thrust of the Martian engine is roughly 4% worse than its Earth counterpart. Due to that, a thrust equally worse has been assumed.

Sizing Equivalent Earth Engine With these performance relations with respect to the Earth engine in mind, the strategy was then to translate this Martian engine into an "**Equivalent Earth Engine (EEE)**". With this strategy, classic statistical relations for Earth engines can be used for weight estimation, such that the sizing of the Martian engine is actually performed in the EEE, and the known drop in performance is then subsequently applied.

The mass for the EEE without the in- and outlet masses can be found using the statistical formula Equation (3.1) below with some adjustments for unit conversion [4]:

$$W_{lbs} = 250 + 0.175 \cdot T_{lbf} \quad W_{kg} = \left(250 + 0.175 \cdot \frac{T_{lbf}}{4.44822} \right) \cdot \frac{1}{2.20462} \quad (3.1)$$

Where W_{lbs} and W_{kg} are the estimated masses of the engine in pounds and kilograms respectively, and T_{lbf} is the maximum thrust provided by the engine in pound force. Conversion factors have been used in the second formula so that the mass is returned in kilograms.

Subsequently, the mass of the in- and outlet can then be computed and added to the mass previously found using the formula below [5]:

$$M_i = 29.26 \cdot (l_d N_i A_i^{0.5} k_{geo})^{0.7331} \quad M_n = 14.63 \cdot \frac{\pi D_n^2}{4} \quad (3.2)$$

Where M_i and M_n are the in- and outlet masses respectively, both in kilograms. Furthermore, l_d is the duct length, N_i is the number of engines, A_i is the area of the inlet, k_{geo} is a statistical factor with a value 0.5, and D_n is the outlet's diameter. All variables use standard metric units. This way, the final Martian engine total mass is obtained.

3.1.2. Main fuel tank sizing

With the SFC of 10×10^{-5} kg/Ns previously discussed, the fuel consumption is then estimated based on the flight profile phases' required thrust. With this information, the fuel tank has been sized.

Since the Mg powder does not need to be pressurized and it is relatively dense compared to liquid propellants, its tank's dimensions will be relatively small, and its thickness will be mainly constrained by thermal stresses and loads due to the Mg powder's inertia when subjected to accelerations. Due to this very low contribution to the total propulsion system's mass, it is neglected in this design phase.

3.1.3. Carrier gas storage and processing

A carrier gas is necessary to transport the magnesium powder to the interior of the engine's combustion chamber. The main idea is to use a pneumatic conveying system in order to capture Martian air mid-flight and pressurize it in a storage tank¹.

Although the gas will be obtained mid-air, a sufficiently large storage tank is needed to ensure redundancy and some flight autonomy in case the pneumatic conveying system fails. Autonomy for 20 minutes of flight is desirable, since it would give the pilots enough time to prepare an emergency landing.

By determining a weight fraction of 1% for the carrier gas flow with respect to the magnesium powder, which would be enough to ensure proper flow [2], a CO₂ storage mass required can be derived. Then, using its molar mass and corresponding volume according to the ideal gas law, the tank's volume can be estimated depending on the pressurization factor chosen. The mass of such tank is basically negligible in comparison with the rest of the propulsion system. Accounting just for cruise, the fixed wing aircraft would not need a tank heavier than 2 kg.

A cylindrical shape has been chosen for the tank for simplicity. Its thickness has been found by using the pressurization stress formula with thin-walled assumption, shown by Equations (3.3) and (3.4):

$$\sigma_L = \frac{PD}{4t} \quad (3.3)$$

$$\sigma_C = \frac{PD}{2t} \quad (3.4)$$

Where σ_L is the longitudinal stress on the cylinder's walls, σ_C is the circumferential stress on the walls, P is the pressure differential between the inside and outside of the cylinder, D is the diameter of the cylinder, and t is the thickness of the tank's walls. Furthermore, it is known that for a classic fuel tank with pressurized fuel, the circumferential stress is dominant for the required thickness.

3.2. Verification

Verifying a theoretical engine is quite hard, especially when the prototypes built have not been to scale. A good idea would be to compare its computed performance with that of Earth engines and see if this relation matches expectations described in scientific papers that report actual prototype testing.

Using the computational tool, a 125 kN thrust Martian engine ends up having a thrust-to-mass ratio of 50 N/kg. The F135-100W engine has a value of 112 N/kg for that. This means that the assumptions made during the design of the tool were probably conservative, in the sense that taking into account the challenges this engine must overcome and its increased mass and decreased efficiency compared to the F135-100W, the final product is less than half as powerful proportional to its mass and about 4 times less fuel efficient than the Earth engine that is one of the best jet engines in its category.

Better performance might still be conservatively assumed given possible future advances in this technology. But this is something that would need more thorough analysis in the next design stages if this propulsion system is selected.

¹URL: <https://www.iqsdirectory.com/articles/pneumatic-conveyor.html> [cited 2023-05-24]

Preliminary Sizing

Five concepts were deemed promising in the baseline phase. To determine which one is the best to fulfill the mission, a quantitative trade-off was performed. The preliminary sizing serves as a first-order estimation of values for trade-off criteria and is discussed in Sections 4.1 to 4.4.

To make the values comparable between designs, some common conditions were agreed upon. The design density for aerodynamic surfaces is 0.01 kg/m^3 , which is the worst-case density at zero elevation and average density at 5 km altitude. The design payload mass is 350 kg, which corresponds to two suited astronauts of 250 kg and cargo of 100 kg. The lifting capability is based on a mass of 3000 kg, the maximum take-off mass (MTOM) requirement, while the target MTOM is 2700 kg (due to a 10 % margin). If the mass is below 2700 kg, the fuel mass is increased by the difference to obtain a higher range. This range will ultimately be compared in the trade-off.

4.1. Design concept 1 & 2: Fixed-wing aircraft

By Joachim Bron

In the following subsections, the two designs for the fixed-wing aircraft will be described. These designs consist of a flying wing aircraft and a biplane aircraft. First, in Section 4.1.1, definitions of what exactly is meant with each design are given. Then, in Section 4.1.2, the preliminary sizing approach for both fixed-wing aircraft is given. For each part, this is first described qualitatively, followed by numerical results for both concepts.

4.1.1. Definitions

By Joachim Bron

For the fixed-wing aircraft concepts, two designs were chosen: a flying wing aircraft and a biplane. As opposed to the other three options, these fixed-wing concepts use Horizontal Take-Off and Landing (HTOL). The flying wing aircraft consists of a (large) wing, a fuselage to carry the astronauts and payload, and potentially some control surfaces such as elevons at the end of the wings and a rudder. It does not have a horizontal stabilizer similar to conventional aircraft, which is the main difference from the biplane design. In general, the flying wing is advantageous as it is a simpler design; on the downside, it suffers on the stability side.

The biplane design consists of two wings stacked one on top of the other. It also contains a fuselage to carry astronauts and payload. It will potentially also have control surfaces such as ailerons and a rudder. Finally, its main difference from the flying wing concept is that it has a horizontal and vertical stabilizer. The biplane design comes at a lower weight than the flying wing due to its smaller wings and smaller structural requirements.

4.1.2. Preliminary sizing and main assumptions

By Joachim Bron, Adrien Beňo, Timo de Kemp, Freek Braspenning

The preliminary sizing for the fixed-wing concepts was performed as follows:

1. Research low Reynolds' number aerodynamic effects, as these will form the basis for the wing sizing.
2. Determine the minimum needed wing area and design wing plan-form.
3. Determine the fuselage volume and dimensions.
4. Calculate the drag due to the wing and fuselage.
5. Determine needed thrust based on maximum drag.
6. Size engines and compute their weight.
7. Perform class I weight estimations and iterate
8. Size structural aspects.
9. Perform stability calculations

Aerodynamic considerations The following provides an overview of the research concerning the aerodynamics of wings at low Reynolds' numbers. The discussed aspects include the coefficient of lift, coefficient of drag, taper ratio, aspect ratio, ground effect, vortex generators, staggered wings, and unconventional wing designs, such as box wings and biplanes.

The design of conventional and flying wing concepts is highly dependent on the lift and drag coefficient of its wings as no other force in the lifting direction is readily available. Preliminary analysis shows that the approximate Reynolds' number which any of the two concepts would experience is in the order of magnitude 10^5 (see Equation (4.1)), which puts the aircraft in a regime when viscous forces contribute significantly to the performance.

$$Re = \frac{uL}{\nu} = \frac{111 \cdot 1}{5.17 \cdot 10^{-4}} = 214700 \quad (4.1)$$

This limits the research of airfoils to specialized low Reynolds' number airfoils. Selig and Guglielmo [6] provide a selection of high lift low Reynolds' number airfoils. For the preliminary design analysis, we will assume the best-performing one - S1223. This airfoil has $C_{l_{max}} \approx 2.3$, and its lift curve can be slightly adjusted by the use of vortex generators or high-lift devices. The former could potentially provide additional $\Delta C_{vg} = 0.3$ and the latter can adjust the shape of the lift curve [7].

According to the experimental and theoretical work of Traub et al. [8], the taper ratio almost does not affect the lift curve, but higher airfoil efficiency can be achieved with a straight planform. Hence, for the purposes of the preliminary research, taper ratio $\lambda = 1$ will be assumed. An aspect ratio of higher than 10 suffices to reach the saturation part of the range and endurance curves for most low Reynolds' number airfoils [9], hence this value is assumed. According to Gross and Traub [10], the ground effect does not provide any additional noticeable lift. Even worse, ground proximity increases drag. Hence, we assume that the aircraft will not make use of the ground effect.

One of the problems encountered in low Reynolds' number flight is early flow separation. One of the design options which could help mitigate this phenomenon is staggered wing design, as shown in Figure 4.1. Unfortunately, XFLR5 (which runs on XFOIL) could not analyze this configuration and hence it will be omitted from the current design stage and left for further analysis in the detailed design stage.



Figure 4.1: Staggered wing design helps to direct the flow, which would have otherwise separated, according to the shape of the wings staggered behind the first wing. [own work]

The drag estimations form one of the driving performance characteristics of the wing design as thrust is also very limited in the Martian atmosphere. "Unconventional" wing designs, such as biplane or box wing planes must be explored by default, as conventional wing designs do not provide necessary drag characteristics. The induced drag estimation is based on the induced drag formula, given in Equation (4.2). According to Somerville et al. [11], the induced drag of unconventional wings can substantially decrease drag, as shown in Figure 4.2.

$$C_{D_i} = \frac{C_L^2}{\pi AR} (1 + \delta) \quad (4.2)$$

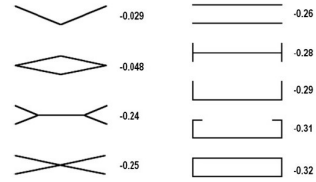


Figure 4.2: Negative induced drag factor for unconventional wings δ [11]

For structural reasons and the need for ease of assembly at the site, some of the above designs are considered unfeasible. Moreover, the need for two wings is justified by otherwise too large wing area for single wing. This leaves biplane and box configuration. For ease of assembly, we will assume $\delta = -0.26$.

Wing sizing In order to size the wings, their area was estimated first. This was done for the worst case scenario, which occurs at MTOM and stall speed. The required wing gross surface area is given by Equation (4.3)

$$S = \frac{W_{MTOM}}{C_{L_{max}} \frac{1}{2} \rho V_{stall}^2} \quad (4.3)$$

where W_{MTOM} is maximum take-off weight and V_{stall} is the stall speed. MTOM was taken from the requirements with a value of 3000 kg, $V_{stall} = 70 \text{ m/s}$ was assumed based on typical values for stall speed, and $\rho = 0.01$ was taken as it is a conservative estimate. $C_{L_{max}}$ was taken as described under "Aerodynamic considerations".

Once the necessary surface area was calculated, the wing parameters were chosen to shape the wing. The parameters that had to be chosen are the aspect ratio AR , the taper ratio λ and the quarter chord sweep $\Lambda_{0.25}$. These are mostly important for the flying wing to ensure stability, and thus are less important for the biplane (as shown in Table 4.1). From these parameters, the wingspan, root chord length, tip chord length as well as the mean aerodynamic chord (MAC) can also be calculated. Furthermore, the wing planform can be shaped and the geometry of the wing designed, which will be useful to calculate the center of gravity.

Fuselage sizing To provide space to carry the astronauts and payload, a fuselage / main body is needed. The minimum volume needed for the astronauts was found using standard cabin sizes. This cabin was assumed to be have internal dimensions of $1.5 \times 1.5 \times 1.9 \text{ m}^3$. Around this a cylindrical fuselage with a diameter of 2.5 m was fit. Using values given by Torenbeek [5], a payload density of 160 kg/m^3 was assumed. Assuming a loading efficiency of 85% and a payload mass of 100 kg, this meant that 0.9 m^3 of volume was needed for the payload. Furthermore, to enhance the aerodynamics of the fuselage, it was chosen to add parabolic-shaped nose and aft cones, which also provide more storage space in case this would be needed for other systems.

With these dimensions known, the fuselage geometry and center of gravity could be determined, and could be connected to the wing geometry. For simplicity, the fuselage designed (presented later) was the same for both the flying wing and the biplane. Its placement relative to the wing is still preliminary, but an effort was made to put it as forward as possible to ensure enough stability margin later on and make sure the aircraft center of gravity (CG) is in front of the aircraft aerodynamic centre (AC).

Weight estimations The weight was divided into the following three categories: Operational Empty Weight (OEW), Fuel Weight (WF), and Payload Weight (WPL). In the lecture slides by R. Vos et al. [12] a method is presented to determine these weights. For the OEW a statistical estimation was proposed, however, no comparable aircraft have been designed for Mars. Consequently, a different estimation method was needed to estimate the OEW. This method is the one from Torenbeek [5], which provides a way to estimate different parts of the OEW. The final part of the OEW that needed to be accounted for was the trapped oil and fuel. This was taken to be 1% of the targeted weight. Weight fractions were used to

describe the fuel used in each stage of the flight. For ground operations, take-off, climb, descent, and landing the weight fractions proposed by the slides from R. Vos et al. [?] were used. The Breguet range equation was used to determine the fuel fractions for range. Furthermore the same design mission was used as in the lecture slides, except for the loiter phase, as no loitering for an airport was necessary on Mars. Finally the payload weight is the weight of the two astronauts including their suits and an additional 100 kg were assumed to be taken to do their research.

Note that initially, the wing's weight was estimated based on the same weight loading as the Raymer aircraft [13]. After the class I weight estimation was completed, this estimate turned out to be quite accurate.

Using the weights calculated and the placing of the different components, the CG of the aircraft could be found. Regarding the weight of the fuel, the volume needed to carry it was found to be much smaller than the volume available to carry fuel in the wings, and thus the fuel was assumed to be spread along the wings as a preliminary estimate.

Engine sizing Based on the thrust required at cruise, the thrust required for the climb performance requirements, and the thrust required at TO and landing, the maximum thrust required can be found and used to size the engines. For the fixed-wing concepts, only the Mg-CO₂ engines are used, since preliminary calculations using propellers and batteries demonstrated the design to be too heavy and impossible to perform any ground operations. Using the required thrust, the engines can be sized and their weight estimated, and more accurate estimates of the fuel needed can be obtained. More details on the engine sizing can be found in Chapter 3. It was chosen to use two engines for reliability purposes, placed on the wing (the placement will be investigated further in the detailed design).

Drag estimations Drag estimations are produced based on the formulas from Torenbeek [5]. Equation (4.4) helps with conceptual understanding of the process.

$$C_D = C_{D_0} + C_{D_i} = C_{D_0} + \frac{C_L^2}{\pi e AR} \quad (4.4)$$

C_{D_0} can be further decomposed as a function of fuselage dimensions and different aerodynamic correction factors as given in Torenbeek [5]. Oswald efficiency factor is given by the results of the research on aerodynamic provided before, $e = \frac{1}{1+\delta} = 1.35$. It may seem erroneous that the Oswald efficiency factor is above 1, since elliptical wing has $e_{elliptical} = 1$. However, it is in fact correct due to the interaction between the upper and lower wings which contribute to e . Drag is then equal to:

$$D = C_D \cdot q \cdot S \quad (4.5)$$

where q and S correspond to dynamic pressure and surface area. These values are specific to the two concepts and are left to be evaluated in their respective chapters.

Structural considerations A preliminary structural analysis was performed on the wing subsystem. First a wingbox representation of the airfoil was made. The geometry of the wingbox was estimated, as seen in Figure 5.2b. From the geometry, the moments of inertia were computed by Equation (4.6), Equation (4.7), and Equation (4.8).

$$I_{xx} = \frac{ta^3 \sin^2 \beta}{12} \quad (4.6) \qquad I_{zz} = \frac{ta^3 \cos^2 \beta}{12} \quad (4.7) \qquad I_{xz} = \frac{ta^3 \sin \beta \cos \beta}{12} \quad (4.8)$$

With this the internal stresses can be computed using Equation (4.9).

$$\sigma_y = \frac{(M_x I_{zz} - M_z I_{xz}) z + (M_z I_{xx} - M_x I_{xz}) x}{I_{xx} I_{zz} - I_{xz}^2} \quad (4.9)$$

Where the moment distributions were obtained from the lift and drag distributions given by simulation results from XFLR5.

4.1.3. Performance calculations

By Freek Braspenning, Joachim Bron

Mission profile The mission profile considers the main mission (2-5) as well as possible diversions (5-8). The mission profile for both the flying wing and the biplane is given in Figure 4.3.

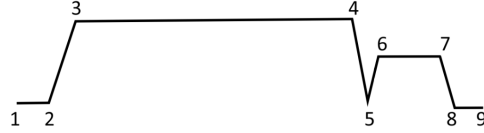


Figure 4.3: Mission profile

Thrust and maximum speed calculations After the maximum thrust has been found, the (horizontal steady) maximum speed that can be flown can be computed by using Equation (4.10):

$$T = D \implies T = C_{D0} \frac{1}{2} \rho V^2 S + \frac{W^2}{\pi A e} \frac{1}{\frac{1}{2} \rho V^2 S} \quad (4.10)$$

Equation (4.10) can be solved for V for various thrust settings until the maximum V is found. Note that the maximum speed was calculated for the worst case scenario of MTOM = 3000 kg. The maximum speed is assumed to be Mach 0.7 even if the propulsion system allows for a higher speed, to avoid compressibility effects.

Maximum altitude The theoretical maximum altitude that can be flown can crudely be approximated by finding the minimum air density at which the aircraft can fly, given by Equation (4.11):

$$\rho_{h_{max}} = \frac{W}{C_{L_{max}} \frac{1}{2} V_{h_{max}}^2 S} \quad (4.11)$$

This is computed for the highest weight. Using the density calculated and the atmospheric model of Mars, the altitude can be computed.

Cruise condition calculations The cruise condition C_L was checked to verify previous calculations and check whether the approximated values were in accordance with this calculation. The value of $C_{L_{cruise}}$ was found using Equation (4.12):

$$C_{L_{cruise}} = \frac{MTOM \cdot g_{mars}}{q_\infty S} \quad (4.12)$$

where q_∞ is the free-stream dynamic pressure. Finally, the drag at cruise condition is needed to determine how much thrust is required.

Climb performance The aircraft needs to achieve a required climb angle in order to avoid obstacles or get out of a crater. Based on statistical data of Martian craters' dimensions, it was decided that the aircraft shall have a minimum climb angle of $\gamma = 30^\circ$. The amount of thrust required to meet this minimum climb angle is then determined using Equation (4.13):

$$T = D + W \sin \gamma \quad (4.13)$$

where W is the maximum take-off weight. Based on this, the maximum Rate of Climb (RC) can be found using Equation (4.14).

$$RC = \frac{TV - DV}{W} \quad (4.14)$$

Take-off and landing performance Take-off and landing is mostly determined by the take-off and landing distance. For take-off, the thrust required is given by Equation (4.15):

$$T = \frac{V_{LOF}^2 W}{2d_{TO}} + \bar{D} + D_g \quad (4.15)$$

where $V_{LOF} = 1.05 V_{stall}$ is the liftoff speed, d_{TO} is the take-off distance, and W is the maximum take-off weight. $\bar{D} = C_{D,TO} \frac{1}{2} \rho \bar{V}^2 S$ is the average aerodynamic drag during take-off and $D_g = \mu(W - \bar{L})$ is the drag due to the ground friction. The landing performance was always found to be less critical than take-off performance, hence we only present the take-off related equation.

4.1.4. Structural considerations

By Freek Braspenning, Timo de Kemp

Flying wing structural performance The aerodynamic loads exerted on the wing are given in Figure 4.4. The loads were estimated by simulation results from XFLR5. The wingbox shape is assumed to approximately follow the airfoil, as shown in Figure 4.5b. The maximum tensile stress in the wingbox occurs at the root and is equal to 282.5 MPa. This occurs at point 4, as shown in Figure 4.5a. The maximum compressive stress in the wingbox occurs at the root and is equal to 282.0 MPa. This occurs at point 2, as shown in Figure 4.5a.

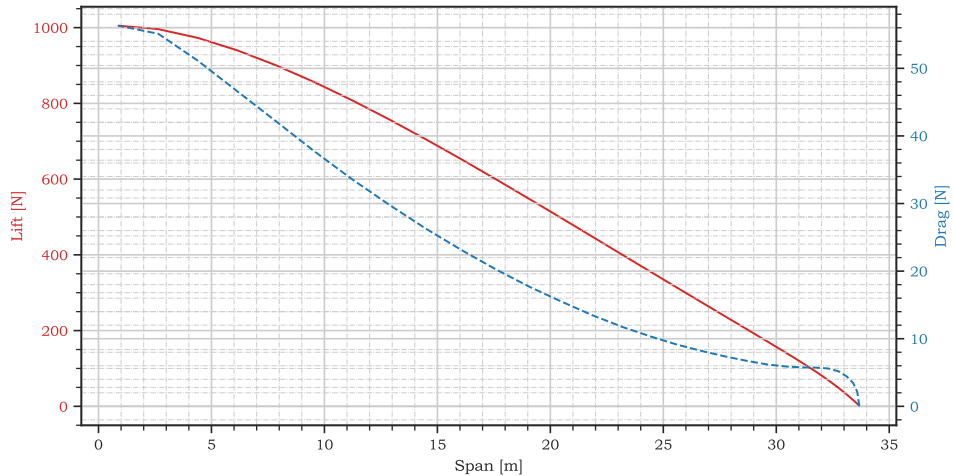
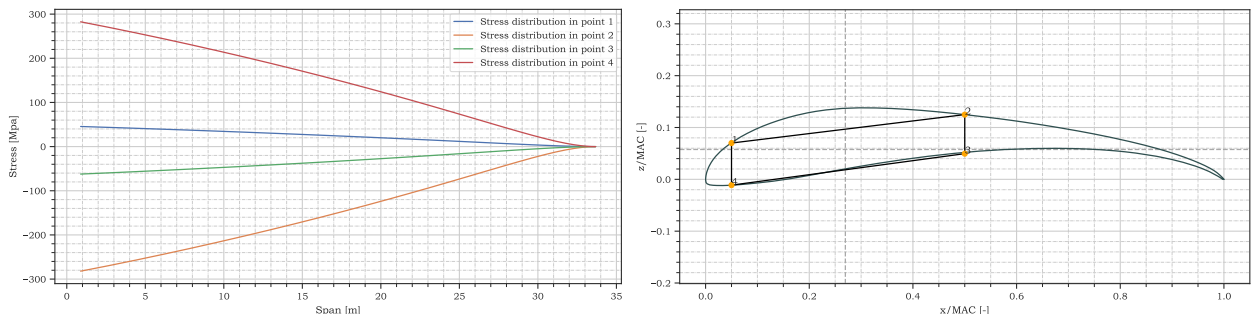


Figure 4.4: Applied loads on the wing of the flying wing



(a) Internal stress distribution of the flying wing wingbox

(b) The wingbox in the airfoil

Figure 4.5: Internal stress distribution in the wingbox

Biplane structural performance The aerodynamic loads exerted on the main wings are given in Figure 4.6. The loads were estimated by simulation results from XFLR5. The wingbox shape is assumed to approximately follow the airfoil, as shown in Figure 4.7b. The maximum tensile stress in the wingbox occurs at the root of the bottom left stringer, see point 4 in Figure 4.7b, and is equal to 283.3 MPa, as shown in Figure 4.7a. The maximum compressive stress in the wingbox occurs at the root of the top right stringer, see point 2 in Figure 4.7b, and is equal to 282.6 MPa, as shown in Figure 4.7a. It should be noted that the average applied loads on the wings of the flying wing are higher than the average applied loads on the wings of the biplane, yet the maximum tensile stresses are approximately the same. This is due to their respective wing planform.

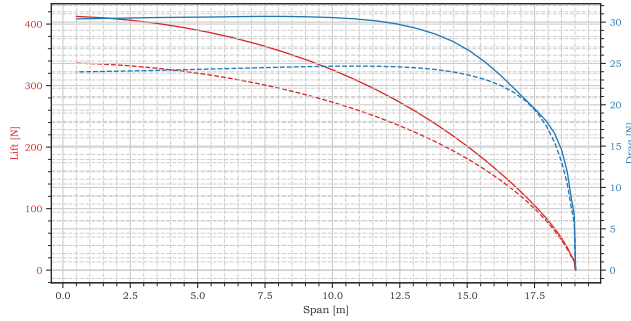


Figure 4.6: Applied loads on the wings of the biplane

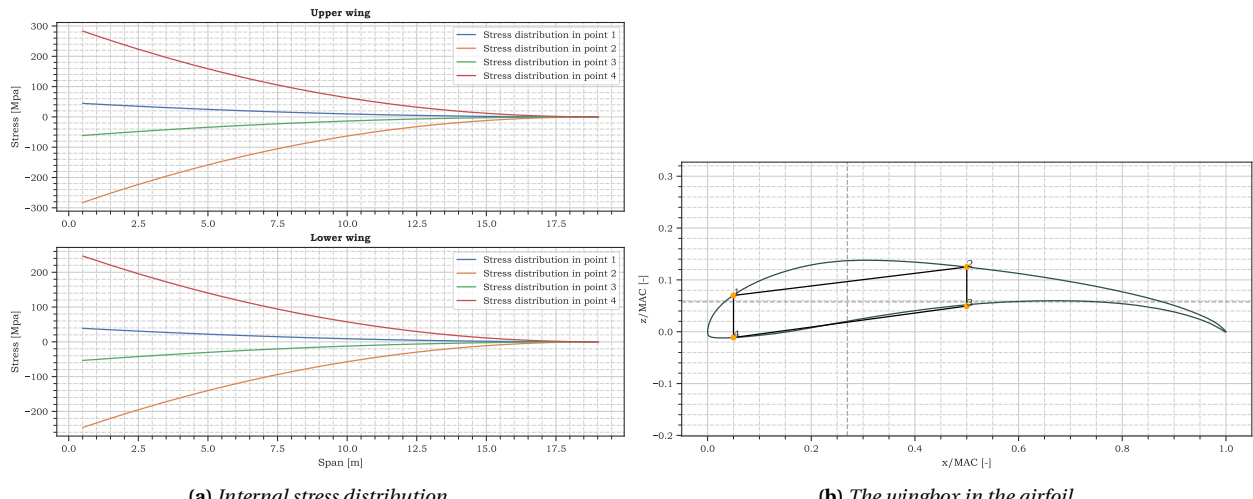


Figure 4.7: Internal stress distribution in the wingbox

4.1.5. Stability and control

By Joachim Bron and Adrian Beňo

Flying wing stability Stability is a common problem among flying wings. Commonly, reflex airfoils or large sweep angles are needed to achieve stability. Here, a simple stability model was set up to check if stability can be achieved using elevons and an arbitrary airfoil.

The flying wing was modeled by a CG, in which the weight (W) acts, an AC (behind the CG for stability) in which the moment M_{ac} and normal force N of the wing and aircraft act and the elevon's AC, where the elevon's normal force N_e acts. The distances between these different points are given in Figure 4.8.

Setting up moment and force equilibrium and assuming steady flight, the following equations were obtained:

$$M_{cg} = 0 \implies M_{ac} - N(x_{ac} - x_w) - N_e l_e = 0 \quad (4.16)$$

$$F_y = 0 \implies N = W \quad (4.17)$$

Both can be rewritten as:

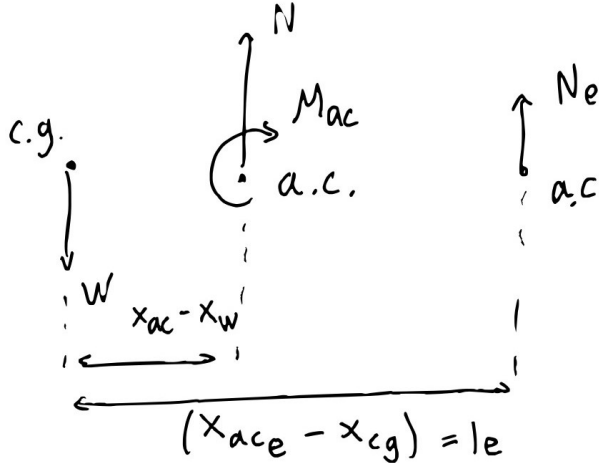


Figure 4.8: FBD of simplified flying wing

$$C_{m_{ac}} - C_N \frac{x_{ac} - x_w}{\bar{c}} - C_{N_e} \left(\frac{V_e}{V} \right)^2 \frac{S_e l_e}{S \bar{c}} = 0 \quad (4.18)$$

$$C_N = \frac{W}{\frac{1}{2} \rho V^2 S} \quad (4.19)$$

Assuming $V_e/V = 1$, the first equation can be rewritten as:

$$C_{N_e} \frac{S_e l_e}{S \bar{c}} = C_{m_{ac}} - C_N \frac{x_{ac} - x_w}{\bar{c}} \quad (4.20)$$

This equation was then used to size the elevons and ensure moment equilibrium. Later on, a deeper analysis can be performed to investigate static stability using control derivatives.

Biplane stability The approximate size and weight of the horizontal tail had to be approximated based on the stability constraints. One additional constraining factor was the need for symmetrical airfoil. Unfortunately, these have lowered maximum coefficient of lift. For the purposes of the preliminary design, NACA0012 airfoil was assumed. The force needed to be exerted by horizontal tail is given in Equation (4.21). The surface area required is then given by Equation (4.22). The horizontal tail surface area was evaluated for take-off, cruise and landing conditions separately, in order to find the limiting size. The weight of the horizontal tail was estimated using formula from [5], given in Equation (4.23).

$$N_h \approx \frac{1}{l_h} \left(C_{m_{ac}} \frac{1}{2} \rho V^2 S_c + W(x_{cg} - x_w) \right) \quad (4.21)$$

$$S_h = \frac{N_h}{C_{l_h} \frac{1}{2} \rho V^2} \quad (4.22)$$

$$M_t = 0.64(n_{ult} S_{tail}^2)^{0.75} \quad (4.23)$$

4.1.6. Preliminary design concept 1 summary: Flying wing

By Adrian Beňo and Joachim Bron

The defining characteristics of the flying wing concept is that it lacks a tail. This reduces the total drag and decreases the amount of fuel needed, which makes the concept more sustainable. At the same time, the area of the wing causes high wingspan and high average structural loads, which require more material. Furthermore, the geometry of the flying wing makes it hard to maneuver close to the ground. The defining design characteristics regarding the flying wing concept can be found in Table 4.1. The planform of the flying wing can be seen in Figure 4.9.

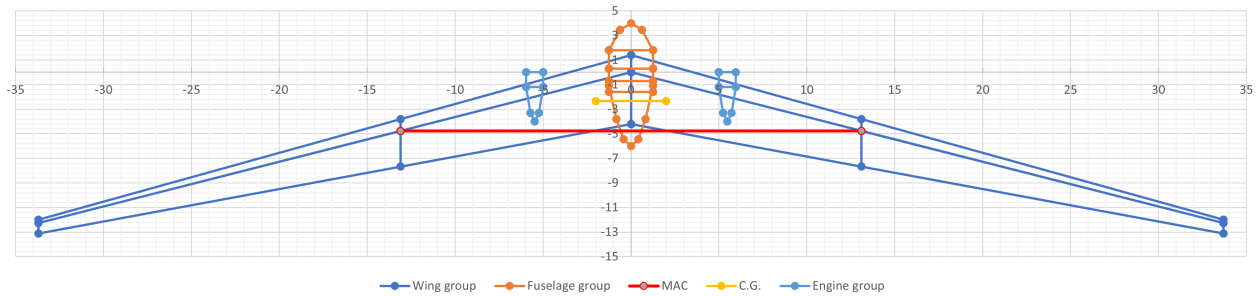


Figure 4.9: Top view of the flying wing concept

4.1.7. Preliminary design concept 2 summary: Biplane

By Adrian Beňo and Joachim Bron

The defining characteristic of the biplane concept is an Oswald efficiency factor greater than 1, which substantially reduces the induced drag. Moreover, the biplane design distributes the necessary wing area over two wings and thus, effectively reduces the wingspan by a factor of 2. As mentioned before, this does not decrease the maximum stress in the wing, but the stress distribution over the wingspan results in lower structural loads on average, decreasing degradation due to fatigue. It is also easier to maneuver due to its geometry. The defining design characteristics regarding the biplane concept can be found in Table 4.1. The planform of the biplane can be seen in Figure 4.10.

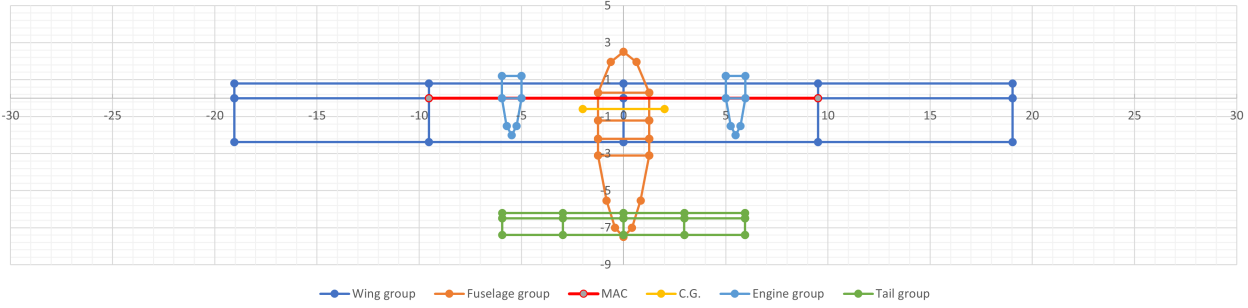


Figure 4.10: Top view of the biplane concept

Table 4.1: Selection of the defining parameters of the flying wing and biplane concepts.

Parameter	Flying wing	Biplane	Parameter	Flying wing	Biplane
$C_{l_{max}}$	2	2	V_{cruise} [m/s]	111	111
$C_{l_{cruise}}$	0.79	0.79	MAC [m]	3.37	3.17
$C_{l_{takeoff}}$	1.8	1.8	f_d [m]	2.5	2.5
$C_{l_{landing}}$	2	2	f_l [m]	10	10
λ	0.2	1	OEW [N]	6270	5314
AR	20	12	WF [N]	2318	3355
e	0.75	1.35	WP [N]	1298	1298
C_{D_0}	0.034	0.034	V_{max} [m/s]	154	154
D [N]	478	483	RC [m/s]	32.18	32.69
S [m^2]	227	227	e_d [m]	0.96	0.96
V_{stall} [m/s]	70	70	e_l [m]	1.2	1.2
b [m]	67.4	38.1	T_{max} [N]	4550	4539
W_{engine} [N]	816	712	c_{root} [m]	5.61	3.17
$\lambda_{1/4} [deg]$	20	0	c_{tip} [m]	1.12	3.17
$d_{take-off}$ [m]	2000	2000	$d_{landing}$ [m]	1949	1960
R at 350 kg payload [m]	1779	2157	-	-	-

4.2. Design concept 3: Tiltrotor aircraft

By Sebastian Harris, Javier Alonso

The tiltrotor configuration requires the combination of a wing and the lift capacity of a rotorcraft. Regarding the rotor configuration, it was chosen to use a set of counter-rotating rotors at the tip of each wing in order to reduce the required rotor radius for take-off.

4.2.1. Main Rotor Sizing

By Sebastian Harris

The process for sizing the main rotor is based on the combination of momentum and blade element theory, as detailed in the book *multicopter Performance, Stability, and Control* by Prouty [14]. The process requires a blade number, blade radius, chord, twist, cutout, airfoil data, and the relevant test conditions

as input. The initial conditions were set to contain the number of blades per rotor, determined to be 6, the chord, calculated as a twentieth of the radius, the twist, assumed to be ideal, the blade cutout, determined to be the chord divided by the radius, and finally the data of the airfoil in this case S1223. The rotation of the chord is calculated to always lead to a tip speed of Mach 0.92.

The blade is separated into up to 15 elements along the radius, each of equal length. For each of these elements, the chord is calculated as well as the local Mach number. The latter is done by the following relation, also leading to the lift curve slope:

$$M_{local} = (r/R) \left(\frac{\Omega R}{V_{sound}} \right) [14] \quad a_{local} = \frac{a}{\sqrt{1 - M_{local}^2}} [14]$$

Subsequently, the local twist of the blade can be calculated for each element boundary as $\Delta\theta$. Thus, the pitch at the blade element is calculated as

$$\theta = \theta_0 + \Delta\theta - \alpha_0 [14]$$

Where α_0 is the zero lift angle of attack for the airfoil selected.

Due to the twist and rotation of the blade, each element has a separate angle with respect to the flow, part of which is called the local inflow angle. The local inflow depends on the twist amongst other parameters and is calculated as

$$\frac{v_1}{\Omega r} = \frac{ab\frac{c}{R}}{16\pi\frac{r}{R}} \left[-1 + \sqrt{1 + \frac{32\pi\theta\frac{r}{R}}{ab\frac{c}{R}}} \right] [14]$$

Finally, the local angle of attack can be calculated as $\alpha = \theta - \arctan \frac{v_1}{\Omega r}$. For the sake of design simplicity in these first stages, it was assumed the local angle of attack would be constant at 6°, a value that matches that of rotorcraft on Earth. [14].

Given this angle of attack, the local values for lift and drag coefficients can be calculated using the previously mentioned lift curve slopes.

With these values in mind, the thrust coefficient can be calculated by first determining the running thrust loading, followed by integrating over the length of the blade, starting from the cutoff point in order to provide the thrust coefficient without tip loss:

$$\frac{dC_T}{d\frac{r}{R}} = \frac{b(\frac{r}{R})^2 \frac{c}{R} c_l}{2\pi} [14] \quad C_{T_{notiploss}} = \int_{x_0}^1 \frac{dC_T}{d\frac{r}{R}} d\frac{r}{R} [14]$$

The tip loss factor, B, is calculated, from which the final thrust coefficient follows:

$$B = 1 - \frac{\sqrt{2C_{T_{notiploss}}}}{b} [14] \quad C_T = C_{T_{notiploss}} - \int_B^1 \frac{dC_T}{d\frac{r}{R}} d\frac{r}{R} [14]$$

In parallel, the required torque for the blade to rotate can be found via the running profile torque, calculated as follows:

$$\frac{dC_{Q_0}}{d\frac{r}{R}} = \frac{b(\frac{r}{R})^3 \frac{c}{R} c_d}{2\pi} [14] \quad C_{Q_0} = \int_0^1 \frac{dC_{Q_0}}{d\frac{r}{R}} d\frac{r}{R} [14]$$

Similarly, the running-induced torque loading:

$$\frac{dC_{Q_i}}{d\frac{r}{R}} = \frac{b(\frac{r}{R})^3 \frac{c}{R} c_l \frac{v_1}{\Omega r}}{2\pi} [14] \quad C_{Q_i} = \int_{x_0}^B \frac{dC_{Q_i}}{d\frac{r}{R}} d\frac{r}{R} [14]$$

The disk loading of the rotor can be calculated as:

$$D.L. = C_T \rho (\Omega R)^2 [14]$$

Finally, the thrust generated by the rotor can be calculated as:

$$T = \rho A (\Omega R)^2 C_T [14]$$

In order to understand the power required by the rotor, the thrust and area of the rotor can be combined to find:

$$P = T \sqrt{\frac{T}{2\rho A}} [14] \quad (4.24)$$

The required radius can be found for a specified mass by iterating this process until the lift produced is sufficient.

The result of the iteration leads to the following values for both rotor and power sizing:

- Rotor Radius: 10.4 [m]
- Rotor Thrust: 2789.72 [N]
- Power Required per Rotor: 56522 [W]

It is important to note that this value of power applies for maximum thrust during vertical take-off, during cruise, and other flight states, this value will be lower due to the action of the wing.

To minimize the mass of the rotor, a study was conducted relating the weight of the rotor with respect to its loading. This led to the calculation of the lowest possible rotor mass. As a first estimate, a rotor fill of 9% was used, leading to a mass of 265 kg per set of rotors.

4.2.2. Geometry sizing

By Javier Alonso

The sizing of the wing is set up in order to minimize wing area when in cruise. This is done by first determining the maximum mass to be lifted, in this case, 3000 kg. Next, the lifting coefficient was determined to be the same as that of the rotor. That is, the value of the S1223 airfoil at an angle of attack of 6°, which is 1.6. As such, the required surface area can be calculated as:

$$S = \frac{MTOMg_{mars}}{C_L \frac{1}{2} \rho V_{cruise}^2} [15]$$

The total wing area required is 112.7 m². Regarding the shape of this wing, two factors determine its size. The first is the rotors having enough space to rotate without interfering with each other. As a first estimate, it was determined that one rotor radius of space between the tips would be sufficient, therefore, the wingspan would have to be three times the rotor radius. Furthermore, the low viscosity of the Martian atmosphere leads to a requirement for an aspect ratio to be larger than 10, as mentioned in Section 4.1. From the surface area, the induced drag can be calculated via the formula:

$$C_{D_{wing}} = C_{D_0} + \frac{C_L^2}{\pi AR_e} [15]$$

Additionally, the drag of the fuselage, engines and undercarriage can be calculated through statistical relations as described by Torenbeek [5].

The first step was to determine the relevant dimensions, for this, the cockpit was determined to have a length of 1.78 m as this value is average in aircraft[5]. Next, the fuselage was assumed to be a cylinder of 1.5 m diameter. Although this value does not allow for the astronauts to stand, it should nonetheless allow for ample operating room. Finally, to the length of the cockpit, the wing chord was added in order to ensure sufficient structural load paths. As there is no need for the fuselage to extend all the way back, the tail was assumed to be connected via a set of booms to the fuselage, thus reducing the fuselage's total length. The relationships for the drag of the fuselage and engines can be seen below:

$$C_{D_{fuselage}} = 0.0031 l_{fuselage} (h_{fuselage} + b_{fuselage}) [5] \quad C_{D_{engine}} = 2 \cdot 0.08 \cdot 0.07 [5]$$

For the engines, the value was hard to estimate as the shape of the engines is not yet known. However, the drag was still calculated not to neglect the contribution. Regarding the undercarriage, the exact design was not yet known, leading to an assumption the main gear would retract into the streamlined fairing, which results in a correction factor: $r_{uc} = 1.08$ [5].

Next, the drag must be corrected according to the Reynolds number around the fuselage, leading to a correction factor:

$$r_{Re} = 47 \left(\frac{V_{cruise} l_{fuselage}}{\mu_{cruise}} \right)^{-0.2} \quad [5]$$

Finally, the tailplane correction factor is $r_t = 1.24$ [5]. Combining these factors leads to a drag coefficient, after which the total drag is calculated.

$$C_{D_0} = r_{Re} \cdot r_{uc} \cdot \frac{r_t (C_{D_fuselage} + C_{D_{engine}})}{S_{wing}} \quad [5] \quad D = \frac{1}{2} \rho S_{wing} V_{wing} (C_{D_0} + C_{D_{wing}})$$

During the cruise, this drag must be counteracted by thrust, thus providing a value for cruise thrust, T_{cruise} , which, after implementing all the formulas above, comes to a value of 739.5 N.

4.2.3. Power budget

By Javier Alonso

A different power will be required during cruise and vertical climb. During cruise, the power output of the propeller can be calculated by multiplying the thrust required during cruise and the cruise velocity, which lead to a required power of:

$$P = T_{cruise} V_{cruise} = 739.5 \text{ N} \cdot 112 \text{ m/s} = 82.163 \text{ kW} \quad (4.25)$$

The minimum cruise time required, stemming from the cruise speed and minimum range, was 2.5 hours. This value was then multiplied to the power obtained in Equation (4.25) in order to obtain the energy that needs to be stored in the aircraft for cruise. Two significantly different values can be found for electrical and thermal engines since the former have an efficiency of up to 95% but modern thermal engines have an efficiency of just 50%¹.

As mentioned before, with a thrust of 739.5 N, the power output of the engines will be 82.163 kW. The situation during lift-off and landing are very different, however. The required thrust in these scenario was 11.13 kN; therefore, the total power output could be calculated using Equation 4.24 which yielded a value of 226.1 kW. As an initial estimate of take-off procedures, the time for this maneuver was determined to be five minutes.

Thus, the values of energy and power consumption were calculated by multiplying the power by the time during which the power is applied. The results of this can be seen in Table 4.2.

Table 4.2: Energy and Power consumption at various maneuvers

Maneuver	Power [W]	Energy[Wh]
Take-off	226088	18840.7
Cruise	82163.7	205409.3

By using an energy density of 437 Wh/kg, a power density of 1317 W/kg [16] and applying a 30% margin to account for battery degradation, the total battery mass comes up to 878 kg.

To increase the range and the ability to fly to remote areas, the installation of solar panels on the wing's surface would decrease the power consumption during flight as well as allow recharge once landed. The solar irradiance on Mars is 586.2 W/m² ², and the available wing area is 112.7 m². Using a total area of 56 m² the average collecting power would be 32.8 kW. Space-degree solar panels have an efficiency of 34% ³. Therefore, they would be able to provide 11.1 kW with a 90° angle of incidence and maximum irradiance, which represents around an eighth of the power consumption in cruise.

¹URL: <https://simpleflying.com/electric-aircraft-power-chain-efficiency-guide/> [cited 2023-05-16]

²URL: <https://mars.nasa.gov/all-about-mars/facts/> [cited 2023-05-01]

³URL: <https://www.spectrolab.com/DataSheets/Panel/panels.pdf> [cited 2023-05-24]

4.2.4. Weight Calculation

By Sebastian Harris

Once certain dimensions of the aircraft were known, it was possible to determine the weight of the relevant structures along with more detailed dimensions of the aircraft. The formulas used were sourced from statistical relations by Torenbeek [5].

The first step was to determine the dimensions of the fuselage. The cockpit area was set to have a length of 1.78 m [5]. The fuselage was assumed to be cylindrical in order to facilitate calculations. For the cross-sectional dimensions of the fuselage, the diameter of the fuselage was set to be 1.5 m based on the 0.75 m distance between seats specified by Torenbeek [5]. The length of the fuselage was set to be the length of the cockpit plus the length of the chord.

With these dimensions the value of the wing group can be calculated with the following relation:

$$\frac{m_{wing}}{m_{TO}} = 4.910^{-3} b^{0.75} \left(1 + \sqrt{\frac{1.905}{b}} N_{ult}^{0.55} \frac{\frac{b}{c}}{S_{wing}} \right)^{0.3} \quad [5]$$

Additionally, the use of a wing brace, a structure relieving the wing from its own weight, was used to further reduce this weight by 30%.

The tail of the aircraft was then sized. In order to provide some first estimates, it was determined the rear tail would be sized as:

$$S_{tail} = \frac{S_{wing} c}{1.5 R} \quad [5] \quad m_{tail} = 0.64 (N_{ult} S_{tail}^2)^{0.75} \quad [5]$$

Next, the fuselage weight was calculated. This is dependent on the gross surface of the fuselage and the dive speed. The dive speed was determined to be 110% of the cruise speed as the cruise speed should be the aircraft's maximum speed.

For the gross fuselage area, it was assumed to be a cylinder capped by a half sphere at each end, leading to the calculation as:

$$S_{gross} = 4\pi r^2 + 2\pi r * l_f \quad [5] \quad m_{fus} = 0.23 \sqrt{\frac{V_{dive} l_t}{(b_f + h_f)}} S_{gross}^{1.2} \quad [5]$$

The total weight of the aircraft was then be used to determine the weight for the next iteration, calculated as follows:

$$m_{total} = m_{wing} + m_{tail} + m_{rotor} + m_{payload} (+m_{solar})$$

Finally, the volume of the aircraft could be calculated based on these dimensions. This volume was divided into the volume of the wings, the rotor blades, the fuselage and the tail. In addition to this, a safety factor of 50% was added to account for elements needed for the assembly such as the tail pole.

The fuselage was sub-divided into a conical cockpit and a cylindrical fuselage section. It's volume can be calculated as shown in Equation (4.26).

$$V_f = \frac{1}{3} l_{cockpit} \left(\frac{f_w}{2} \right)^2 \quad (4.26)$$

In order to size the wings, the cross-sectional area of the airfoil was computed using Python and multiplied by the wingspan. The same procedure was applied to the rotor blades.

Finally, the density of the tail was assumed to be the same as the wing, such that the volume was obtained by multiplying the wing volume by the mass fraction.

4.2.5. Performance

By Sebastian Harris

The performance of the design was mainly calculated based on RC and the payload-range diagram. Regarding RC, this was calculated at cruise, allowing for a better understanding of performance in operational capabilities.

When calculating RC, the first step was to determine the climb angle during the cruise. This angle depends on the maximum thrust available during the cruise. This is done by calculating it from the power relation:

$$T_{max} = \frac{P_{available}}{\sqrt{\frac{1}{2\rho\pi R^2}}}^{\frac{2}{3}}$$

From which the climb angle was found, in turn leading to the rate of climb.

$$\gamma = \arctan\left(\frac{T}{m_{total}g_{mars}} - \frac{C_l}{C_d}\right) \quad ROC_{cruise} = V_{cruise} \sin \gamma$$

Regarding the vertical configuration, the climb performance was dependent on the difference in horsepower between the maximum performance and that required to hover. As the maximum power and hover power are known, the rate of climb could be found by solving the following equation for rate of climb.

$$\Delta hp = \frac{MTOM}{550} \left(\frac{V_{climb}}{2} + \sqrt{\frac{V_{climb}^2}{2} + V_{induced,hover}^2} - V_{induced,hover} \right)$$

It must be mentioned that the formula above is in US customary units, and as such the values must be converted. The result is an iteration on rate of climb until the difference in horsepower is smaller than 1%.

Table 4.3: Climb rate in the two main configurations of the tiltrotor

Configuration	Rate of Climb [m/s]	Climb Angle [deg]
Aircraft in cruise	62.5	34.24
Rotorcraft	2.3	90

Regarding the Payload range diagram, the difference between the design mass and the calculated mass from the weight estimation was made use of. This difference would be either filled by batteries or by payload. This process is repeated for a set of payload masses and calculates the range, leading to Figure 4.11.

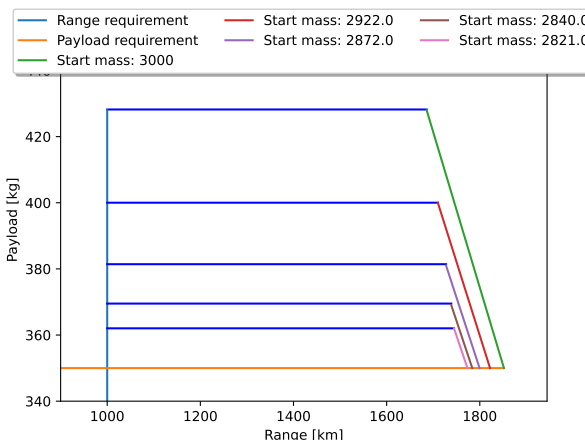


Figure 4.11: Payload to Range diagram of the Tiltrotor design

4.3. Design concept 4: Multicopter

By Patrick Kostelac, Dominik Stiller

We define a multicopter as a rotorcraft with fixed rotors and no additional lifting surfaces, unlike a tiltrotor aircraft. This concept is the only one that is flight-proven on Mars through Ingenuity, a 1.8-kg demonstrator with a coaxial rotor. The multicopter design consists of a helicopter-like fuselage connected to the rotors via spars. Key challenges include the creation of sufficient lift to hover in the thin Martian atmosphere and preventing supersonic tip speeds.

A multicopter is characterized by the number of rotors, blades per rotor, rotation speed, and blade properties. Blade properties include the radius, chord, airfoil, and twist distribution. Rotors can be coaxial, meaning two counterrotating rotors stacked on each other but driven by the same engine.

4.3.1. Preliminary sizing

By Dominik Stiller, Patric Kostelac

The preliminary sizing approach for multicopters is as follows:

1. Enumerate radius–rotation speed combination for a range of numbers of blades and rotors.
2. Find the combination with the minimal blade radius such that the vehicle weight can be sustained in hover and the tip Mach number is below 0.85.
3. Size the spars for each combination such that they can sustain rotor thrust and provide sufficient rotor clearance.
4. Estimate the vehicle mass for each combination using statistical and physical approaches.
5. Choose the lightest combination and proceed with detailed sizing.

To simplify the preliminary sizing, we make a range of assumptions:

- Hovering during take-off/landing is the critical sizing condition since forward flight helps with lift.
- The design lift should sustain the mass of 3000 kg.
- The tip speed should not exceed $M = 0.85$, similarly to [17].
- The blades have a constant chord and cross-section.
- The blades are 60 % hollow/40 % solid.
- The airfoil geometry follows the cl5605 airfoil of Ingenuity [18]. This thin airfoil supports laminar flow even at low Reynolds numbers.
- The lift curve is linear at a slope of 6 (1/rad).
- The pitch angle of the blade changes linearly with radial position from 25° at the root to 8° at the tip.
- The chord-to-radius ratio is 1/20.
- Carbon Fiber-Reinforced Polymer (CFRP) with an allowable tensile stress of 600 MPa is used for rotors and spars.
- Spars are thin-walled cylinders with a thickness of 2 mm.
- The design air density is 0.01 kg/m^3 , corresponding to the lowest expected temperature at zero elevation. At cruise altitude, the forward speed will help with lift generation.

Rotor sizing

The thrust of each rotor is then found using the equation from Kaya and Kutay [19]:

$$T = t_1 \Omega^2 + t_2 (V \cos \alpha)^2 + t_3 \Omega (\nu_i + V \sin \alpha)$$

where Ω is the rotation speed, V is the multicopter's velocity, α is the multicopter's angle of attack and ν_i is the vertical induced velocity due to rotor downwash. Expressions for t_1 , t_2 , t_3 and ν_i depending on the geometry are given in [19]. The equation is based on an analytical evaluation of the blade element method.

After initial experiments, the thrust was too low to sustain the multicopter's design weight despite the large blade radius. Therefore, we considered coaxial rotors, which can greatly increase lift without increasing the rotor footprint. Compared to two individual rotors, the lift of two coaxial rotors is about 88% of that. This empirical factor is estimated from results of Coleman [20].

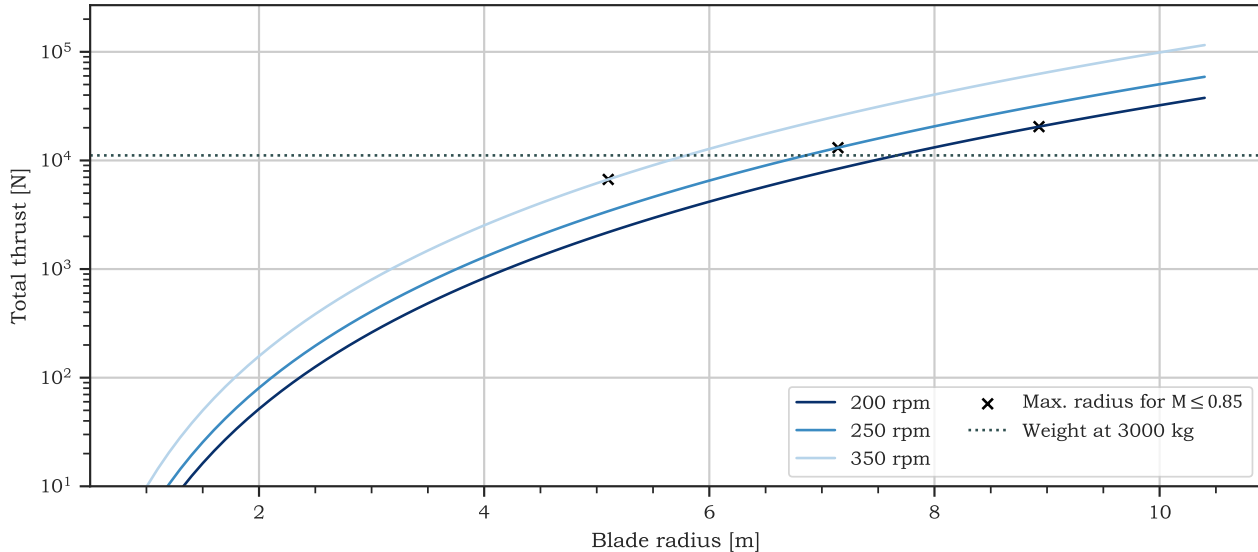


Figure 4.12: Radius–rotation speed combinations for six blades and four coaxial rotors.

An example of the resulting radius–rotation speed combinations is shown in Figure 4.12. Above a rotation speed of 250 rpm, the tip Mach number would be too high for any blade radius (i.e., the scatter point is below the dotted line). At 200 rpm, a radius of 7.8 m would be feasible. However, the minimum blade radius is 7 m, achieved at 250 rpm.

We calculated several combinations of 2–8 rotors with 3–6 blades. The resulting radii are 9.5 m to 5.5 m, the rotation speeds 200 rpm to 300 rpm. The next step is to find the option that results in the lowest total vehicle mass.

Engine and fuel sizing

In chapter Section 4.3.3, the torque required for each coaxial blade pair at different stages of the flight profile is derived. The critical condition with the highest required torque is the vertical ascent at the lowest density ($\rho = 0.01 \text{ kg/m}^3$), during which the torque of each rotor is $\tau_t = 3536 \text{ Nm}$, with the rotational speed $\omega_t = 250 \text{ rpm} = 26.2 \text{ rad/s}$. From this, the required horsepower can be derived as follows:

$$P[\text{hp}] = \frac{\tau \cdot \omega}{745.7} = 115 \text{ hp}$$

A 115 hp engine is necessary to rotate one set of coaxial rotors. Due to the need for in situ resource utilization, standard engines are not an option. Since the power requirement in cruise does not reduce significantly when compared to take-off, the battery mass required for the entire flight is too high to satisfy the mass requirement. Thus the Mg-CO₂ engine concept is used, as it is still under development. It is assumed that it will be twice as heavy as the exact horsepower Earth counterpart to account for the TRL. To estimate the mass of the earth's counterpart, a statistical analysis on Pratt and Whitney ⁴ series of engines. The engine masses are compared to the horsepower produced, and a relationship is found. The estimated lower bound for engine mass is 41 kg, and the upper bound for engine mass is 81 kg.

With the cruise speed of 111 m/s and the range of 1000 km as mentioned in the requirement, the cruise will take two and a half hours $t_c = 2.5 \text{ hrs}$. Adding thirty minutes for take-off and landing $t_t = 0.5 \text{ hrs}$. The

⁴URL: <https://www.prattwhitney.com/en/products/helicopter-engines> [cited 2023-05-11]

total energy used by all four engines during the flight can then be calculated to be:

$$E[kWh] = \tau_t \cdot \omega_t \cdot \frac{t_t}{1000} \cdot n_{engines} = 1110 kWh$$

Based on the same Pratt and Whitney series of engines, it was found that the average fuel consumption is $0.00195 \text{ g}/(\text{kWh} \cdot \text{hp})$ equaling 0.224 kg/kWh for a 115 hp engine. This value was obtained based on the current fossil fuels used. The Mg-CO₂ reaction releases 0.568044 times the energy when compared to fossil fuel reaction in the standard multicopter engines. Meaning that $\frac{1}{0.568} = 1.76$ times more fuel is needed making the fuel consumption of the Mg-CO₂ engine $0.224 \cdot 1.76 = 0.394 \text{ kg/kWh}$. This means that the total fuel consumption for a three-hour, 1000 km flight is:

$$M_{fuel} = 0.394 \cdot 1110 = 437 \text{ kg}$$

Mass estimation

The mass estimation approach is based on a mix of custom physical calculations and empirical relations for helicopters from Prouty [14]. While Prouty [14] has relations for all subsystems, a helicopter's layout is too different from our Martian multicopter to, for example, use their rotor and engine sizing. The system mass is broken down as follows:

$$MTOM = m_{rotors} + m_{engines} + m_{hubs} + m_{spars} + m_{fuselage} + m_{legs} + m_{misc.} + m_{payload} + m_{fuel}$$

Some component masses are taken to be fixed: $m_{misc.} = 400 \text{ kg}$ (estimated from remaining components like the fuel system, fuselage interior, electronics, etc.) and $m_{payload} = 350 \text{ kg}$ (set as a requirement).

The rotor mass m_{rotors} is calculated from the mass of each blade multiplied by the number of total blades. The blade mass depends on the volume and density. The cl5605 airfoil we use has $t/c = 0.05$ and is approximately triangular in shape. Therefore, the area is $0.025c^2$, from which the volume is found by multiplication with the blade length by the constant-cross section assumption. However, we assume that the volume is only filled to 40%, accounting for interior honeycomb structures and foam commonly found in multicopter blades [21]. The mass is then calculated with the density of CFRP. The blades account for roughly 25 % of the mass and may be a promising target for weight optimization. Note that we assume that the blade can sustain in-plane and out-of-plane bending stresses as well as centrifugal loads.

The engine mass $m_{engines}$ is just the individual engine mass multiplied by the number of sets of coaxial rotors. Both rotors are driven by the same engine.

The hub mass m_{hubs} is calculated using Prouty [14]'s relation for a multicopter hub and hinge, which have to support the centrifugal forces of the blades and contain the swashplate assembly. Our design does not require collective/cyclic control, which is usually responsible for much of a hub's mass, and benefits from more than 30 years of innovation since the publication of the book. Therefore, we use 20% of the estimated value and multiply it by the number of engines.

The spar mass m_{spars} is based on a thin-walled cylinder of length 1.2 times the radius for rotor clearance and a thickness of 2 mm. The diameter is set such that bending due to thrust is sustained. The spar is modeled as a cantilever beam made from CFRP with the thrust applied at the tip.

The fuselage mass $m_{fuselage}$ is based on Prouty [14]'s relation since we assume the multicopter fuselage to be similar to a helicopter fuselage. The fuselage size is independent of the rotor size, and the wetted area is based on a box of $5 \times 3 \times 2 \text{ m}$. The estimated mass is 83 kg for the structure only without interior items, which are part of the miscellaneous mass.

The landing leg mass m_{legs} is, again, based on Prouty [14]'s relation for four legs. However, we take 33 % of the value since we do not have wheeled legs. The estimated mass is 41 kg.

The fuel mass m_{fuel} is then set such that the total mass is 2700 kg through iteration, which leads to a fuel mass of 603 kg.

A multicopter with four coaxial rotors (i.e., eight rotors in total) of six blades leads to the largest fuel mass and will be used going forward.

4.3.2. Preliminary design

By Dominik Stiller

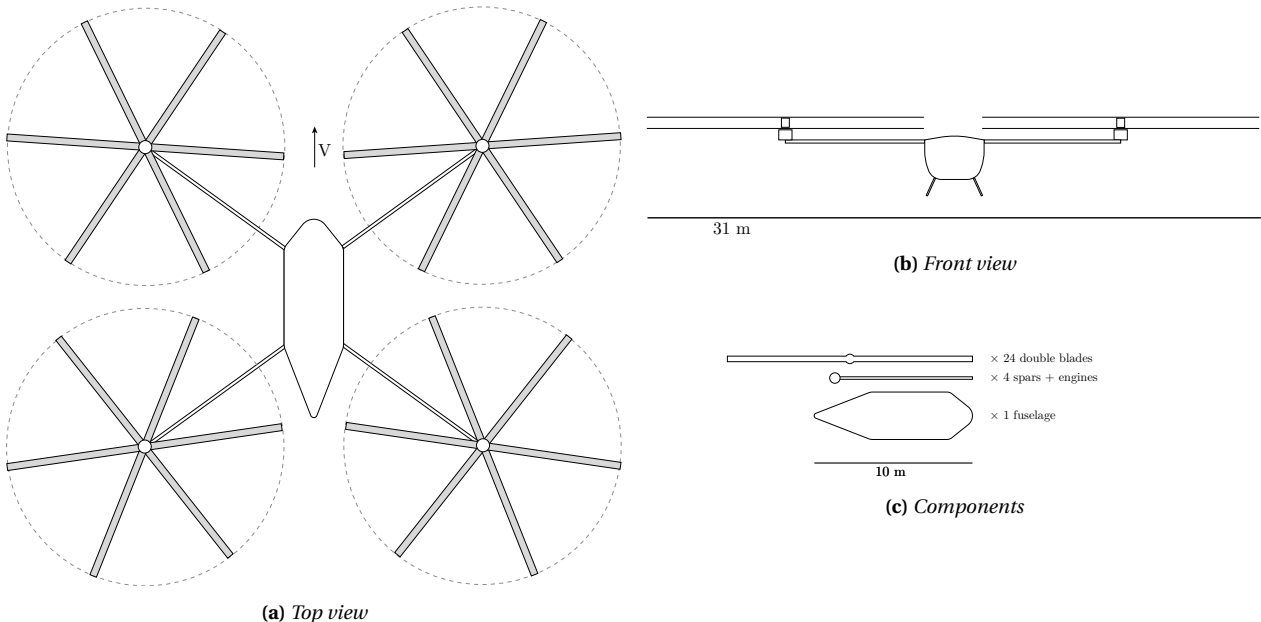


Figure 4.13: Scale drawings of the preliminary multicopter design with four coaxial rotors and a radius of 7 m.

The preliminary design of the multicopter is shown in Figure 4.13. The aircraft uses four coaxial rotors, so eight rotors of six blades each. The maximum rotation speed is 250 rpm during take-off. The blade radius is 7 m, with a chord of 0.35 m and a maximum thickness of 18 mm. The spars are 8.4 m long and have a diameter of 16 cm. The fuselage has a length of 10 m and a width of 3 m, although these dimensions should be considered a placeholder. The total dimensions of the multicopter are about 30 m in width and length, depending on the spar angle, and 4 m in height. The spars could be angled upwards for more rotor ground clearance.

The total mass is 2665 kg. Considering the rotor has been sized to sustain a weight of 3000 kg, there is sufficient margin. The blades have the largest contribution at 720 kg (there are 48 blades), followed by engines and hubs, which sum to 442 kg. The spars are relatively light at 58 kg.

The multicopter can be disassembled for transport as shown in Figure 4.13c. Rotor blades are assumed to be transported as double blades (i.e., three per rotor) of 14.5 m in length but could also be packed as single blades. They would then be stacked in a rack. The total disassembled volume is 186 m³, compared to an assembled bounding box volume of 3600 m³. The maximum height and volume are well within the capabilities of the SLS and Starship launchers.

4.3.3. Aerodynamic characteristic

By Patrick Kostelac

The aerodynamic characteristics of the aircraft are a crucial part of the design stage. As previously mentioned the gravity field on Mars generates an attraction of 3.71 m/s², meaning that 11130 N of lift is necessary. However, the Martian atmosphere can be as thin as $\rho = 0.01 \text{ kg/m}^3$, which requires large lifting surfaces. The multicopter design uses the rotor thrust as the main lifting component. The rotors are sized according to the critical conditions: vertical climb during take-off. The thrust equation from Kaya and Kutay [19] in Section 4.3.1 can be expanded to include the rotor geometry components:

$$\begin{aligned} T = & \Omega^2 \left(\frac{1}{6} \rho A \sigma a \theta_0 R^2 + \frac{1}{8} \sigma a \rho A \theta_{tw} R^2 \right) + (V \cos \alpha)^2 \left(\frac{1}{4} \rho A \sigma a \theta_0 + \frac{1}{8} \sigma a \rho A \theta_{tw} \right) \\ & + \Omega (V \sin \alpha + v_i) \left(-\frac{1}{4} \sigma a \rho A R \right) \end{aligned}$$

where ρ is the density, A is the area covered by the rotor, σ is the rotor solidity, $a \cdot \theta_0$ and $a \cdot \theta_{tw}$ represent the lift coefficient of the blade at the root and the tip with a being the lift curve slope and θ the twist angle and R is the radius of the rotor. The equation is based on an analytical evaluation of the blade element method. Using the analytical expression, the influence of individual blade parameters can be assessed, and thus an optimal blade radius, solidity, and airfoil, which minimize the mass and maximize the thrust, can be found. The thrust is generated due to the rotor's rotational velocity and the rotor blades' lift coefficient. Due to the difference in velocity at the blade root and the blade tip, the twist angle is introduced to distribute the lift along the blade radius evenly. The thrust produced by the blade depends both on the blade radius and the blade rotational velocity, as can be seen in Figure 4.12 but also on the lift coefficient along the blade, which is controlled by changing the before mentioned parameters.

The radius of 7 m and a rotational speed of 250 rpm found in Section 4.3.1 were obtained by using Ingenuity's clf5605 airfoil [18]. The airfoil twist was set to 25° at the blade root and 8° at the blade tip. The reason for such large twist angles is the induced velocity due to the rotor, which makes the angle of attack of the blades lower than the twist angle. The solidity of the blades is 0.095. Lastly, the current rotor configuration uses four coaxial rotors with three blades per rotor. With these parameters, the thrust produced at hover is 11800 N which is more than the multicopter weight allowing for take-off.

Just as the lift coefficient is a non-dimensional characteristic of fixed-wing aircraft, the ratio of thrust coefficient to solidity C_T/σ is the corresponding non-dimensional characteristic of multicopter. The average section lift coefficient \bar{c}_l is six times this [14]. While our value of $C_T/\sigma = 0.31$ during hover is quite high compared to existing vehicles (Ingenuity has 0.1), Prouty [14] suggests a maximum of 0.2 prevent blade stall), our blades have $\bar{c}_l = 1.86$, which is within a reasonable range for our clf5605 airfoil [18].

The drag coefficient of the multicopter can be divided into rotor torque drag and cruise body drag. The rotor blade rotational velocity generates large amounts of torque, which has to be compensated by the engines. The torque can be calculated using an analytical equation from Kaya and Kutay [19]:

$$Q = \Omega^2 \left(\frac{1}{8} \rho A \sigma \overline{C_d} R^3 \right) + (V \cos \alpha)^2 \left(\frac{1}{8} \rho A \sigma R \overline{C_d} \right) + (\Omega v_i) \left(\frac{1}{4} \sigma a \rho A \theta_0 R^2 + \frac{1}{8} \rho A \sigma a \theta_{tw} R^2 \right) \\ + (\Omega V \sin \alpha) \left(\frac{1}{4} \sigma a \rho A \theta_0 R^2 + \frac{1}{8} \rho A \sigma a \theta_{tw} R^2 \right) + (v_i + V \sin \alpha)^2 \left(-\frac{1}{4} \sigma a \rho A R \right)$$

Where the symbols are the same as in the thrust equation, and the $\overline{C_d}$ is the average drag coefficient. The rotor blades act as wings and generate both lift and drag. The drag thus has a zero lift drag component and the lift-induced drag component. Both have to be accounted for in the average drag component. Using the blade properties mentioned before and the average drag coefficient of 0.083 found from data in Koning et al. [18], the blade torque was calculated to be 3536 Nm. During cruise, due to the reduced RPM, the torque produced is only 1925 Nm

The cruise body drag also needs to be calculated. During the cruise, the main body, rotor connectors, and the rotors themselves cause drag opposite of the multicopter velocity. For drag purposes, the main body was assumed to resemble the AKTAY helicopter body with the values obtained from Batrakov et al. [22]; the cruise drag coefficient is 0.1. The connector spars are assumed to have an aerodynamic shape and a drag coefficient of 0.04. Additionally, the spars can be used to generate extra lift during cruise if necessary, but in that case, extra lift drag will be created. The blades of the rotors themselves also cause not only the torque but also the drag in the opposite direction of the velocity. The drag coefficient of the blades is 0.083, as assumed before. The cruise speed of the multicopter is 111 m/s, and assuming the worst ground-level conditions for drag. The density is then 0.02 kg/m³. The total drag during cruise is 730 N.

As a concluding remark to the aerodynamic chapter, it is worth mentioning that all of the aerodynamic forces were calculated for the worst possible conditions. That means that the lift was calculated for the lowest possible Martian atmosphere density, and the drag was calculated for the highest Martian atmosphere density. It is important to note that these two can never happen at the same time but are given here as the two worst-case scenarios that are considered.

4.3.4. Stability and control

By Patrick Kostelac

The multicopter design should be both stable and controllable. The multicopter design is stable if the multicopter can resist environmental disturbances. The multicopter design is controllable if the multicopter can move in any direction once in the air. In order for the multicopter design to be controllable, it does not require any control surfaces, as all of the maneuvers can be performed by throttling the thrust of the rotors. There are four pairs of coaxial rotors; each pair can be tilted, slightly vectoring the thrust of that coaxial pair. The list of maneuvers that can be performed by the multicopter can be seen below:

- **Vertical movement:** The multicopter can move horizontally by throttling all of the rotors. By increasing the angular speed of all the rotors, the thrust is increased, and the multicopter moves upwards. Similarly, the angular speed can be reduced, reducing the thrust, and thus the multicopter moves downwards.
- **Pitch:** The pitch of the multicopter can be controlled by increasing the angular speed of only the forward rotors or only the backward rotors. By producing a larger force in front or behind the center of gravity, the moment equilibrium is disturbed, and the multicopter pitches forward or backward.
- **Roll:** The roll is controlled similarly to the pitch, but instead of throttling the rotors in front or aft of the cg, the pairs of rotors on the left or on the right are throttled, creating a rolling motion.
- **Yaw:** In order to control the yaw, the multicopter rotors need to be able to tilt the rotors. Regular multicopters yaw by increasing the rotational speed of the diagonal rotors as the rotor's two sets of diagonal rotors rotate in different directions. However, in the case of coaxial rotors, throttling, specifically the counterclockwise or clockwise rotating rotors, is impossible, so the rotors' tilting is required. By tilting the rotors, the thrust is vectored, which can be used to induce a yawing moment when necessary. To ensure that the force remains in equilibrium and only the moments change, the diagonal rotors will be tilted simultaneously.
- **Horizontal movement:** The multicopter can move horizontally by either tilting the rotors while the main body remains in the same orientation or by pitching and rolling the body itself without tilting the rotors individually. Both of these actions create a horizontal thrust component, enabling the multicopter to move horizontally.

The multicopter is statically stable as it generates its lift from the rotors. The multicopter is symmetrical around its longitudinal axis, meaning it will have statically lateral stability. The longitudinal stability is achieved since the forward and aft rotors are at the same longitudinal distance to the center of gravity. In case of a pitch-up disturbance, the front rotors will move upwards, reducing their effective angle of attack and reducing the lift that the front rotors produce, simultaneously the aft rotors are moving down, and thus their effective angle of attack is higher, increasing the lift produced by the aft rotors. This will generate a restoring moment. The same can be concluded for roll stability. In case the downwards-moving rotors are close to stalling in cruise, they might stall when moving downwards, which is why a limitation on the twist angle of the rotors needs to be introduced. Due to the even mass distribution and a symmetrical geometry, a side slip will only result in a side force rather than a force and a moment; that force will need to be counteracted by using rotor tilt.

The dynamic stability of the multicopter design can be logically analyzed as a detailed stability analysis is out of the scope of this phase of the project. The multicopter design can be compared to a quadcopter drone when it comes to its stability characteristics. This means that the multicopter design will not have long term dynamic stability. However, the design will use an in flight computer that shall compensate any external forces or moments by throttling and vectoring individual rotors. Thereby even though the design may not be stable, it is not a major concern as it can be controlled by a in flight computer as demonstrated by quadcopter drones.

4.3.5. Performance analysis

By Patrick Kostelac, Dominik Stiller

The performance of the multicopter design will be analyzed based on the selected flight profile for the

mission. Each aspect of the flight profile will be assessed individually based on the multicopter design capabilities. The selected flight profile can be seen below:

- **Take-off:** The multicopter design concept has the capability to take-off and land vertically, which sets it apart from the standard airplane designs. This capability could be crucial for Mars exploration as it allows the multicopter to take-off and land almost anywhere. The take-off is the most demanding part of the flight profile for the multicopter design. As can be seen in Section 4.3.1, the highest required torque is during the take-off. During take-off the multicopter does not take advantage of horizontal velocity, which generates extra lift, and it requires additional power compared to hover as the multicopter needs to gain height.
- **Climb:** In case of a completely vertical climb, the required torque and power are the same as in the take-off. However, the climb does not have to be vertical. In order to optimize the climb, the multicopter will fly forwards as it climbs. The free stream velocity will help both the rotors and the connectors generate extra lift, which reduces the torque requirement on the rotors. The multicopter has been designed for a climb angle of 10°, but it is capable of a completely vertical climb if necessary. However, the vertical climb does require more power.
- **Maneuvers:** In case of a sand storm or terrain, the multicopter might need to deviate from the pre-determined flight path. The multicopter does not have any control surfaces; rather, it maneuvers by throttling the thrust on its rotors. Throttling the rotors at the front or at the back allows for yaw control, throttling the rotors at the left and right side allows for roll control, and throttling the diagonal rotors allows for yaw control. The multicopter thus has high maneuverability and is able to fly in crosswind conditions.
- **Cruise:** Due to the extremely high torque requirement on take-off, the multicopter is able to cruise at high velocities. As can be seen in Section 4.3.3, when designing for take-off, the available thrust for the cruise is 21 700 N. This allows for cruise speeds of up to Mach 0.7, set as the maximum in the requirements. However, in this case, the limiting factor is not the drag of the multicopter but rather the high Mach number experienced on the rotor blade tips due to the cruise speed and the rotational speed of the blades. Due to the high Mach number, the lift produced by the rotors is reduced, and thus the available thrust is reduced. Because of this, the multicopter will not cruise faster than 111 m/s. In order to fly at the desired speed, the rotors will be throttled down to an angular velocity of 148 rpm. Flying at this rpm and an angle of attack of 5° (nose down), the thrust is sufficient to sustain the weight and overcome drag. This will reduce the torque and the fuel usage of the engine. Since the limiting factor is the tip mach speed, In order to fly as fast as possible, the rotor should spin as slowly as possible, which is achievable at the highest densities. The design cruise altitude is thus as low as possible since that allows for the highest densities. However, the multicopter design is capable of flying at 5 km, but due to the lower densities at higher altitudes, the rotors will need to spin faster, which reduces the maximum cruise speeds at higher altitudes.
- **Descent:** The descent stage can be performed vertically or with the horizontal component. In case there is a horizontal component, again, extra lift can be generated due to it. During the descent stage, the multicopter will also need to slow down. This will be done by pitching backward and using the rotor thrust to generate a braking force. In the case of vertical descent, the descent speed is limited by the vortex ring state, which happens if the multicopter descends too quickly and its rotor blades get caught in the irregular air calculation.
- **Landing:** Similarly to take-off, the landing needs to be performed vertically. However, during landing, instead of requiring extra power to gain altitude, less power is required as the multicopter is losing altitude. This makes landing less critical than take-off, which justifies the decision to design for take-off rather than for the landing.

The payload–range diagram for the multicopter is shown in Figure 4.14. There maximum payload is only limited by the MTOM, not by structural considerations. Hence, the relation is linear over the whole range. At the range requirement of 1000 km, the maximum payload mass is 465 kg. At the payload requirement of 350 kg, the maximum range is 1270 km. Note that a safety factor of 1.3 is used for the specific fuel

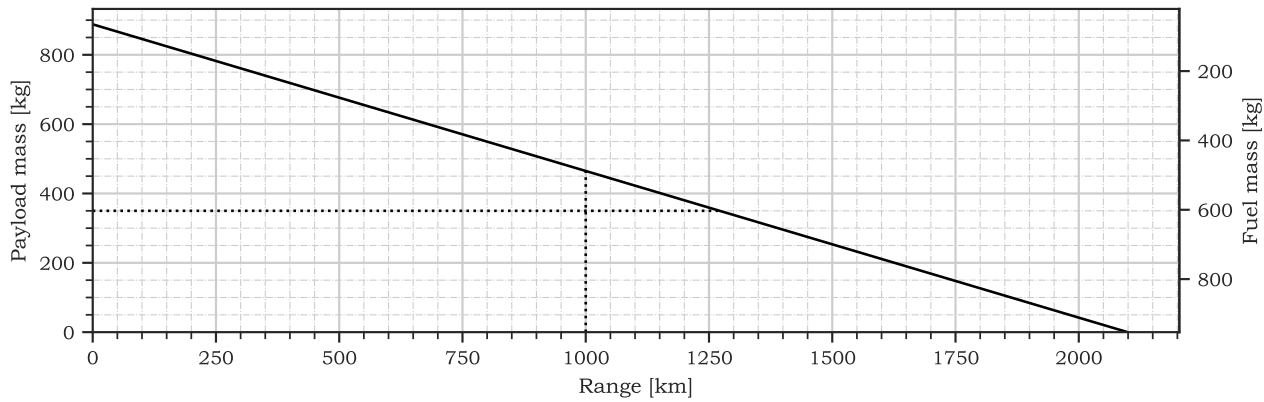


Figure 4.14: Payload–range diagram for the multicopter. Payload mass includes both astronauts and cargo. Take-off and landing requires 98 kg offuel without adding range.

consumption to account for engine uncertainty.

4.3.6. Desing concerns

By Patrick Kostelac

Lastly the design does come with some concerns. The proposed Mg-CO₂ engine is still in the development phase and is not yet flight proven, meaning that the engine might not be viable and in case it is viable, its mass and fuel consumption might be higher than anticipated. Additionally, multicopters at the large scale have not yet been used, this comes with a new set of concerns. The large blades could prove to be a weakness in the design as they introduce large forces and moments into the rotor hub structure. The hub structure has not been explored in detail, which can influence the blade flutter and bring the blade structural integrity in question due to fatigue. The stability and controllability of the design could also be a potential hurdle. Currently only drones use throttling of the rotors as a control measure while larger helicopter use swash plates. The proposed design uses a combination of both which adds extra weight. The yaw control is achieved only by tilting the rotors which might not be the most efficient, a potential small tail which adds yawing possibilities could be explored.

4.4. Design concept 5: Airship

By Freek Braspenning, Thomas van de Pavoordt

The final design option considered was a lighter-than-air vehicle, i.e. an airship. The airship produces lift passively by means of buoyancy, removing the need for a runway, or rotary lifting surfaces. In this section, the process of sizing the airship is shown.

4.4.1. Definition

An airship as a planetary exploration vehicle has been considered in various different mission concepts as a way to cover ground quickly and with a higher efficiency than an ordinary rover [23, 24]. Due to the aircraft being lighter than air, it creates a buoyant force that can provide enough lift to carry the weight of the aircraft. This passive way of providing lift gives the airship a high efficiency. The benefits and challenges which come with the preliminary sizing are given below.

Firstly, the use of hydrogen is highly beneficial on Mars. There is no risk of combustion since hydrogen does not react with carbon dioxide, which is prominently present in the Martian atmosphere. Furthermore, since hydrogen is the lightest known gas, it will create the most buoyant force compared to any other gas. In addition to this, hydrogen is widely available on Mars. There is a surplus of water under the surface of Mars, which can be used to produce breathable oxygen by electrolysis with hydrogen as a by-product. In addition to this, since hydrogen can be obtained through the electrolysis of water, which can be obtained by mining ice on Mars, this fuel is sustainably available. This process will also produce oxygen as a by-product that can be used as breathable air for the astronauts or any habitat present on Mars.

Next to this, the passive lift generation of the airship offers Vertical Take-Off and Landing (VTOL) capabilities. This allows for the exploration of remote places, even those that cannot be accessed by conventional airplanes. Furthermore, the low density benefits drag performance. The low density reduces the drag which in turn will reduce the thrust required and the weight needed for propulsion.

The airship is a challenging design to size for a couple of reasons. First of all, the low density of the Martian atmosphere posed an issue in providing enough buoyant force. While the relative ratio of the density of the atmosphere and the lighter-than-air gas is greater on Mars than on Earth, the absolute difference was too little to provide a useful buoyant force. This resulted in a massive volume which caused the weight of the encapsulating skin to increase quadratically. As the skin density can not be meaningfully lowered, without compromising strength, it ended up weighing too much. Furthermore, while the density is much lower than on Earth, the requirement for cruise speed proved to be unattainable, since the airship will need to withstand the higher pressure that occurs at cruise speed.

In addition, hydrogen is the smallest element and is therefore highly prone to permeation. This will cause very precise tolerances on the skin to prevent permeation, which will likely cause an increase in weight. Due to permeation, the hydrogen will also be refueled often, which puts constraints on the time available to fly and on the production of hydrogen.

It can thus be said that it is worth investigating the concept of an airship on Mars. The Martian atmosphere could provide an environment in which an airship can excel, due to the decreased gravitational acceleration and drag. However, this same environment poses significant challenges due to an increase in required volume and thus mass.

4.4.2. Preliminary Sizing

For the preliminary sizing of the airship, several estimation formulas are set up. These formulas provide a first estimate of the mass and performance.

There are several design options when considering an airship, such as the gas used in the blimp, the propulsion type, and the skin materials. Hydrogen was chosen as lighter-than-air gas, as it is more sustainable and lighter than helium. The density of hydrogen was obtained by means of the ideal gas law, as seen in Equation (4.27):

$$\rho_{H_2} = \frac{p_{H_2}}{R_{H_2} T_0} \quad (4.27)$$

where $p_{H_2} = 1.005 \cdot p_0$, and $R_{H_2} = \frac{R}{M_{H_2}}$.

The volume of the gas chamber of the airship is obtained from Equation (4.28).

$$V = \frac{m_{MTOM}}{\Delta\rho} \quad (4.28)$$

where

$$\Delta\rho = \rho_0 - \rho_{H_2} \quad (4.29)$$

This equation is based on the force equilibrium between the weight of the airship and the buoyant force provided by the difference in density between hydrogen and the Martian atmosphere. Buoyant force is defined as:

$$F_{Buoyant} = \rho_0 V g_M \quad (4.30)$$

The shape of the gas chamber is then assumed to be a sphere in order to get a high-level estimation of the surface area needed to encapsulate the gas chamber, as per Equation (4.31) and Equation (4.32).

$$V = \frac{4}{3}\pi r^3 \quad (4.31)$$

$$S = 4\pi r^2 \quad (4.32)$$

The mass of the skin is then estimated using Equation (4.33), where $\rho_{skin} = \rho_{HDPE} = 940 \text{ kg m}^{-3}$, t the thickness of the skin, and S the previously calculated surface area. Several skin materials have been considered for high strength and low weight, of which High-Density Polyethylene was assumed.

$$m_{skin} = \rho_{skin} S t \quad (4.33)$$

With the mass of the skin, the total volume required can be calculated again and this process is iterated until it converges. The iteration is then optimized to carry the least amount of skin mass, to be able to leave as much mass for the payload, fuselage, propulsion system, and other subsystems.

4.4.3. Aerodynamic characteristics

Once the preliminary size had been determined, a drag estimation was performed to be able to calculate the required thrust, fuel and range, for example. The drag of an airship can be quantified by Equation (4.34), as given by Li et al. [25].

$$C_D = C_F \left[4 \left(\frac{L_a}{D_m} \right)^{1/3} + 6 \left(\frac{L_a}{D_m} \right)^{-1.2} + 24 \left(\frac{L_a}{D_m} \right)^{-2.7} \right] \quad (4.34)$$

Here, L_a/D_m is the fineness ratio of an airship, which sets up a more ellipsoid shape that induces less drag than a sphere. The skin friction drag coefficient, C_F , is approximated by Equation (4.35):

$$C_F = 0.045 Re^{-1/6} \quad (4.35)$$

The Reynolds number can be calculated for the characteristic length of the airship, using Equation (4.36) and the dynamic viscosity given by Equation (4.37) [26].

$$Re = \frac{\rho V L_a}{\mu} \quad (4.36)$$

$$\mu = \mu_0 \left(\frac{T}{T_0} \right)^{3/2} \left(\frac{T_0 + S}{T + S} \right) \quad (4.37)$$

where the dynamic viscosity at T_0 is given by $\mu_0 = 1.37 \times 10^{-5} \text{ Nsm}^{-2}$, with $T_0 = 273 \text{ K}$, and Sutherland's constant is given by $S = 222 \text{ K}$ [26].

Drag is then easily computed with Equation (4.38):

$$D = 0.5 \rho V_{cruise}^2 S C_D \quad (4.38)$$

With the drag known, the thrust required is also known and from this, the required fuel can be calculated. The engine weight was estimated using the method described in Chapter 3, with the engine thrust specific fuel consumption used in Equation (4.39) to calculate the required fuel mass:

$$m_{fuel} = SFC \cdot D \cdot \frac{R}{V_{cruise}} \quad (4.39)$$

This formula can also be used to calculate the achievable range with the amount of mass that is left for fuel without breaking the MTOM requirement.

4.4.4. Results

With the formulas complete, several results can be obtained before deciding whether to move on with further analysis into stability & control, and performance characteristics. The airship has been optimized to have a mass of 2700 kg in total, as prescribed by the mass budget with contingency. In this MTOM, 720 kg will be the effective payload mass, meaning that in this mass everything other than the mass of the skin encapsulating the hydrogen volume will be incorporated. Taking into account that 350 kg of payload mass will be allocated to the 2 astronauts being transported, only 370 kg is left for systems such as structures, propulsion, and fuel. The mass of the fuselage is estimated via the same estimation methods prescribed in Section 4.1.2. This leaves 110 kg for control surfaces, the propulsion system, fuel, and other miscellaneous mass.

When flying at 400 km/h, it was found that the drag of the airship was 2298 N, from which it followed that the propulsion system mass would be 231 kg. Naturally, this is too much mass already for the available amount and thus renders this configuration infeasible. It was therefore decided to find a combination of speed and, eventually, range that would render achievable. Naturally, the more the speed decreased, the more the drag decreased and the more the fuel mass could increase, due to a lighter propulsion system. However, to achieve the range of 1000 km, as determined by the requirements, the speed would have to decrease by 90%. A compromise was found at 50% of the range requirement, thus 500 km, and 25% of the speed, thus 100 km/h. This speed is significantly faster than current-day rovers and has far more range, thus still providing plenty of advantages. It does mean that certain requirements are not met and that will be reflected in the trade-off, which will be performed after the Verification & Validation (Chapter 5) in Chapter 7.

Verification and Validation of Design Concepts

This chapter presents the verification and validation of each design concept. The methods used to obtain design parameters needed to be verified and validated to perform a trade-off based on the design concepts. Each design was based on a set of parameters obtained through numerical calculations, which were carried out using software developed internally. To verify the programs, first unit testing was performed on individual formulas, after which a global verification procedure was done. To validate the programs, existing aircraft were used: the inputs to the program shall resemble an existing aircraft, and the program's outputs were compared to the parameters of those aircraft.

5.1. Fixed-Wing Aircraft: Flying Wing & Biplane

By Adrian Beño, Joachim Bron, Timo de Kemp

Verification refers to checking whether the equations solved during the design process were solved correctly. In order to perform verification, two different verification methodologies were used: code testing, composed of unit tests and global tests, and verifying whether the numerical solvers produce results compatible with analytical solutions of arbitrary, simple problems.

5.1.1. Code test

The numerical tools for the design of the fixed-wing aircraft consist of a combination of Microsoft Excel files. These were tested using unit tests, where the outputs to a particular combination of inputs are known. The input-output for cells with formulas was then compared to the expected output to detect mistakes in the tools and calculations. Once the Excel files were fully unit tested, the tools were used to design the two fixed-wing aircraft. A detailed description of the unit tests is omitted since these were directly implemented into the Excel files, and each calculation was in a bottom-up fashion, instead of testing in a separate phase.

5.1.2. Comparison with analytical solutions

Two comparisons of numerical simulation with analytical solutions are presented. Firstly, the $C_l - \alpha$ curve, as predicted analytically by inviscid thin airfoil theory, is compared to the $C_l - \alpha$ of the NACA0006 airfoil at $Re = 10^8$. At this relatively high Reynolds number, the flow can be assumed to be dominantly governed by inertial effects rather than viscous effects. Furthermore, the thickness of the airfoil can also be assumed to approach an infinitely thin airfoil. This comparison is shown in Figure 5.1, where an extremely close match, with maximum absolute error $|\epsilon_{abs}| = 0.029$ [-] and maximum relative error $|\epsilon_{rel}| = 0.026$, is visible and the thin airfoil theory prediction of $\frac{dC_l}{d\alpha} = 2\pi \text{ rad}^{-1}$ is met. Also, the airfoil is symmetric, which is reflected in the $C_l - \alpha$ having an intersection with the origin.

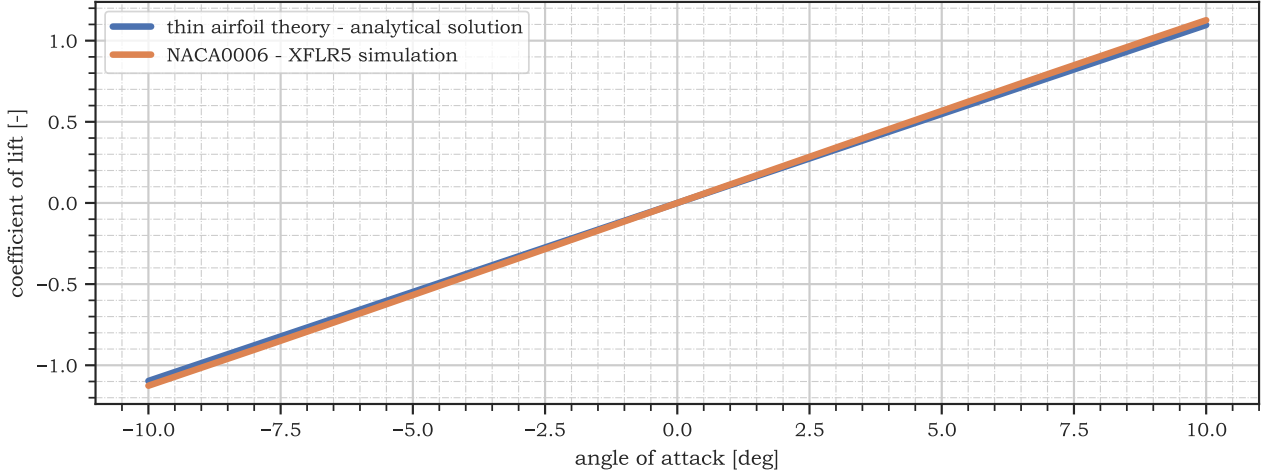


Figure 5.1: Comparison of $C_l - \alpha$ curves, as predicted by thin airfoil theory and as computed with XFLR5 for a NACA0006 airfoil at $Re = 10^8$.

Secondly, a cantilever beam's analytical and numerical stress distributions under a constantly distributed load are presented. The analytical solution is given by Equation (5.1):

$$\sigma_y = \frac{\left(\frac{b}{2} - y\right)^2 w z}{2I} \quad (5.1)$$

Where y [m] is the spanwise wing position, starting at the root, z [m] is the vertical position along the wing, w [N/m] is the load distribution, and I [m^4] is the area moment of inertia. For this verification simulation, a rectangular wingbox is assumed; hence the maximum and minimum vertical position distributions are provided. The comparison of our numerical solver with the analytical solution is provided in Figure 5.2a. A close match is visible, adding to the confidence in the model.

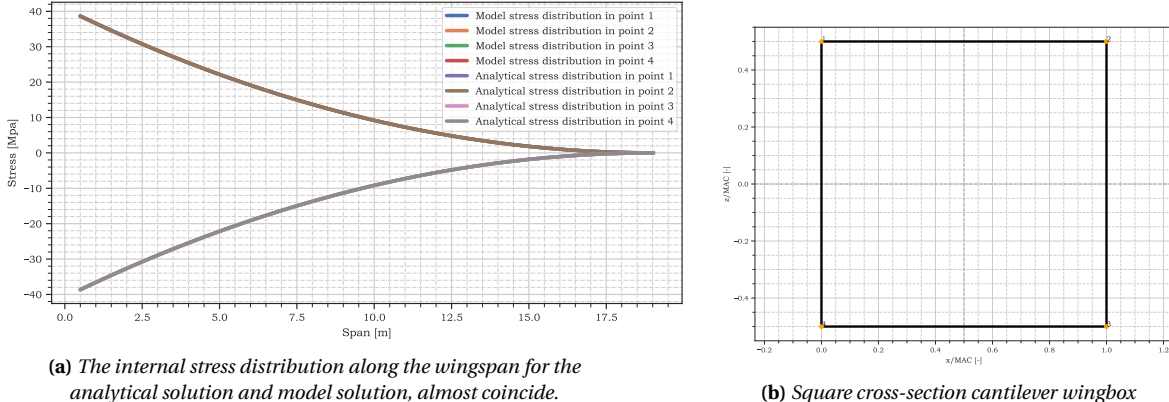


Figure 5.2: Comparison of numerical simulation prediction to the analytical solution.

Validation refers to checking whether the equations chosen to be solved during the design process represent the governing physical phenomena of the real world. In order to perform validation, two different validation methodologies were used, as listed below.

- Most papers published on low Reynold's number high lift airfoils are conducted in wind tunnels on small models. The scalability of these results to our design must be validated.
- Most weight estimation calculations use weight estimation formulas from [5]. These formulas are based on statistical relationships of Earth-based aircraft. Hence, validation must be performed for their validity in the Mars atmosphere.

5.1.3. Simulation scalability

A comparison between low Reynold's number lift curve characteristics of high lift low Reynold's number airfoil S1223, as predicted by XFLR5 simulation and experimentally measured by Ma et al. [27] is presented. This is given in Figure 5.3. The overall shape of the curve follows our expectations and the only source of lowered confidence in the model stems from the curve being slightly shifted to the left, by around 4°. This results in the maximum relative error in any C_l prediction of 11 %. Because verifying the non-viscous case yielded a perfect match, we conclude that this 11 % error stems exclusively from the viscous effects, which XFLR5 superimposes on the otherwise linear non-viscous model. Hence, future design calculations shall be carried out with an 11 % uncertainty margin in the theoretically predicted lift coefficient. The scalability and extrapolability of simulation results are valid if all non-dimensional flow numbers, such as Reynold's number, are kept constant across the extrapolation.

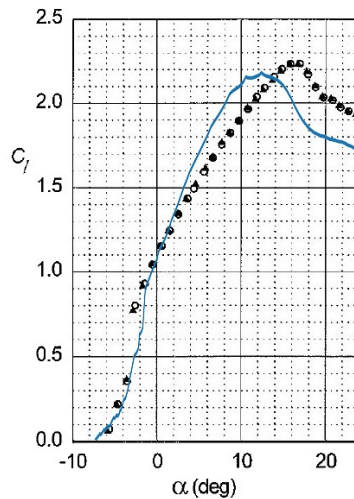


Figure 5.3: Comparison of lift curves of airfoil S1223. The blue line corresponds to XFLR5 numerical simulation. Black dots correspond to experimentally produced data by [27].

5.1.4. Weight estimation validation

Secondly, weight estimation formulas from Torenbeek [5] are based on statistical aircraft relationships of Earth-based aircraft. Unfortunately, a statistical analysis of how much these differ concerning Mars-based aircraft cannot be conducted, as there are no examples available for Mars. At the same time, some assumptions about their validity can be concluded. For example, the gravity on Mars is about three times as low as Earth's. Hence aircraft structures on Earth have to withstand about three times as high loads. Hence predictions by Torenbeek [5] are conservative and we expect that the detailed design phase will yield lower weights than those currently predicted.

5.2. Tiltrotor

By Sebastian Harris, Javier Alonso Garcia, Thomas van de Pavoordt

Verification of the tiltrotor is done in two parts: Section 5.2.1 starts with verifying individual functions in the code used to determine all parameters related to the tiltrotor. Section 5.2.2 tests the system as a whole through sensitivity analyses. After verification, Section 5.2.3 will explain the validation done for the tiltrotor analysis.

5.2.1. Unit test verification

By Javier Alonso Garcia, Thomas van de Pavoordt

Unit testing of the tiltrotor is focused on code verification of the different functions calculating performance. In order to locally verify the code, a series of unit tests were performed that combine checking the correlation between inputs and outputs (for example, increasing MTOM should lead to a greater wing surface area) and extreme value tests. Using Python's library `unittest`, it was tested whether a variation

in a specific input resulted in the corresponding correlation in output, i.e., the positive correlation should test TRUE when an increase in input results in an increase in output. The functions tested and the expected correlation between input and output are given in Table 5.1. All functions passed their unit tests and can, in that sense, be considered successfully verified.

Table 5.1: Functions undergoing unit testing and their expected correlation between input and output

Function	Input	Output	Correlation
RadiusMassElementMomentum	Mass	Thrust	Positive
	Mass	Radius	Positive
	Mass	Rotor Mass	Positive
	# of rotors	Thrust	Negative
	Density	Radius	Negative
	Gravity	Thrust	Positive
Area	C_l	Area	Negative
	Mass	Wing area	Positive
	Dynamic pressure	Wing area	Negative
	Gravity	Wing area	Positive
DragEstimation	Fuselage size	C_d_0	Positive
Size_power_subsystem	T_0 Thrust	Battery mass	Positive
	Cruise time	Battery mass	Positive
	Take-off time	Battery mass	Positive
Class2Weight	Rotor radius	Tail weight	Negative
	Fuselage size	Body weight	Positive
	Braced Wing	Wing weight	Negative
	Ultimate load	Tail weight	Positive
AircraftClimbPerf	Battery mass	ROC	Positive
	Power density	ROC	Positive
	Mass	ROC	Negative
RotorClimbPerf	Mass	ROC	Positive
	Rotor radius	ROC	Negative
	# of rotors	ROC	Positive

5.2.2. Sensitivity Analysis

By Javier Alonso Garcia

In order to test the system as a whole, two different sensitivity analyses were performed. The first was a typical sensitivity analysis using Python's *SALib* library, which tested the correlation between a set of inputs and outputs of the design function. The Sobol indices for this study can be seen in Table 5.2, which represent how much does the variance of an output depend on the variance of a particular input¹.

Table 5.2: Sensitivity analysis between function inputs and outputs

(a) Sensitivity of the design to prescribed inputs from the customer

Inputs / Outputs	Range	Total mass	Rotor mass	Battery mass	Body mass	Wing mass	Tail mass	Rotor radius	Wing-span	Chord	Cruise thrust	Max power
payload mass	0.06	0.12	0.00	0.04	0.03	0.05	0.03	0.00	0.00	0.02	0.05	0.00
design range	0.03	0.02	0.00	0.09	0.01	0.01	0.01	0.00	0.00	0.00	0.01	0.00
cruise speed	0.93	0.44	0.00	0.75	0.93	0.18	0.93	0.00	0.00	0.96	0.90	0.00
maximum mass	0.02	0.41	1.02	0.11	0.01	0.76	0.01	1.02	1.01	0.01	0.02	1.02

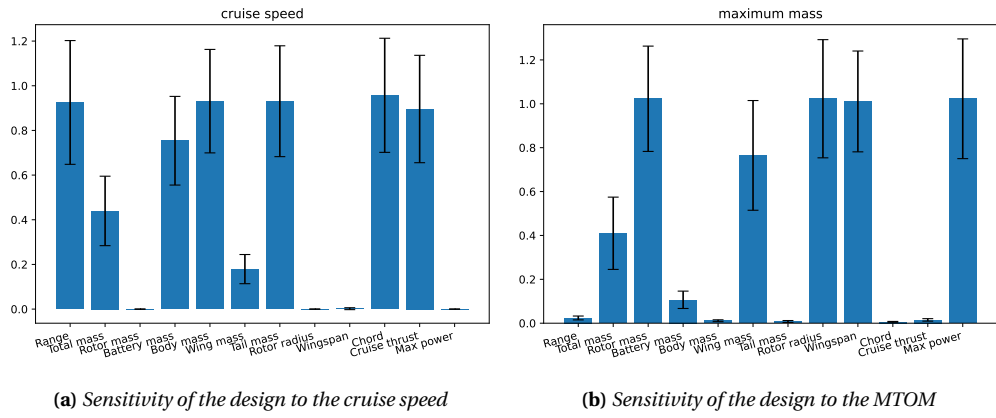
¹URL: <https://towardsdatascience.com/sobol-indices-to-measure-feature-importance-54cedc3281bc>
[cited 2023-06-02]

(b) Sensitivity of the design to calculated values

Inputs / Outputs	Range	Total mass	Rotor mass	Battery mass	Body mass	Wing mass	Tail mass	Rotor radius	Wing-span	Chord	Cruise thrust	Max power
Gravity	0.01	0.01	0.00	0.02	0.00	0.01	0.01	0.00	0.00	0.00	0.01	0.07
Air density	1.02	0.99	0.85	0.93	1.00	0.95	0.99	0.84	0.90	1.00	0.97	0.04
Speed of sound	0.00	0.01	0.16	0.07	0.01	0.04	0.01	0.16	0.10	0.01	0.03	0.97
Cruise viscosity	0.00	0.00	0.00	0.00	0.00	0.00	0.00	0.00	0.00	0.00	0.00	0.00

(c) Sensitivity of the design to assumed values

Inputs / Outputs	Range	Total mass	Rotor mass	Battery mass	Body mass	Wing mass	Tail mass	Rotor radius	Wing-span	Chord	Cruise thrust	Max power
C_l	0.13	0.43	0.42	0.19	0.76	0.31	0.61	1.01	1.01	0.76	0.51	1.05
Power density	0.25	0.04	0.00	0.82	0.02	0.00	0.01	0.00	0.00	0.02	0.02	0.00
Energy density	0.68	0.00	0.00	0.00	0.00	0.00	0.00	0.00	0.00	0.00	0.00	0.00
Blade density	0.00	0.20	0.23	0.00	0.09	0.02	0.07	0.00	0.00	0.09	0.11	0.00
Fill factor	0.01	0.31	0.35	0.00	0.14	0.04	0.11	0.00	0.00	0.14	0.18	0.00
Ultimate load	0.00	0.01	0.00	0.00	0.01	0.62	0.23	0.00	0.00	0.01	0.01	0.00
Take-off time	0.01	0.00	0.00	0.00	0.00	0.00	0.00	0.00	0.00	0.00	0.20	0.00

**Figure 5.4:** Sensitivity of the design to prescribed inputs from the customer with a 95% confidence interval

Firstly, the code was based on the values derived from the requirements such as the cruise speed and the maximum allowed mass. Therefore, the output of the code was expected to be sensitive to these values. As seen in Table 5.2a, these parameters even have a score greater than 1 in some places, implying that variations in this input will have effects on other inputs, leading to significant variability in the final output. These effects can be better visualized in Figure 5.4 and will be paid special attention to in the detailed design phase. The parameters which were expected to cause high variance (maximum mass and cruise speed) were confirmed to do so. The validity of the numerical value of these parameters will be of particular importance during the detailed design stage.

Similarly, calculations were also based on environmental values investigated in literature. The variance is small for all parameters other than air density as seen in Table 5.2b which impacts greatly the output of the design. For this reason, the best and worst case design scenarios used in Chapter 7 were based on the design air density.

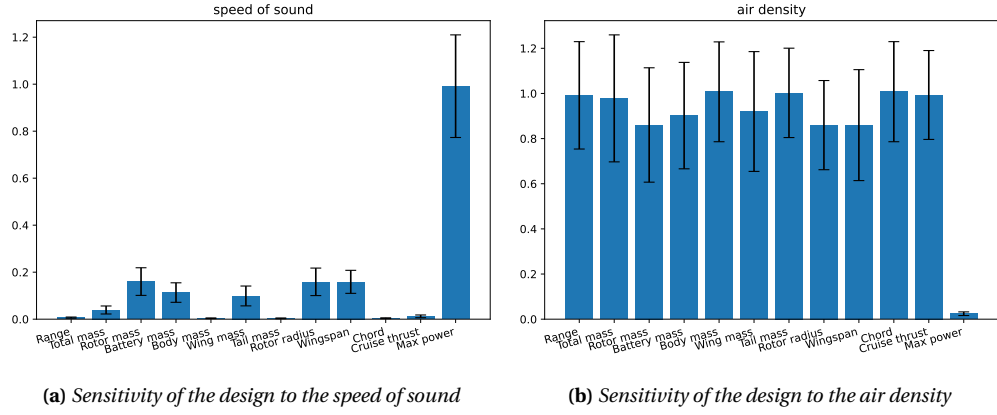


Figure 5.5: Sensitivity of the design to calculated inputs from the environment with a 95% confidence interval

Finally, the code was also based on the performance of individual components such as the batteries or the airfoil used. Since the same airfoil is used for the rotor blades and the wings, its lift coefficient was expected to have a large impact on the design; which was indeed the case, as seen in Table 5.2c and Figure 5.6a. Based on the outputs of this analysis, special attention will have to be payed to the lift coefficient, battery power density and battery energy density in the next design phase.

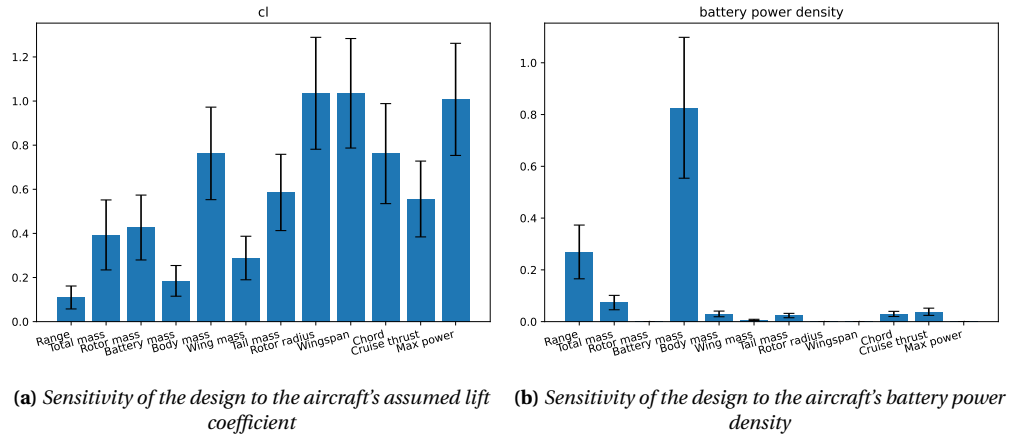


Figure 5.6: Sensitivity of the design to assumed performances with a 95% confidence interval

As a second system test, the influence of upstream functions' outputs on the simulation outputs was tested. This offered insight into determining which functions were more critical, which was helpful when deciding which margins were appropriate for the validation. This was done by adding 10% to the outputs of each function one at a time and comparing the result with the data obtained without perturbances. As can be seen in Table 5.3, variations of the output of the rotor sizing have significant impact throughout all of the outputs, except for the total mass. Due these high uncertainties in important parameters such as Rotor radius, validation of the outputs of the sizing of the rotor were be performed in Subsection 5.2.3.

Table 5.3: Change in output value due to a 10% change in a function's output

Output/Function	Rotor sizing	Wing sizing	Drag	Power sizing	Class2Weight
Range	7.63%	-7.86%	-0.11%	3.81%	12.44%
Total mass	-0.39%	8.52%	0.07%	8.84%	3.77%
Rotor mass	10.00%	0.00%	0.00%	0.00%	0.00%
Battery mass	-11.47%	19.64%	0.19%	23.06%	4.34%
Body mass	-3.15%	3.29%	0.02%	3.42%	11.42%
Wing mass	4.02%	13.51%	0.07%	10.75%	14.39%
Tail mass	-18.50%	36.27%	0.12%	18.91%	17.56%
Rotor radius	10.00%	0.00%	0.00%	0.00%	0.00%
Wingspan	3.42%	3.77%	0.03%	3.92%	1.49%
Chord	-3.66%	3.77%	0.03%	3.92%	1.49%
Cruise thrust	-17.71%	27.13%	0.26%	16.40%	5.99%
Max power	10.00%	0.00%	0.00%	0.00%	0.00%

5.2.3. Validation

By Sebastian Harris

The validation procedure for the design process of the tiltrotor is doubly complex, first in the aspect that tiltrotors are unique and few designs were developed into finished products. Next, using rotorcraft on Mars has only recently become a possibility, thus further reducing the available validation data. However, the process of sizing rotors should be comparable with rotorcraft on Earth in the same conditions. As such, the validation procedure was run by modifying the design environment to match Earth's. The two main outputs of the function are the rotor size and the rotor power. The following data was collected and used as an input:

Table 5.4: Available data from various tiltrotor aircraft [28]

Name	Rotor Radius [m]	Take-off Mass [kg]	Power[kW]	Rotors	Blades	Tip Mach
V-22	5.8	23859	5498	2	3	0.9
V-280	5.35	17200	4470	2	3	0.75
AW609	3.96	7620	1446	2	3	0.7

After importing this data into the function, the output is compared to the true values. The results are tabulated below:

Table 5.5: Differences between calculated and real data for various tiltrotors

	V-22		V-280		Aw609	
	Radius [m]	Power [kW]	Radius [m]	Power [kW]	Radius [m]	Power [kW]
Calculated	5.4	5428	5.5	3259	4	1401
Data	5.8	5498	5.35	4470	3.96	1446
Difference	6.9%	1.26%	-2.8%	27.1%	-1%	3.12%

The significant variation in power related to the V-280 is mainly due to the lack of information regarding the vehicle. As it is relatively recent and under development, the values found are most likely outdated and, as such, need to be validated. Other validation procedures are unavailable, as the lack of information on other tiltrotor aircraft leads to a lack of validation that can be performed on this preemptive study. However, more in-depth validation procedures will be possible for the following steps of the Design Synthesis Exercise by performing wind-tunnel validation, testing with scale models, and otherwise ensuring the design performance follows that of the models.

5.3. Multicopter

By Patrick Kostelac

The verification of the multicopter is done in two parts; first unit verification on formulas, and second function testing verification. The sensitivity analysis is done by varying the inputs. The validation is done by performing a local validation of assumptions and formulas and a global validation.

5.3.1. Unit testing verification

The first step is making sure that the inputs to the program have the correct values. The values should be presented in SI units. This was done by comparing the values used in the program to the values obtained in Haberle et al. [29]. The values on Martian atmospheric conditions such as the density, speed of sound, and the gravitational acceleration were found to match the literature, thus they were verified.

The second step of unit verification is the verification of the individual formulas used in the program. The code used for the parameter estimation can be divided into two parts, a part used for aerodynamic modeling and a part used for mass estimation. The aerodynamic modeling was verified by first confirming that the units of the formulas are equal on both sides. Then by comparing the formula to Kaya and Kutay [19]. After comparison, the output value of the program is compared to a hand-calculated value and the values obtained in the paper. The paper has validated the formulas with an experiment and they are thus considered correct and verified. The mass estimation is performed on a combination of statistical relations and geometric relations. The mass estimation is a combination of well-known geometric relations which are verified and the statistical relations from the book Prouty [14] and was thus considered validated. The verification procedures are the same as in the aerodynamic modeling.

5.3.2. Function testing verification

The first output to be verified is the plot showing the maximum allowable radius at each rpm. First the inputs are verified. Then the maximum tip Mach number is verified using data attained by NASA². The output of the graph was first verified by visual inspection. At the same blade radius, the higher RPM should produce more lift, similarly for the same RPM, a larger blade radius increases lift. Lastly, it is expected that the larger blades will produce more lift at the tip Mach number of 0.85. The plot has passed the visual inspection test. After the visual inspection tests, the maximum radius for each RPM in accordance with the Mach number constraints was independently calculated and compared to the graph values. The values matched and thus the graph was verified.

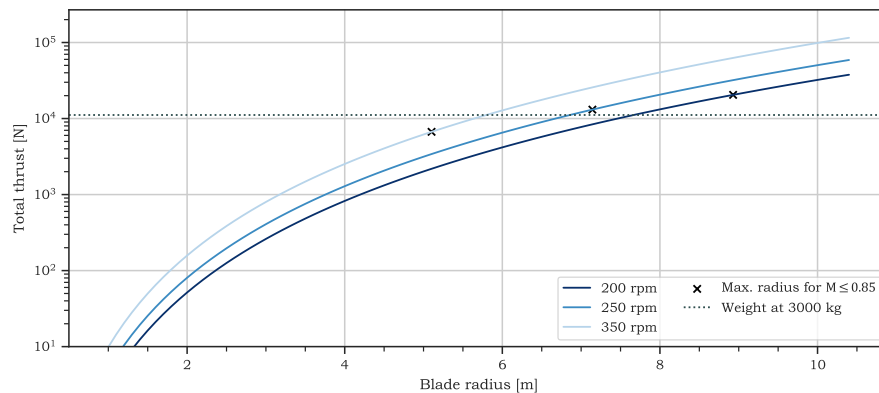


Figure 5.7: Radius–rotation speed combinations for six blades and four coaxial rotors.

The next step was verifying the lift, torque, and drag calculations. The lift and torque calculations use the formulas from Kaya and Kutay [19]. Most of the inputs are design parameters so the only verification measure was checking that the correct inputs are taken. However, one of the inputs is the induced velocity. The induced velocity uses thrust as input and thus a loop is created. In order to ensure that the correct values are used, numerical optimization was used until the change in thrust and induced velocity

²URL: <https://mars.nasa.gov/technology/helicopter/> [cited 2023-05-16]

was below 1 %. The `scipy` function is considered to be already verified. The drag function takes only the design parameters, cruise and take-off speed, and density as input. Thus only the use of correct values was verified.

5.3.3. Formulas assumptions

The next step of verification and validation is making sure that the formulas used in the program are valid for the low Reynolds number and low density environment and can be applied to the large Martian multicopter. In order to validate the formulas used in the program, the assumptions used in the formulas presented by Kaya and Kutay [19] need to be valid in the low Reynolds number environment. Only the airfoil aerodynamic characteristics are affected by the atmosphere and thus to confirm that the assumptions are valid on Mars, the airfoil data for low Reynolds number and low density is used.

Firstly it is assumed that the blades of the rotors are rigid with a constant chord. In the multicopter design, the blades do indeed have a constant chord making that part of the assumption valid. To validate the rigidity the blades were assumed to be cantilever beams mounted at the rotor hub. To account for the worst-case scenario the lift is assumed to act on the blade tip. With that assumption, the deflection of a seven meter blade is half a millimeter which is several orders of magnitude smaller, and thus this assumption is valid. Secondly, it was assumed that the lift coefficient of the airfoil varies linearly with angle of attack. This is validated as shown by Koning [30] since it shows that the slope of the $C_l - \alpha$ curve remains linear within the operation angle of attack range (2° - 15° , which makes the assumption valid. The next assumption states that the pitch angle of the blade changes linearly with the radial position. This assumption is valid for the design. The next assumption stated that lift acting on the blade has a greater magnitude than drag. According to Koning [30] the C_l/C_d varies between eight and twenty meaning that the assumption is valid. The next assumption stated that the blades are identical which is true for the design thus the assumption is valid. Lastly, it is assumed that lift and drag are the only aerodynamic forces acting on the blade, this is true for the design and thus the assumption is valid. An additional assumption made for the program states that the coaxial rotors are 88 % as efficient as two separate non coaxial rotors, which is confirmed by Coleman [20]. This validates all of the assumptions concerning the rotor blade properties, meaning that the formulas are validated and can thus be used for the program.

5.3.4. Local validation

To validate the working of the aerodynamic side as a whole, the value of ct/σ is calculated. This represents the thrust coefficient divided by the solidity ratio and it is the main descriptor of helicopter performance. Standard values for this parameter range from 0.12 to 0.30. The calculate multicopter value is $ct/\sigma = 0.306$. This is on the high end but because of the large number of rotors, this value is acceptable and thus validated. To validate the mass calculations, first the blade mass is validated, the blades were assumed to be of triangular shape, this needs to be validated. In Figure 5.8 the maximum thickness over chord ratio of the clf5605 is 0,05 which decreases to 0 at the trailing edge. This area of this is thus approximately equal to the triangle area and this assumption is thus valid for the mass calculation only. Thus we can assume that the area of the airfoil is approximately the area of a triangle with the base equal to the chord times the maximum thickness over chord ratio and the height being the chord length.

The next step in the mass estimation validation is the validation of the load-carrying components. Since the load-carrying components were designed from scratch using well-known formulas, in order to validate their mass, the use of the assumptions in the formulas needs to be validated. The first assumption made is that the cylindrical spars are thin-walled. The spars have a length of 8.4 m and diameters of 0.16 m, while their thickness is only 2 mm. This is a two orders of magnitude difference meaning that the thin-walled assumption is valid. The functions used to determine the diameter are considered to be valid as they are well-known and used functions. Thus the mass calculation of spars is validated.

The last step in the mass validation is the validation of the sizing methods used in the book Prouty [14]. The methods in the book are made for Earth helicopters before 1990 which greatly differs from the Martian multicopter. The hub sizing is based on centrifugal forces, which are independent of the environ-

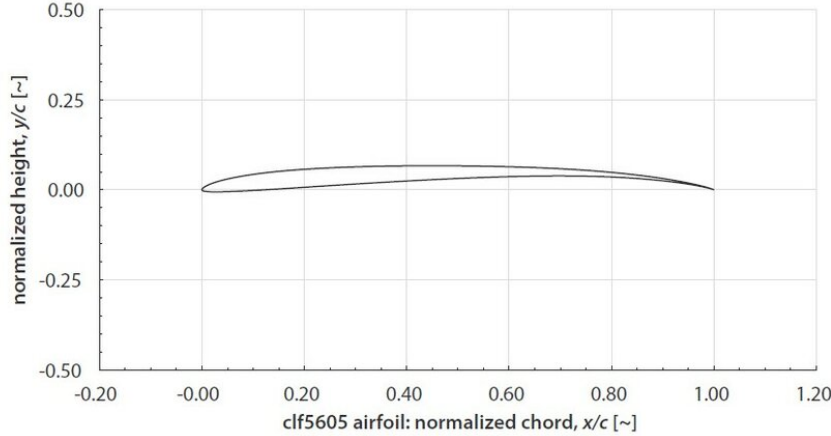


Figure 5.8: Cross section area of the clf5605 airfoil

ment. However, our design does not use swashplates and benefits from more than 30 years of innovation thus the expected mass of the hubs is 20 % of the estimated value. However, this value can not be validated, thus a safety factor for the mass of the hubs of $\pm 50\%$ is used to account for uncertainty. The fuselage mass estimation is more accurate since we assume a helicopter fuselage. The mass is based only on the wetted area which for the current design is $5 \times 3 \times 2$ m. In this case, the error is smaller than for the hubs, however, the fact that the book is based on helicopters older than 30 years still introduces uncertainties, which should be accounted for with at least $\pm 25\%$ in the sensitivity analysis.

5.3.5. Sensitivity analysis

The sensitivity analysis is split into two parts. First, the variation of aerodynamic parameters, which affects the thrust and the torque of the design. The second part of the sensitivity analysis covers the mass estimation. Here the input parameters as well as the outputs of the statistical relations will be varied in order to determine their effect on the final mass.

Table 5.6: Sensitivity analysis on aerodynamic input parameters

Input parameter	Change	Effect
Density	The Martian atmosphere density varies between 0.01 and 0.02 kg/m^3 during the year, thus this effect should be explored	Thrust and torque vary proportionally with density
Temperature	The Martian atmosphere temperature varies between 150 and 275 K which changes the speed of sound from 191 to 259 m/s	Increasing the temperature increases the torque and thrust
M_max	The maximum allowable Mach number is a design choice, and shall thus be varied from 0.5 to 0.9 to observe its impact	Thrust and torque vary quadratically with maximum Mach number
c to R ratio	The c to R ratio is a design choice and is varied from 10 to 30 to observe its impact	Increasing the twist increases both thrust and torque
Twist	Twist is a design choice and shall thus be varied to observe its impact	The twist is directly connected to the thrust and the torque produced
Number of rotors	The number of rotors is a design choice and shall thus be varied to observe its impact	The number of rotors is proportional to the thrust and torque produced
Number of blades	The number of blades is a design choice and shall thus be varied to observe its impact	The number of blades is proportional to the thrust and torque produced

The impact of density on thrust and torque is validated as the density is proportional to aerodynamic loads. The impact of temperature is correlated to the speed of sound through $V_{sound} = \sqrt{\gamma \cdot R \cdot T / M}$. The speed of sound influences the rotational velocity through tip mach number restrictions, smaller temperature gives smaller torque and thrust thus it is validated. The maximum tip mach number influences

the torque and thrust as explained in the sentence before. The chord-to-radius ratio varies the chord of the blades, and thus varies the solidity ratio which is directly correlated to thrust and torque. The twist is a parameter in both the torque and thrust formulas which makes it valid. Lastly, both the number of rotors and blades increase both the torque and thrust which is valid as increasing the area will increase the aerodynamic forces.

The sensitivity analysis for the mass estimation deals both with the input parameters and the outputs of statistical relations. Input parameters such as the blade airfoil infill percentage and fuel consumption will be varied in order to find their minimum and maximum masses. Additionally, the statistical relations based set by Coleman [20] will be varied according to the values stated in Section 5.3.4 in order to get a more accurate idea of the mass estimation.

Table 5.7: Sensitivity analysis on mass parameters

Parameter	Change	Effect
Infill percentage	The infill percentage varies between 8% and 100%	Mass varies between 144 kg and 1800 kg
Fuel consumption	The fuel consumption shall be varied by $\pm 25\%$	Mass varies between 328 kg and 546 kg
Hub sizing	The hub sizing output shall be varied by $\pm 50\%$	Mass varies between 101 kg and 304 kg
Fuselage sizing	The fuselage sizing output shall be varied by $\pm 25\%$	Mass varies between 64 kg and 106 kg
Engine sizing	The engine sizing output shall be varied according to Pratt and Whitney estimations	Mass varies between 41 kg and 81 kg

Before it is assumed that the total mass is 2700 kg from which the fuel mass is allocated, the extra fuel is added for emergencies or avoidance maneuvers. However, the actual nominal mass with enough fuel for a 1000 km trip is 2534 kg. By performing the mass sensitivity analysis it was discovered that the minimum possible mass is 1707.5 kg while the maximum possible mass is 3856.6 kg. The edge values of each parameter cover two standard deviations meaning that the possibility that each of these parameters is within the range is 95.5 %. This means that the chance that the mass of all components exceeds the maximum value is $5.7 \times 10^{-9}\%$ which is negligible. This range gives an idea of the code accuracy and with that the current mass estimation accuracy.

5.3.6. Global validation

In order to perform the global validation of the system, the question arises of what the key information output by the model is. The answer to that question is the thrust, torque, and mass of the multicopter. According to those values, the rest of the design will follow. In order to validate the program as a whole, the output of the program will be compared to the performance of a standard helicopter. If the program output values are within 20 % of the existing helicopter values, the program would be considered validated. The helicopter used for comparison will be the Hughes TH-55 Osage whose parameters³ can be seen in Table 5.8 . Using this set of inputs in the program used for calculating the multicopter parameters, the results in Table 5.9 were obtained.

Table 5.8: Hughes TH-55 Osage parameters

Airfoil	NACA0015, $CL\alpha = 0.1/\text{deg} = 5.729/\text{rad}$
Rotor radius	3.8545 m
Empty weight	406 k g, 3923 N
Loaded weight	703 kg, 6896 N
Twist root	$2^\circ = 0.0349 \text{ rad}$
Twist tip	$8^\circ = 0.1395 \text{ rad}$
Omega	(400-530) rpm = (41.9-55.5) rad/s
Chord to radius	1/20
Blades	3
Rotors	1

³URL: http://www.flugzeuginfo.net/acdata_php/acdata_269_en.php [cited 2023-05-22]

Table 5.9: Comparison of the results and the reference values

Variable	Low rpm take-off	High rpm take-off	Low rpm cruise	High rpm cruise
Thrust	3400 N	7600 N	6100 N	10300 N
Reference Thrust	3800 N	7000 N	5300 N	9300 N
Torque	3800 Nm	6600 Nm	3200 Nm	6700 Nm
Reference Torque	Not available	Not available	Not available	Not available

The expected thrust values at take off are based on the loaded and empty weight. The take-off thrust at highest rpm needs to be higher than the loaded weight to allow for upward acceleration. The take-off thrust at the lowest rpm needs to be slightly lower than the empty weight to allow for landing. The cruise values are based on the the weight of the aircraft as well as the lower density of the air at cruise and the drag produced by the helicopter. At the lowest rpm, the helicopter is able to cruise at the empty weight. At the high rpm, the helicopter is able to cruise at the loaded weight. Thus the take-off values for thrust differ by 10 % while the thrust values at cruise differ by up to 13 %. It is also important to note that the low rpm values differed more than the high rpm values which can be further looked at. However since all of these are within the before mentioned 20 % we can say that the thrust values are validated. There are no available values for the torque of the rotor during cruise and take-off thus those values could not be validated. Lastly, the mass calculation was validated. The mass calculation predicted the helicopter empty mass to be 369 kg. This is within the 10 % of the actual value, this is considered enough to validate the mass of the multicopter. However, it is important to note that the mass is underestimated and it is possible that the mass would exceed the 3000 kg target. To conclude, the model over-predicts the thrust produced by 10 % to 13 % while under-predicting the mass by 10 %, which is already taken into account in the from of contingencies. However, both of those are within the aforementioned 20 % meaning that the program is validated.

Verification and Validation Plan

Preliminary Design

This chapter details the Verification and Validation plan and who is accountable for each section of the Verification and Validation. Section 6.1 details who is responsible for the verification. Section 6.2 dives into several verification and validation methods. Section 6.3 applies several Verification and Validation methods to the model. Section 6.4 proposes a plan for verification and validation for the report's future, from preliminary design to detailed design and the final product.

6.1. Responsibilities

By Timo de Kemp

Every engineer is responsible for creating unit tests for their code before the functions have been created. This will ensure that the engineers are not biased in creating the unit tests after their functions have been written. When multiple functions from the engineer work together, the engineer will design tests to show that the functions have the correct inputs and outputs. The systems and integration engineers are responsible for making sure that the functions of different departments/engineers can be appropriately integrated into the primary function. This includes designing tests and ensuring the engineers create functions that work together.

6.2. Verification and Validation methods

By Timo de Kemp, Freek Braspenning

The methods to do verification and validation are analysis, inspection, demonstration, and testing. What these terms mean will be explained in the next paragraphs [31].

- **Analysis:** The use of mathematical modeling and analytical techniques to determine the compliance of the design with its requirements or the code with its expected value based on calculated data.
- **Inspection:** Determination of requirement compliance by visual inspection, often used to verify physical design features.
- **Demonstration:** Show that the end product achieves a requirement(verification) or customer expectation(validation). It differentiates from testing by the lack of detailed data collection.
- **Testing:** A realized end product, with detailed data collection, is used to verify or validate its performance.

6.3. Model Verification and Validation

By Timo de Kemp

This section implements and applies some of the previously discussed Verification and Validation methods to the model.

6.3.1. Model verification

Unit tests Unit tests will be done for the functions created. These unit tests will include tests for the order of magnitude expected, a range of expected numbers, and extreme values.

Module tests The connection between other functions is tested in module testing. The module is a collection of related functions that collectively provide input to the subsystem. Testing of these modules can be done in various ways. In this project's scope, the module tests that will be performed are extreme value testing, sensitivity analysis, and integration testing.

Subsystem tests A subsystem consists of multiple modules, and the interaction between these modules is tested with subsystem tests. These tests include but are not limited to integrated tests and acceptance tests.

System tests The system is the collection of all subsystems. The system is tested for the integration of the subsystems. These tests include methods, as discussed in module tests and subsystem tests.

6.3.2. Model validation

By Freek Braspenning

Once the model is verified, its validity is tested with respect to experimental data. This ensures that the suitable model has been solved to represent reality accurately. The model will be inputted with the same conditions for the experimental setup. Martian conditions should be approximated to the best of your abilities when testing on Earth. Another method to validate the model is to run the model using Earth parameters and compare the results to experimental data.

Experiments such as wind tunnel tests, scaled models, and prototype test flights will validate the model data. In addition, the scaled models can be validated for aerodynamics, structures, and transportation. Finally, prototypes can be flown on Earth or Mars to simulate relevant flow characteristics.

6.4. Product Verification and Validation

After the conceptual design phase, the team will present a design that should meet all requirements. This product will be verified and validated in various ways. During the conceptual design phase, it can be verified using simulations and analysis of the model, but also limited testing such as wind tunnel tests.

Verification and validation processes are continued throughout the future of the project. With further development of the design concept, more thorough verification and validation methods are used. These methods include testing on prototypes, demonstration of working concepts, and inspections of the final product.

Throughout the project, the design is validated with respect to the requirements. The methods of validation change as the design takes shape. At the start, most of the validation tests would be analyzed, while later on, prototypes could be tested to validate the design.

Testing methods for validating are proposed in Table 6.1 for a select number of requirements.

Table 6.1: Driving requirements

Identifier	Description	Verification method
REQ-ASTR-SAFE-01	The system shall not produce more than <TBD>positive gs in any direction.	Testing/Analysis
REQ-SAG-REUS-03	The system's assembly process shall be repeatable.	Demonstration
REQ-GOPS-ACT-ASS-01	The system shall be able to be assembled by 2 astronauts.	Demonstration
REQ-AERO-LFT-02	The aerodynamic system shall have a maximum lift coefficient of <TBD>.	Testing
REQ-AERO-LFT-04	The aerodynamic system shall have a stall angle of <TBD>degrees.	Testing
REQ-STG-PAY-02	The system shall be able to hold 100 kg of payload.	Demonstration
REQ-PWR-ELEC-01	There shall be <TBD>Watts of power available to power all essential systems.	Analysis
REQ-ETHC-02	The system shall not pollute the Martian environment.	Analysis
REQ-CLMB-01	The climb rate at take-off altitude shall be at least <TBD>m/s.	Testing
Key requirements		
REQ-SAG-LF-03	The system shall obtain power from sources available on Mars.	Analysis
REQ-LCD-LVEH-SIZE-01	The system shall have a volume of less than <TBD>[m ³].	Inspection
REQ-LFSP-AIR-01	The system shall provide breathable air to the astronauts.	Testing
REQ-CRUS-05	The nominal cruise speed shall be 111 m/s.	Demonstration

Trade-Off

By Dominik Stiller

A trade-off is performed among the five options to find the optimal design for our mission. Finally, the results are checked for robustness through a sensitivity analysis. This chapter details the methodology in Section 7.1 and the results of the trade-off in Section 7.2.

7.1. Methodology

We used a traditional numerical trade-off. This method requires weighted criteria, assigning a score per design option. The steps to choose the optimal design were as follows:

1. Decide on criteria candidates.
2. Determine weights for all criteria candidates.
3. Define scoring categories (unacceptable, good, ...) and their numerical value.
4. Determine how scoring categories are assigned for each criterion.
5. Perform preliminary sizing for all design options to estimate criteria values (Chapter 4).
6. Select significant criteria from candidates.
7. Determine optimal option from total scores.
8. Check the robustness of results using sensitivity analysis.

Infeasible options were already eliminated in the baseline phase. This means that all effort for preliminary sizing was focused on promising concepts.

Determining a total score for something as complex as an aircraft design is challenging: disparate criteria such as range and sustainability must be combined, and qualitative criteria such as feasibility must be quantified. These challenges were considered throughout the process to achieve an unbiased and representative result. Note that the actual process was less linear than presented here, and some internal iterations were necessary.

7.1.1. Selection of criteria

Before starting the preliminary sizing, our group agreed on a range of criteria candidates that may be relevant for the trade-off. These criteria came from the requirements and consideration of differences between the designs. Both qualitative and quantitative aspects were considered. The quantitative candidates were:

- **Range at 350 kg payload:** The range at the design payload of 350 kg (250 kg for two suited astronauts + 100 kg for cargo) should be maximized. This would reduce the need for refueling.
- **Max. payload at 1000 km range:** The maximum payload at the design range of 1000 km should be maximized. This may allow the transportation of another astronaut or more cargo.
- **Cruise speed:** The cruise speed should be maximized (within Mach limits). This reduces travel time.
- **MTOM:** The MTOM should be minimized.
- **Landing/take-off distance:** The landing/take-off distance should be minimized, VTOL (zero distance) would be optimal. A longer distance would restrict landing sites due to craters and rocks.
- **Availability:** The availability depending on diurnal, seasonal, and weather-related conditions should be maximized. For example, a solar-powered design may be limited to daytime flight.
- **Packed volume:** The volume of the aircraft disassembled for transport from Earth to Mars should be minimized. This allows greater flexibility with launchers or shipment of multiple aircraft to Mars at once.
- **Number of disassembled parts:** The number of parts into which the aircraft is disassembled for transport from Earth to Mars should be minimized. This facilitates assembly at the destination.

The qualitative candidates were:

- **Feasibility:** The feasibility, or probability of the design being successful, should be maximized. While crewed flight on Mars has yet to be attempted, technologies that are flight-proven in Earth conditions (or even Mars conditions) should be preferred. Also, critical assumptions with large uncertainties reduce feasibility.
- **Sustainability:** The sustainability should be maximized. The aircraft should limit the negative impact on the future populations of Earth and Mars. Important aspects are ISRU, pollution, and recyclability.
- **Assembly complexity:** The assembly complexity should be minimized. There is little infrastructure and personnel on Mars to help with assembly. Therefore, the aircraft should be assemblable with just two astronauts and simple tools.
- **Safety:** The safety should be maximized. High safety standards apply to crewed flights.

We aimed to select four to six criteria for the trade-off since more would dilute the relevant differences between designs. The selection was based on (1) the importance due to customer requirements and group discussion, (2) the spread between design options, and (3) whether the values can be determined through preliminary sizing.

The selected criteria and justifications are in Table 7.1. Four criteria were chosen: "range at 350 kg payload," "landing/take-off distance," "feasibility," and "sustainability."

Table 7.1: Candidate criteria and why they were (or were not) selected. Four are selected (marked by ✓), and seven are either not distinguishing enough or hard to quantify with only preliminary sizing.

Criterion	Justification
✓ Range at 350 kg payload	Important due to user requirements
✓ Landing/take-off distance	Large differences between VTOL/HTOL designs; important for possible landing sites
✓ Feasibility	Design feasibility impacts the development time and subsequent cost required to develop the design as well as how realistic it is to build; low feasibility jeopardizes all other aspects
✓ Sustainability	Sustainability is crucial as the design should limit its impact on environment of Earth and Mars
Assembly Complexity	Important due to the limited infrastructure available, but also all designs could be designed for simplified assembly (e.g., make wings and rotors foldable instead of attachable)
Max. payload at 1000 km range	Important due to user requirements, but high correlation with "range at 350 km payload"
Cruise speed	All designs have a similar cruise speed of 400 km/h
MTOM	All designs have a design MTOM of 2700 kg; if below, the difference is filled with fuel, which makes designs more comparable under "range at 350 km payload"
Availability	All designs have an availability greater than 90 %
Packed volume	All designs easily fit into payload fairings of possible launchers
Safety	Safety highly depends on detailed design (e.g., cockpit structure absorbs crash energy, protruding parts like rotors break away during crash); all designs have one-engine-out procedures and similar crash protection; higher risks are acceptable for experimental aircraft

7.1.2. Weighting of criteria

More weight can be given to essential criteria. Initially, we considered different weights for the criteria. However, no clear differences in importance could be determined. Therefore, we decided to weigh all criteria equally but analyze whether using different weights between 1 and 5 would have changed the outcome. This sensitivity analysis is described in Section 7.2.

7.1.3. Scoring of criteria values

To compare values of disparate criteria, we scored them among five categories ranging from "unacceptable" to "exceptional." For the quantitative criteria, we defined numerical intervals for each category. For qualitative criteria, the category was determined based on multiple sub-criteria.

The scoring categories are shown in Table 7.3. The categories were assigned as follows:

- **Range at 350 km payload:** The nominal range from the user requirements is 1000 km. The range is "good" if it is within 10 % of 1000 km. The performance is "exceptional" if the range is more than twice the requirement and "unacceptable" if below 700 km.
- **Landing/take-off distance:** A longer distance increases the risk of collision with rocks or interference from craters. VTOL (i.e., a distance of 0 m) circumvents these risks. However, the two fixed-wing aircraft are the only options that require a non-zero distance of 2000 m. Therefore, this criterion is essentially binary and may be sensitive to the interval boundary. While statistical analyses of rock and crater distributions to find physically meaningful boundaries were considered, they proved too complex for this trade-off. Therefore, we used a more pragmatic approach: the 2000 m are not "unacceptable" (we could design a robust landing gear or target flat, explicit landing sites) but are also not "good" (the landing sites will likely be somewhat limited). Therefore, the 2000 m distance is considered "acceptable," which was approved by the customer. The effect of this choice was checked in the sensitivity analysis.
- **Sustainability:** The sustainability aspect of the trade-off is broken down into four criteria. (1) The power or propulsion system should prevent emitting foreign molecules into the atmosphere (e.g., violated by a Mg-CO₂ engine emitting solid carbon). For all systems, the existence of power generation emissions negatively impacts the sustainability of the design. (2) Emissions due to the lifting system should be prevented (e.g., violated by leaking hydrogen of the airship). (3) Recyclability of the aircraft structures improves sustainability, as the aircraft's end-of-life is crucial. Metals and thermoplastics are preferable to CFRP (recycled fibers usually do not meet stringent performance requirements and are rarely recycled in practice [32]). (4) The use of batteries on the aircraft positively affects the sustainability of the system, as the technologies will be compatible with Earth technologies (batteries are a cornerstone for sustainable energy for Earth and thus heavily researched), source its power from renewable sources, and allow for re-using of the batteries as static energy storage for future missions.
- **Feasibility:** The feasibility of the design is primarily based on the Technology Readiness Level (TRL)¹ of the power generation, thrust generation, and control system. The score is assigned as these three systems' lowest TRL. In the event of a draw, the number of similar existing designs is used to distinguish the remaining designs (e.g., there is more precedent for fixed-wing aircraft than tiltrotors as more designs exist and have been flight-proven).

The trade-off results were based on the expected value for each criterion. However, we also derived best-case and worst-case values. This was useful for checking the significance of trade-off results, the effect of sizing uncertainties, and sensitivity analysis for weighting. Different assumptions, which are detailed in Table 7.2, were used for best-case/worst-case values of the quantitative criteria. For the qualitative criteria, the score category was shifted up/down (e.g., "great" becomes "good"/"exceptional").

¹Multiple definitions of TRLs exist. We use the following relevant for our subsystems: 4 = technology validated in a laboratory, 5 = technology validated in the Earth environment, 6 = technology demonstrated in the Earth environment, and 9 = technology flight-proven in the Mars environment. For example, the Mg-CO₂ engine has TRL 4, while electric rotor propulsion has TRL 9.

Table 7.2: Assumptions for expected, best-case and worst-case scenarios. The atmospheric density is adjusted for all designs based on the expected range at zero elevation. The Mg-CO₂ engine efficiency is adjusted for the internal combustion engine only (not for jet engines).

	Expected	Best case	Worst case
General	Atmos. density = 0.015 kg/m ³	Atmos. density = 0.010 kg/m ³	Atmos. density = 0.020 kg/m ³
Blended wing	Take-off distance = 2000 m	Take-off distance = 3000 m	Take-off distance = 1000 m
Biplane	Take-off distance = 2000 m	Landing distance = 3000 m	Take-off distance = 1000 m
Tiltrotor	—	—	—
Multicopter	Cruise fuel consumption = 0.394 kg/kWh (better than hover, Mg-CO ₂ is less efficient than fossil fuels); engine mass = 61 kg	Cruise fuel consumption = 0.224 kg/kWh (better than hover, Mg-CO ₂ is as efficient as fossil fuels); engine mass = 41 kg	Cruise fuel consumption = 0.448 kg/kWh (same as hover); engine mass = 81 kg
Airship	Skin thickness = 0.1 mm	Skin thickness = 0.1 mm	Skin thickness = 1 mm

Each scoring category was then assigned a numerical score between zero and four. No points were gained for an "unacceptable" design, while four were given to "exceptional" designs. The categories in between used consecutive integers, i.e., a linear scale. The numerical score for a certain value can be obtained from the provided rubric (Table 7.3), which was described above.

The total score was then calculated based on each criterion's weights and the numerical scores of the assigned category. The minimum possible total score is 0, and the maximum possible total score is 16 (if all criteria are "exceptional"). The scale for the total weighted score was then linearly stretched out to 0–100. This is the score that is discussed subsequently in the trade-off results.

The total score can be interpreted as follows:

- **0:** all criteria are "unacceptable"
- **0–25:** on average, the criteria are between "unacceptable" and "acceptable"
- **25–50:** on average, the criteria are between "acceptable" and "good"
- **50–75:** on average, the criteria are between "good" and "great"
- **75–100:** on average, the criteria are between "great" and "exceptional"
- **100:** all criteria are "exceptional"

7.2. Results

The trade-off results are shown visually in Figure 7.1 and summarized with criteria values in Table 7.4. For the expected values of each criterion, the tiltrotor wins with a score of 81, followed by the multicopter with a score of 62. The airship scores the lowest at 38 points. The fixed-wing aircraft rank between the airship and the multicopter.

The tiltrotor has the lowest spread between the best case and worst case (69–94), which indicates that the final design is likely to be in the range of the preliminary sizing. In the best case, the multicopter is on par with the expected case of the tiltrotor. However, despite some overlap, the tiltrotor range is significantly above the multicopter range. The best-case scores for the blended wing and biplane aircraft are around the expected score for the multicopter, while the airship scores only 56, even in the best case.

The robustness of the results was analyzed through a sensitivity analysis. The trade-off was performed again with the expected values, but the initially equal weights of 1 of each criterion were perturbed 1000 times. This was done by uniformly sampling weights between 1 and 5. This means that a one criterion could be up to five times more important than the others. The robustness is then measured by the inter-

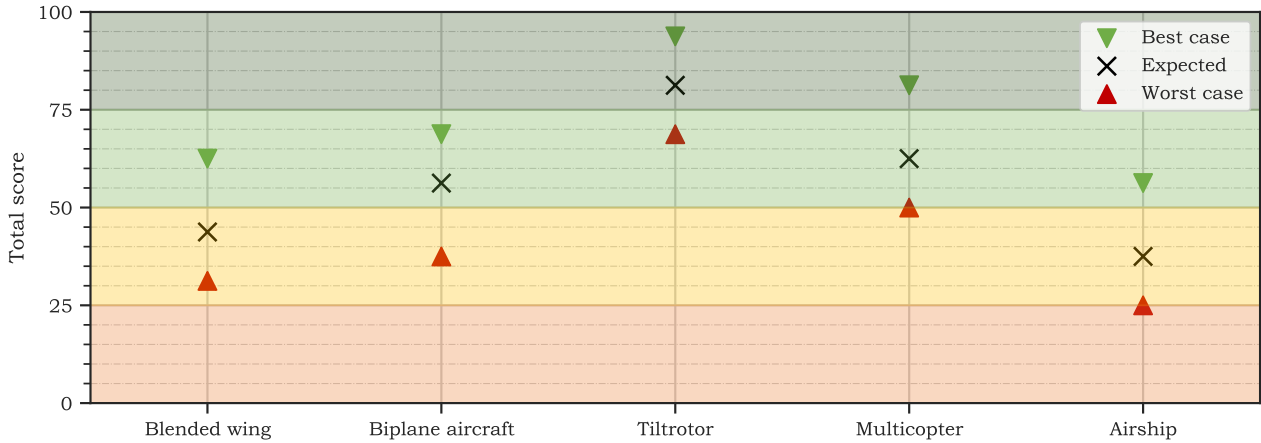


Figure 7.1: Results of the trade-off. The tiltrotor wins for the expected case, par with the multicopter's best case.

quartile range (IQR) of the resulting total scores (corresponds to box height in box plots; smaller IQR = more robust). Note that we do not perturb the actual criterion values (e.g., the range for the multicopter) since the best-case and worst-case scenarios cover this in a more physical manner.

The sensitivity analysis results are shown in Figure 7.2. The relative ranking is very similar to the results from Figure 7.1. In general, the better designs are also more robust to perturbations. The airship score is the most sensitive ($IQR = 11$). The tiltrotor is the most robust design ($IQR = 3$) since it scores high under all criteria. Even more importantly, the whiskers of the tiltrotor box do not overlap much with any other box, which means that there is only a low chance that another design is actually better than the tiltrotor.

We also performed a targeted sensitivity analysis for the "landing/take-off distance" criterion since the two fixed-wing design scores may be sensitive to the boundary (see Section 7.1.3). Regularly, the landing distance of 2000 m is considered "acceptable." If considered "good," the biplane aircraft would be on par with the multicopter in the expected cases, while it would be better than the biplane if 2000 m were considered "great." However, the tiltrotor is the best option in any case.

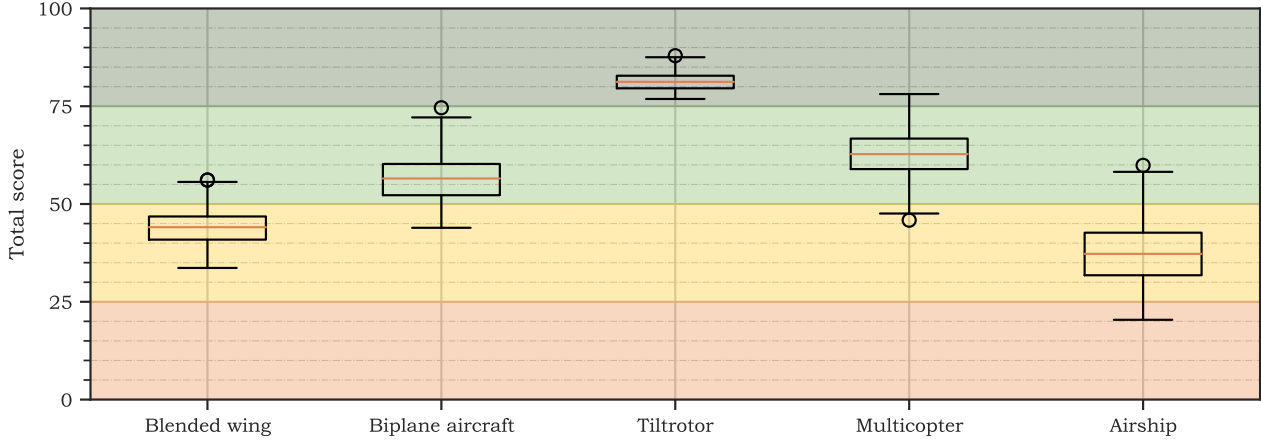


Figure 7.2: Sensitivity analysis for the trade-off. The boxes denote the IQR, while the whiskers extend from $Q1 - 1.5IQR$ to $Q3 + 1.5IQR$. The criteria weights are perturbed by uniformly sampling weights between 1 and 5. The outcome of the trade-off is robust to these perturbations. Designs with higher scores are less sensitive.

From these results, the tiltrotor is the optimal option under the chosen criteria and will be designed in more detail going forward. This choice is robust under perturbed weights and different assumptions. The multi-copter is the second-best option, but possibly matched by the fixed-wing aircraft HTOL is penalized less. The airship is the worst due to its unacceptable range. Among the fixed-wing aircraft, the biplane aircraft performs better than the flying wing.

Table 7.3: Score assignment rubric for each criterion. Intervals are given for quantitative criteria.

<i>Score value</i>	Unacceptable 0	Acceptable 1	Good 2	Great 3	Exceptional 4
Range at 350 kg payload [km]	< 700	[700, 900)	[900, 1100)	[1100, 2000)	≥ 2000
Landing/take-off distance [m]	> 5000	[5000, 1500)	[1500, 500)	[500, 1)	0 (VTOL)
Feasibility	Min. TRL $\in [1, 4]$	Min. TRL $\in [4, 6]$ and <1000 existing designs	Min. TRL $\in [4, 6]$ and >1000 existing designs	Min. TRL $\in [6, 9]$	All TRL = 9
Sustainability	No criteria fulfilled	1 criterion fulfilled	2 criteria fulfilled	3 criteria fulfilled	All 4 criteria fulfilled

Table 7.4: Trade-off summary including criteria values and scores. The total score in the last column indicates the overall goodness of the design. The tiltrotor design has the highest score, which is robust to perturbations and is selected.

	Range at 350 kg payload [km]		Landing/take-off distance [m]		Feasibility		Sustainability		Score
<i>Weight</i>	1		1		1		1		
Blended wing	1779	GREAT	2000	ACCEPTABLE	Min. TRL of 4 (Power) and <1000 existing designs	ACCEPTABLE	Emits carbon, and the energy source is not renewable	GOOD	44
Biplane aircraft	2157	EXCEPTIONAL	2000	ACCEPTABLE	Min. TRL of 4 (Power) and >1000 existing designs	GOOD	Emits carbon, and the energy source is not renewable	GOOD	56
✓ Tiltrotor	1885	GREAT	0	EXCEPTIONAL	Min. TRL of 6 (Control)	GREAT	Rotor blades are not recyclable, but uses batteries	GREAT	81
Multicopter	1270	GREAT	0	EXCEPTIONAL	Min. TRL of 4 (Power) and <1000 existing designs	ACCEPTABLE	The energy source is not renewable, and rotor blades are not recyclable	GOOD	62
Airship	480	UNACCEPTABLE	0	EXCEPTIONAL	Min. TRL of 4 (Power) and <1000 existing designs	ACCEPTABLE	Emits carbon and hydrogen, and the energy source is not renewable	ACCEPTABLE	38

Technical Risk Assessment

By Sebastian Harris, Freek Braspenning

The Technical Risk Assessment can be conducted once more on the final design. This follows a set methodology, described in Section 8.1. Next, the risks from previous reports are summarized in Section 8.2. Finally, the risks stemming from this design phase are researched and assessed in Section 8.3.

8.1. Methodology

Within the Risk Assessment process, various methods are available to both size risks and their impact. In the context of this report, the scale in Table 8.1 is used.

Table 8.1: Score associated with probabilities and impacts of the risks

Scale	Probability	Impact
5	Very High ($p \geq 95\%$)	Catastrophic (Complete Mission Failure)
4	High ($60\% \leq p < 95\%$)	Partial Mission Failure
3	Medium ($30\% \leq p < 60\%$)	Moderate performance reduction
2	Low ($1\% \leq p < 30\%$)	Small performance reduction
1	Very Low ($p < 1\%$)	Negligible

After recalling the risks identified and assessed in the previous reports, additional risks can be identified as the chosen design is known.

8.2. Risks from previous reports

For the sake of conciseness, the risks listed in previous reports will only be mentioned when their original risk was unacceptable. The risks in Table 8.2 were identified.

Table 8.2: List of Risks from previous reports

Risk ID	Description	Risk ID	Description
R-PREP-01	Imperfections in manufacturing	R-OP-06	Improper Maintenance
R-PREP-02	Damage during transport	R-TO-03	Dust clogs any air intake
R-PREP-03	Errors in Assembly	R-TO-06	Insufficient runway length
R-PREP-04	Missing items in package	R-TO-07	Insufficient lift produced
R-PREP-05	Launcher failure	R-CR-01	Engine Failure
R-STAT-01	Dust Storm leading to aircraft damage	R-CR-02	Dust clogs any air intake
R-STAT-02	Damage due to strong winds	R-CR-03	Control surface failure
R-STAT-03	Damage due to radiation	R-CR-04	Corrupted on-board computer
R-STAT-04	Incident when refueling/recharging	R-CR-05	Structural failure
R-STAT-05	Pre-flight procedures fail	R-LD-01	Engine failure
R-STAT-06	Unable to refill energy storage	R-LD-02	Dust clogs any air intake
R-STAT-07	Failure to assemble on site	R-LD-03	Control surface failure
R-OP-01	Life support failure	R-LD-04	Non-functional landing gear
R-OP-03	Compromised thermal insulation	R-LD-08	Landing site is too small
R-OP-04	Astronauts unable to operate the aircraft	R-LD-09	Landing gear failure
R-OP-05	Power system failure		

8.3. Additional risks

With the final design settled additional concept-specific risks arise. These risks are listed in Table 8.3.

Table 8.3: Additional Risks

Risk ID	Description	Probability (1-5)	Impact (1-5)
R-AR-01	Faulty batteries	1	5
R-AR-02	Transmission failure [33]	1	4
R-AR-03	Gearbox Failure [33]	1	4
R-AR-04	Hydraulic failure	1	4
R-AR-05	Avionics failure[34]	1	3
R-AR-06	Brownout [35]	4	3
R-AR-07	Short-circuiting of electrical components	1	4
R-AR-08	Rotor failure	1	4
R-AR-09	Autopilot failure [33]	1	2
R-AR-10	Instrument failure [33]	1	3
R-AR-11	Temperature control failure [36]	1	3
R-AR-12	Astronauts unresponsive [37]	1	5
R-AR-13	Battery Ageing	5	3
R-AR-14	Vortex Ring State ¹	3	3
R-AR-15	Center of gravity shift	2	5

To facilitate understanding, both Brownouts and Vortex Ring States will be further explained. A brownout consists of the dust thrown up by the rotors to cloud the pilot's vision, resulting in a total lack of visibility. This lack of vision can lead to crashes and errors in piloting. Considering the decreased gravity on Mars, these brownouts could last much longer as the particles will not settle. However, due to the decreased viscosity of the atmosphere, the entrainment of particles will also be decreased. Separately, the vortex ring state consists of a situation in descent where the wake of the rotor causes the airflow to rotate over and re-enter the flow of the rotor. This leads to a large decrease in thrust, which is not always done symmetrically, potentially rolling the aircraft. From the data present in Table 8.3, the design risk matrix can be created in Table 8.4

Table 8.4: Additional Design risk matrix

		Probability				
		Very Low (1)	Low (2)	Moderate (3)	High (4)	Very High (5)
Impact	Catastrophic (5)	R-AR-01, R-AR-12	R-AR-15			
	Critical (4)	R-AR-02, R-AR-03, R-AR-04, R-AR-07, R-AR-08				
	Moderate (3)	R-AR-05, R-AR-10, R-AR-11		R-AR-14	R-AR-06	R-AR-13
	Marginal (2)	R-AR-09				
	Negligible (1)					

¹URL: <https://www.skybrary.aero/articles/vortex-ring> [cited 2023-06-02]

Table 8.5: Mitigation of Additional Risks

Risk ID	Mitigation	Probability (1-5)	Impact (1-5)
R-AR-01	Isolate battery storage and regularly inspect	1	3 (-2)
R-AR-02	Redundant transmission	1	1 (-3)
R-AR-03	Redundant gearbox	1	2 (-2)
R-AR-04	Redundancy in the hydraulic	1	1(-3)
R-AR-05	Redundant Avionics	1	1 (-2)
R-AR-06	Use Infrared Imaging	4	1 (-2)
R-AR-07	Use fuses	1	3 (-1)
R-AR-08	Ensure Rotor and Cockpit are not aligned	1	2 (-2)
R-AR-09	Install alert system and manual override	1	1(-1)
R-AR-10	Redundancy in instruments	1	1(-2)
R-AR-11	Redundancy in temperature control failure	1	3 (-2)
R-AR-12	Automatically engage autopilot when crew is unresponsive	1	3 (-2)
R-AR-13	Monitor battery health and performance	5	1 (-2)
R-AR-14	Set limit on descent speed and train crew in Vuichard Correcting Technique	2 (-1)	1 (-2)
R-AR-15	Calculate the center of gravity when loading payload and alert astronauts if too close to the neutral point	1(-1)	5

With the data present in Table 8.5, the new mitigated design risk matrix can be created, as seen in Table 8.6. Compared to Table 8.4 the risks have shifted to the bottom left, reducing their probability and consequence.

Table 8.6: Mitigated Design risk matrix

		Probability				
		Very Low (1)	Low (2)	Moderate (3)	High (4)	Very High (5)
Impact	Catastrophic (5)	R-AR-15				
	Critical (4)					
	Moderate (3)	R-AR-01, R-AR-07, R-AR-11, R-AR-12				
	Marginal (2)	R-AR-03, R-AR-08				
	Negligible (1)	R-AR-02, R-AR-04, R-AR-05, R-AR-09, R-AR-10	R-AR-14		R-AR-06	R-AR-13

As visible, all risks determined in this phase have been mitigated. In the following stage of the design process, these risk mitigation steps will be implemented in the final design.

Furthermore, despite the mitigation of the risks, the failure of a main component, such as an engine or a rotor, will have a strong impact on the mission. Although this will be further investigated in the next design phase, it can still be noted that the design possesses many safety advantages. In the event of an engine failure, the tiltrotor is able to either autorotate in the situation where it is moving vertically or glide similarly to a conventional aircraft. This combination should ensure smooth landings no matter the engine configuration. The design can also take off by producing thrust diagonally, thus producing both lift and forward thrust, which will, in turn, be facilitated by the wing.

Sustainable Development Strategy

By Thomas van de Pavoordt

To design for sustainability, firstly, a definition of sustainability was agreed upon. We define sustainability after Brundtland [38]:

"Meeting the needs of the present without compromising the ability of future generations to meet their own needs."

Since the future of humanity may be multi-planetary, we need to consider the needs of future generations on both Earth and Mars. This means that both the development, design, and manufacturing of the system on Earth and the operations of the system on Mars should be sustainable.

During this preliminary design phase of all the different options, sustainability is becoming increasingly integrated. Each design concept was created with the goal of sustainability in mind, especially given the fact that it is a customer requirement to only utilize in-situ available resources (REQ-USER-SUST-01). Moreover, from the sustainability definition, requirements were derived concerning manufacturing on Earth (REQ-MNFCT-TXIC-01 - REQ-MNFCT-TXIC-02), pollution on Mars (REQ-SUST-04), and the use of recyclable materials (REQ-SUST-02). As seen in the baseline report, these requirements will have to be met and are therefore integral to our design.

Additionally, in the trade-off process, sustainability was considered as a trade-off criterion. This ensured that all designs aimed towards scoring as high as possible in this category. The tiltrotor design concept was equipped with batteries and a propulsion system powered by electrical (solar) energy, while the jet engine designs use magnesium and carbon dioxide, both of which are available on Mars. This ensured that the in situ resource use requirement was met. Sustainability was one of the stand out criteria for the tiltrotor and contributed to the final design choice as can be seen in Table 7.1 in Chapter 7. The tiltrotor design uses completely renewable energy and ensures no pollution of the Martian atmosphere, thus contributing to the sustainable development strategy.

Only in the detailed conceptual design phase of the report it is possible to dive deeper into the effects of the design on the sustainability goals. This means, but is not limited to, assessment of the materials used, how these materials are manufactured, what their recyclability is, and their end-of-life plan. It will have to be assessed what footprint the design will leave on Mars and whether this can be considered polluting. The assembly as well as the transportation from Earth to Mars will have to be assessed and their impact on Earth's atmosphere will be evaluated. The life span of the aircraft will have to be considered along with the re-usability of the system. All these aspects, and more, are inherent to the detailed conceptual design and thus, the sustainability manager will prepare to enforce these during the final phase.

Summarizing, the following new sustainability goals of the system and project have been set:

- Use in-situ, renewable fuels
- Use non-toxic, abundant, recyclable materials
- Evaluate manufacturing processes and their impact on Earth
- Evaluate assembly process and its impact on both Earth and Mars
- Evaluate the impact of transportation on Earth atmosphere
- Evaluate the impact of pollution on the Martian atmosphere and potential life on Mars
- Evaluate re-usability of system
- Evaluate end-of-life plan

These goals are set in a larger sustainability framework consisting of multiple parts. Life Cycle Thinking (LCT) is implemented by evaluating the manufacturing processes, the operation of the system and the end-of-life plan. LCT contains a step-by-step plan from Life Cycle Assessment (LCA), which identifies all emissions and utilized resources throughout the life cycle, to Life Cycle Management (LCM), which aims to minimize the environmental impact using tools such as input-output analysis, cumulative en-

ergy requirements analysis, and risk assessment.¹ Next, goals and targets have been set, which are vital for tracking progress and quantifying the effectiveness of said sustainability goals. Careful reporting and communication will be employed within the sustainability framework to ensure continuous improvement in the sustainability goals. The sustainability manager will oversee the framework and inspect the progress in weekly meetings.

¹URL: <https://www.lifecycleinitiative.org/activities/what-is-life-cycle-thinking/> [cited 2023-06-02]

Project Logic

This chapter describes the logistics of the product development, as well as the agenda for the final report. Section 10.1 shows the development of the chosen design after the preliminary design phase. The operational and logistic flow of the product is provided by Section 10.2. Section 10.3 explores the iteration phase of the preliminary design. Section 10.5, Section 10.4 and Section 10.6 provide the updated Work Flow Diagram, Work Breakdown Structure, and Gantt Chart, respectively, for the final phase of the design.

10.1. Project description & development logic

By Timo de Kemp

The Project Description & Development Logic (PD&DL) diagram describes the stages of the product production and operation which take place after the preliminary design has been finalized. The first step is to finalize the design in the detailed design phase after which it will be produced and tested. Once testing is complete the design and the crew are prepared for operation. The final stage of the project is the operation on Mars, which ends with the End of Life operations.

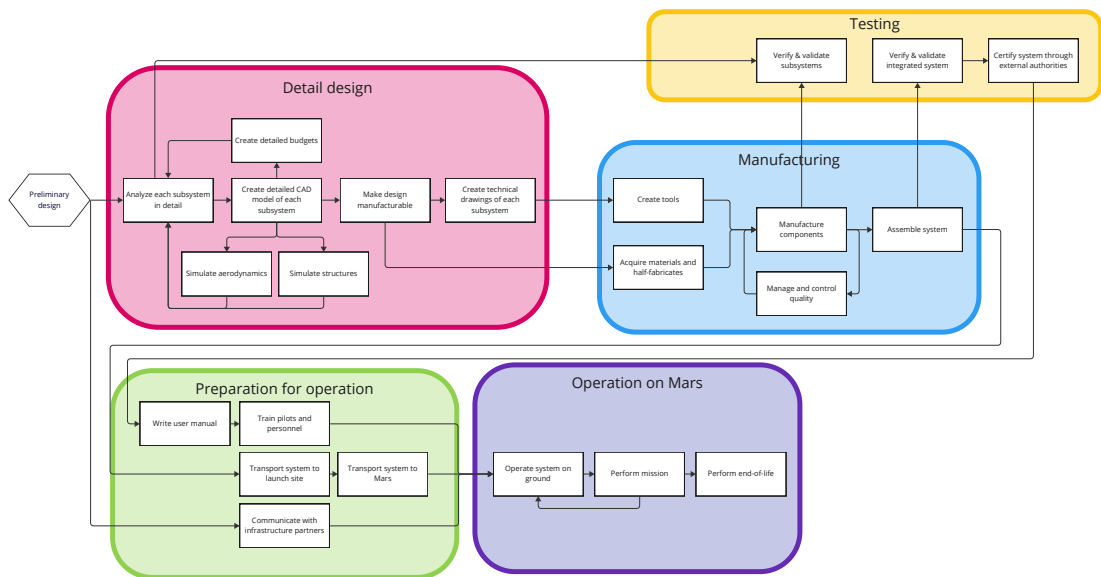


Figure 10.1: Project Design & Development Logic for post preliminary sizing phase

10.2. Operations and logistics description

By Timo de Kemp

In this section the operations and logistic concept for the production and operation phase of the aircraft will be discussed. As can be seen in Figure 10.2, the flowchart starts from semi-finished materials i.e. processed metal or plastic pallets. These have to be transported to the manufacturing facility and manufactured into the sub-assemblies. The sub-assemblies will be transported to Mars. As little infrastructure is assumed on Mars, therefore only the final assembly will be done on Mars. As this assembly consists of multiple sub-assemblies will have to be transported to Mars, the three dots in Figure 10.2 indicate that this number is still to be determined.

Since only the assembly is performed on Mars, additional equipment needs to be transported. The same equipment can be used for the assembly as well as maintenance if necessary. The equipment for assembly will consist, but is not limited to, assembly jigs, fasteners, fastener tools, and heavy duty machines.

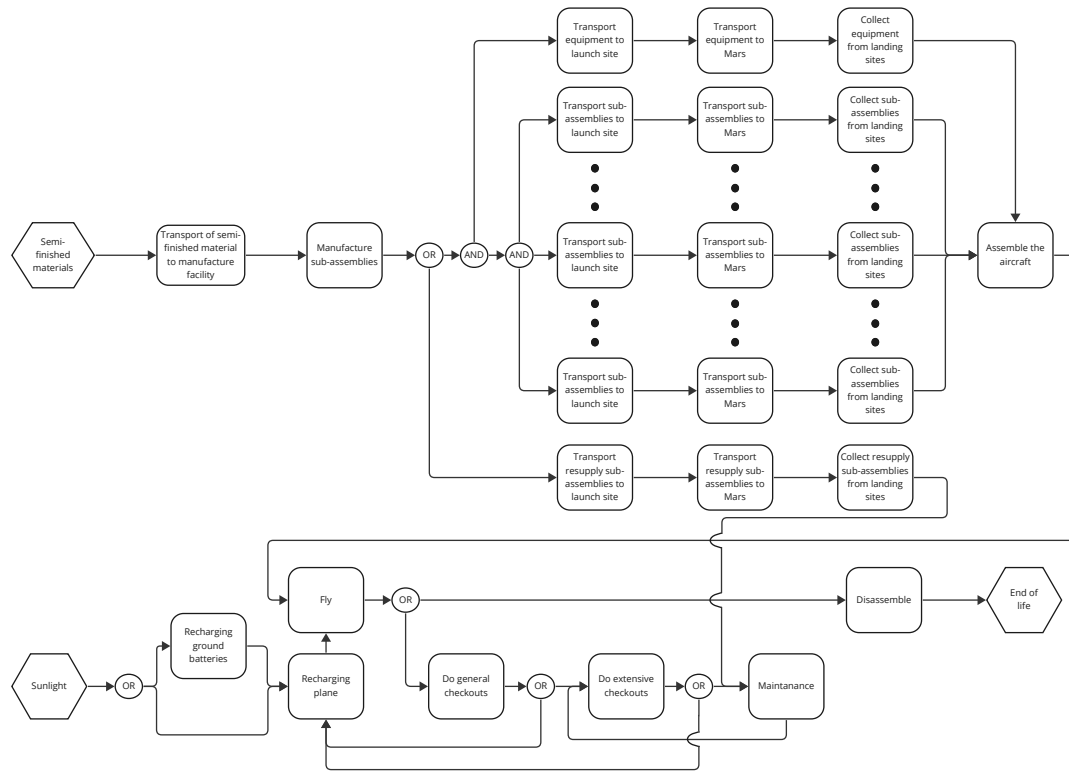


Figure 10.2: Flow chart which describes the operations and logistics for the production and operation phase.

Additionally, the sub-assemblies that are transported from Earth need to be checked for possible damage due to transportation.

There is no infrastructure necessary for the flight itself. However the turnaround time will on average(average yearly solar irradiance and average latitude) be 10 hours when the solar panels are used for recharging. In order to decrease the turnaround time an additional charging system can be implemented.

After the operational life of the design is over it will enter the end of life stage. In this stage the aircraft will be recycled for use on Mars. The batteries can be used for base energy storage. The engines can be used to drive a rover or for on base purposes. The body of the design can be used as a shed for environmental pressurized storage. Finally the wings and blades could be used as beams in the construction of the base. Other parts of the aircraft will also have their purpose in the base on Mars.

10.3. N^2 charts

By Patrick Kostelac, Javier Alonso

The N^2 chart is a diagram in the shape of a matrix, representing the functional and physical interfaces between system elements. In the design phase, the N^2 chart is used to determine the inter dependencies of each system. The outputs of each system are presented on the horizontal axis and the inputs of each system are presented on the vertical axis. This way, the key subsystems can be identified as those which influence multiple other subsystems. Subsequently, the chart can be used to identify further risks. Some subsystems are dependent on many other subsystems and thus their design can be significantly constrained.

New table

- Flight path - Incoming communications with satellites/base	- External temperature -Airspeed -Current location					-State of the external structure	
Communications		-Required turn radius		-Required power for communications			-Outgoing communications with satellites/base -Periodic status reports to base
-Possible failure report -Current location	Sensing	-Required attitude change -Need to transition between T/O and cruise configuration	-Need to transition between T/O and cruise configuration -Incoming airspeed -Speed of sound	-Required power from sensors -Solar irradiance	-Required temperature change of the batteries, payload and engines -External temperature	-	
	-Current attitude	Stability and control	- Required thrust vector - Required thrust level	- Required power to move control surfaces -Required power to tilt the rotors		-Control surfaces movement	
	-Rotor's rotational speed -Rotor's orientation	-Maximum achievable thrust	Propulsion	- Required rotor power for T/O, cruise and manoeuvring -Required energy capacity		-Rotor-induced vibrational loads, axial loads and moments	
	-Battery levels -Expected remaining range -Expected recharge time		-Maximum available power	Power	-Optimum battery temperatures -Maximum available power		
	-Current temperature of the batteries, payload and engines			-Required power for heating/cooling	Thermal control	-Induced thermal loads Opening/closing of vents for cooling/heating	
	-Structural integrity -Current fatigue levels				-Absorptivity and emissivity of the aircraft	Structures	-Need to do repairs/maintenance

Figure 10.3: N^2 chart of the system in operation

10.4. Work Breakdown Structure

By Freek Braspenning, Patrick Kostelac

The Work Breakdown Structure (WBS) for the final report is set up as can be seen in Figure 10.4. The WBS for the final report goes into the lower-level tasks. The WBS is built up from the Work Flow Diagram (WFD) as it takes the same higher-level tasks. These higher-level tasks form the work packages which are further divided into sub-tasks. The workload for each task is then estimated and a team member is assigned. The initials of the group members responsible for each task are presented alongside the total estimated task duration (in man work hours). In case the entire group is responsible for the task, Group is written instead of the mentioning every name. The final output of the DSE is the final symposium presentation.

10.5. Work Flow Diagram

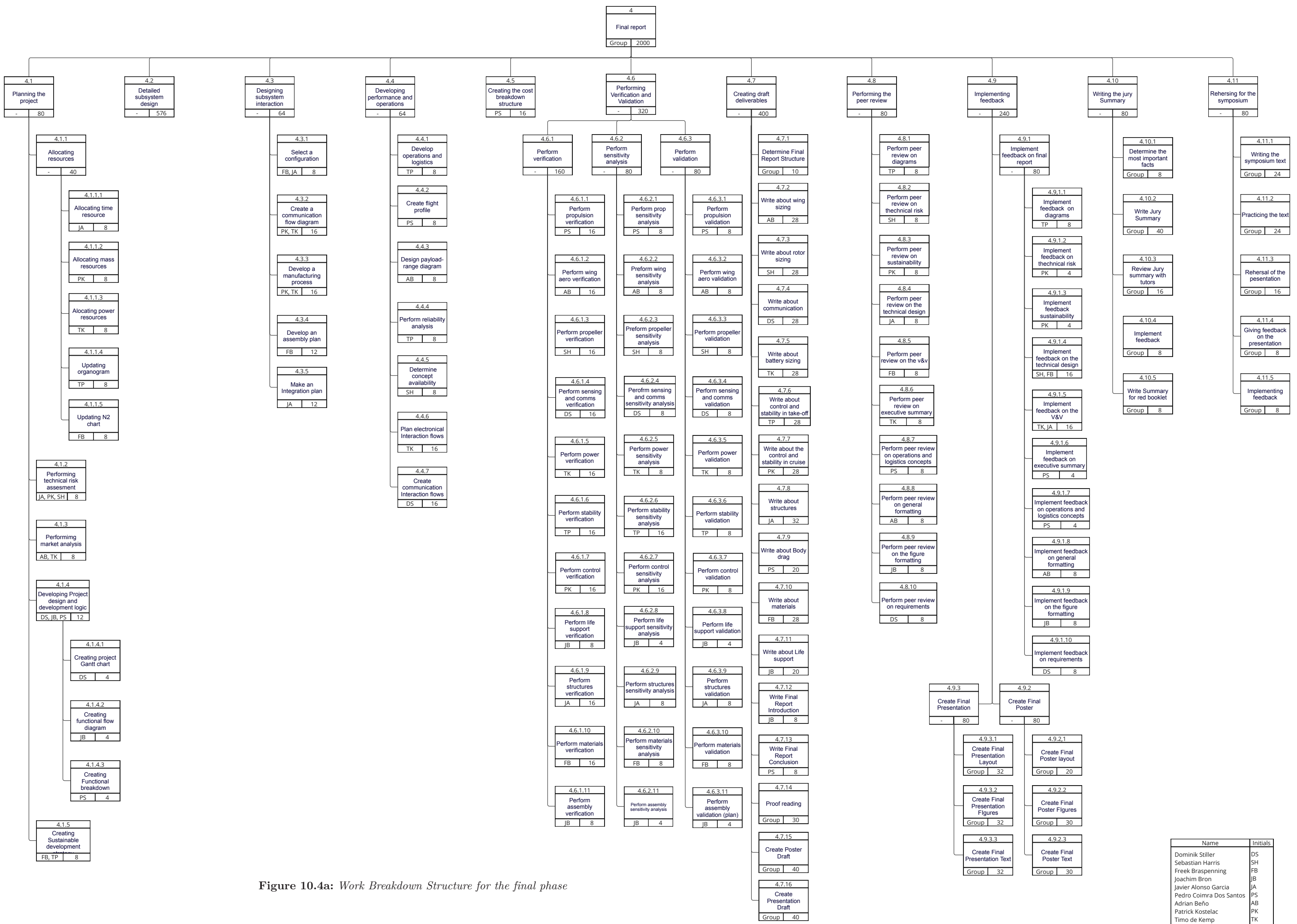
By Freek Braspenning, Patrick Kostelac

A detailed WFD for the final phase of the project was created and can be seen in Figure 10.5. The midterm report serves as a starting point for the final phase of the report. The WFD shows the tasks up to the second order of precision. The tasks which can be done simultaneously are presented in parallel and the tasks which need to be performed sequentially are presented in series.

10.6. Gantt chart

By Javier Alonso

The Gantt chart in Figure 10.6 will show how the tasks from the WBS in time. This will prove very useful for project management reasons. The Gantt chart shows a detailed work distribution for each day. This reduces the amount of non useful work done as well as increases the overall productivity of the team. The Gantt chart is designed to have tasks that are no smaller than 4 hours.



Name	Initials
Dominik Stiller	DS
Sebastian Harris	SH
Freek Braspenning	FB
Joachim Bron	JB
Javier Alonso Garcia	JA
Pedro Coimbra Dos Santos	PS
Adrian Beño	AB
Patrick Kostelac	PK
Timo de Kemp	IK
Thomas van de Pavoordt	TP

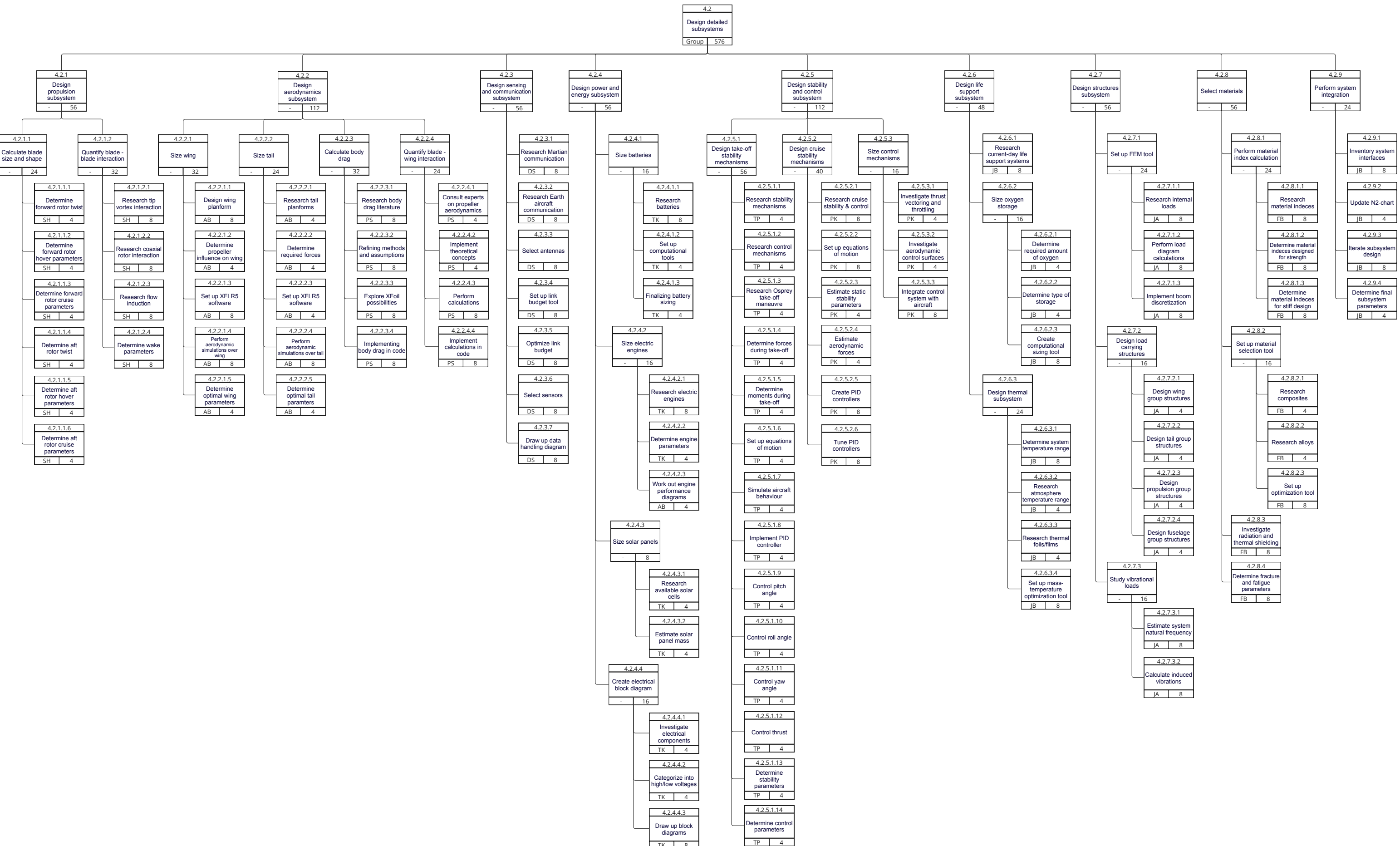


Figure 10.4b: Sub-Work Breakdown Structure for the detailed subsystem design

Name	Initials
Dominik Stiller	DS
Sebastian Harris	SH
Freek Braspenning	FB
Joachim Bron	JB
Javier Alonso Garcia	JA
Pedro Colma Dos Santos	PS
Adrian Beno	AB
Patrick Kostelac	PK
Timo de Kemp	TK
Thomas van de Pavoordt	TP

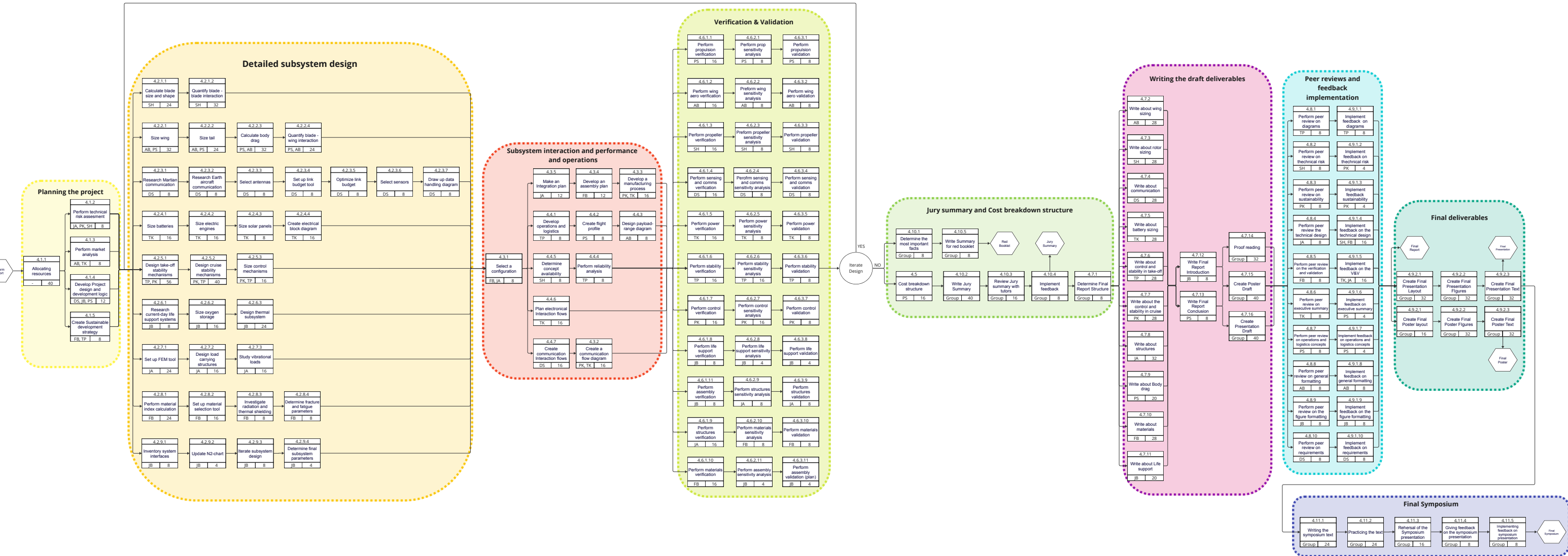
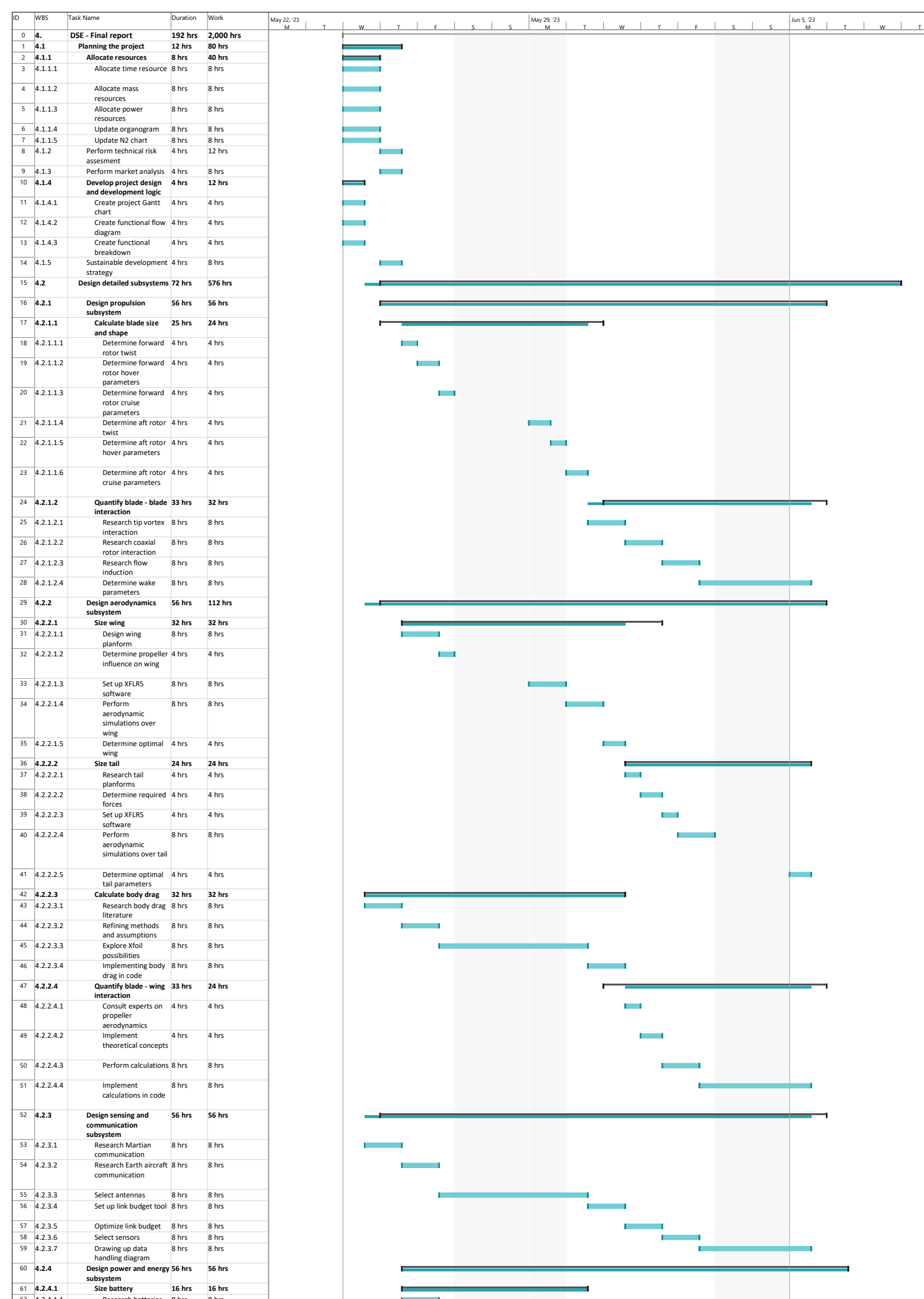
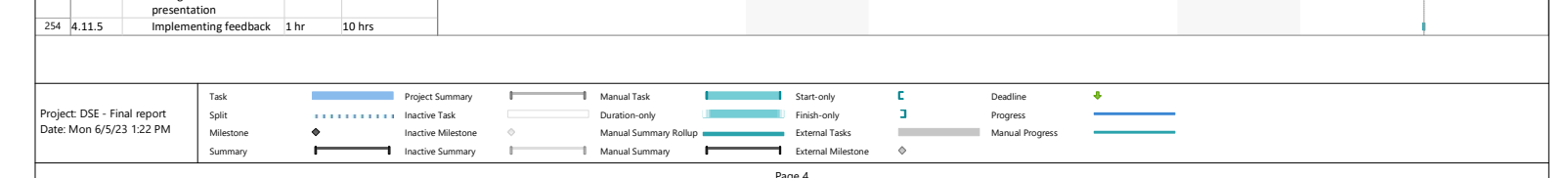
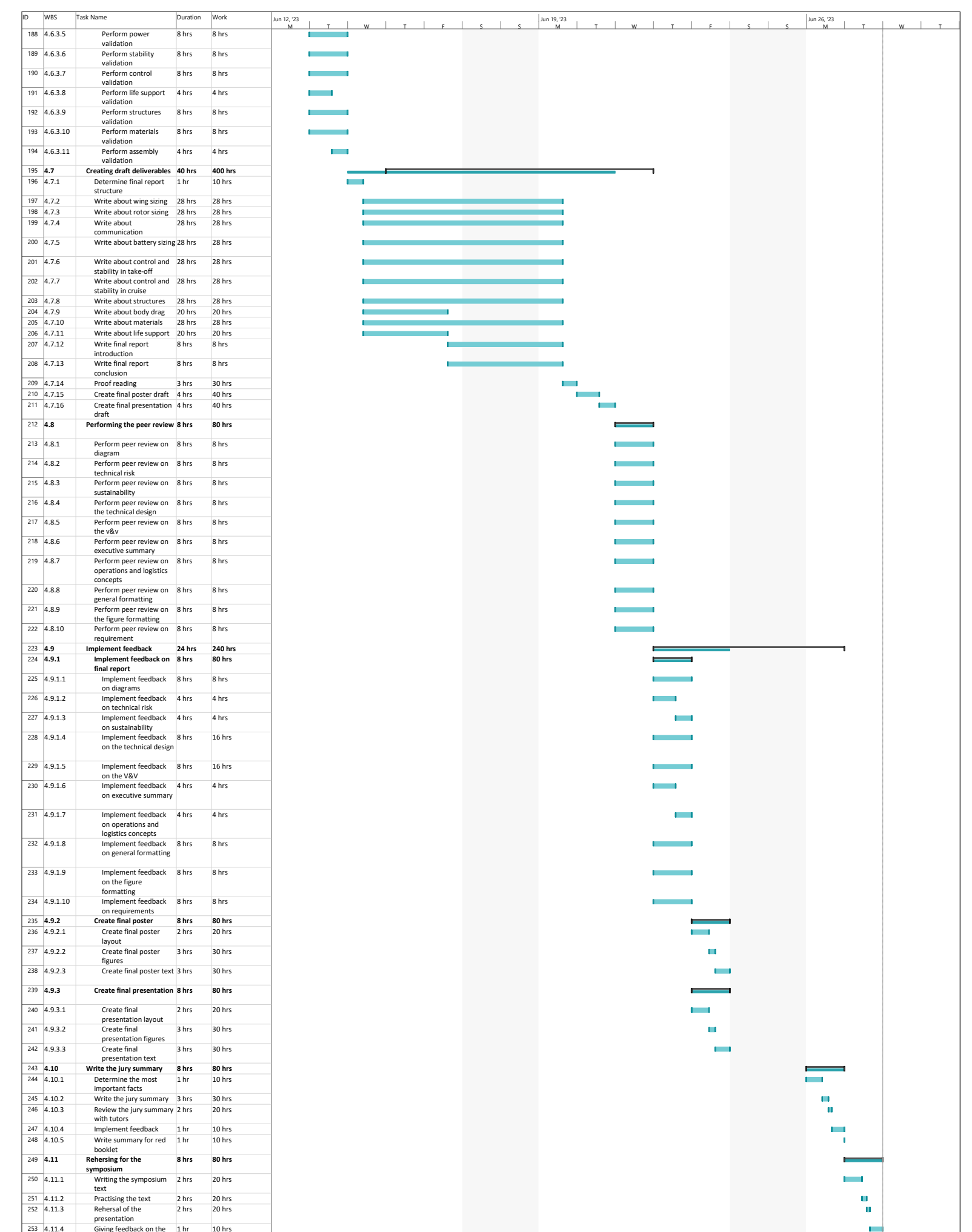
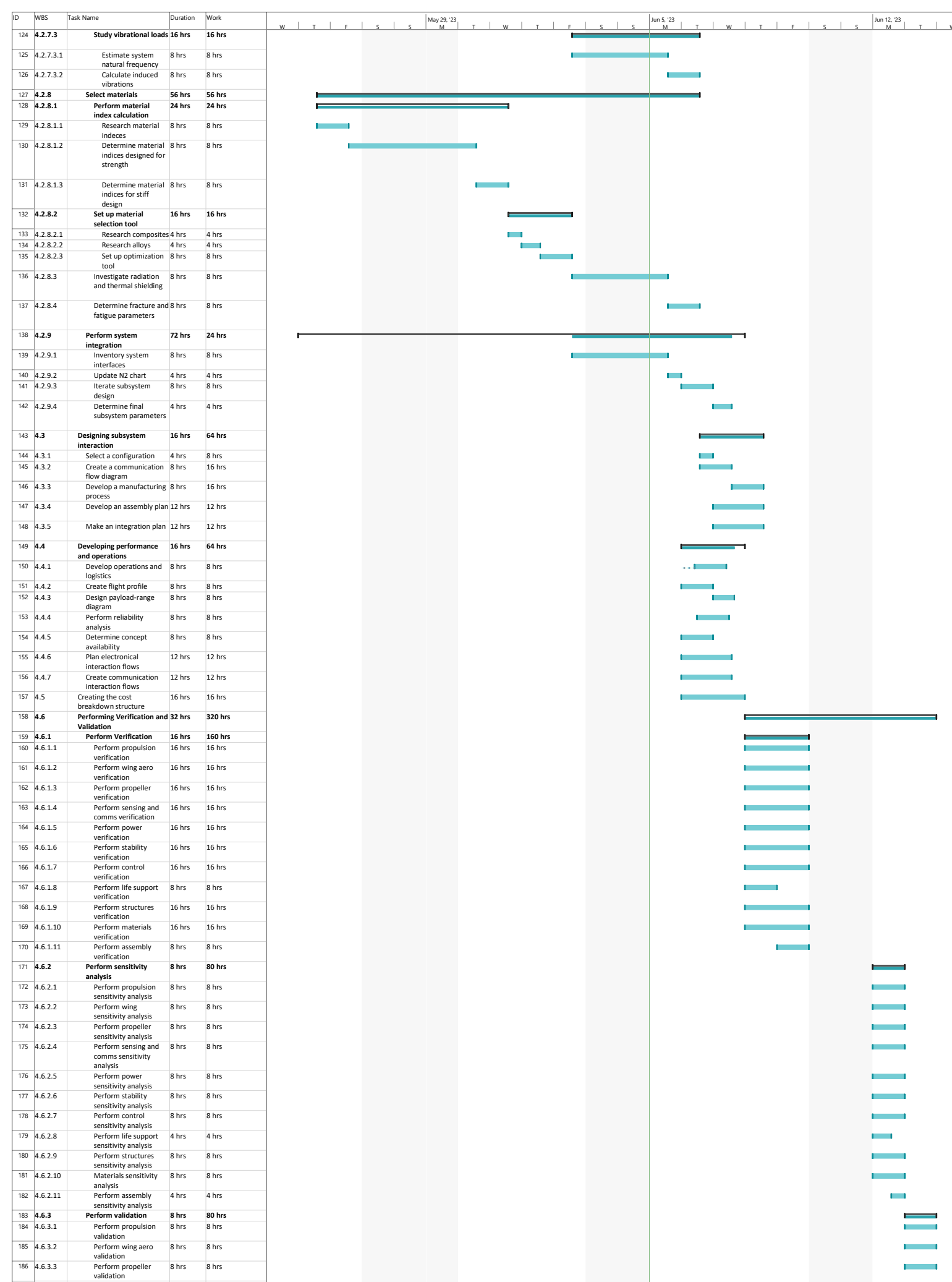


Figure 10.5: Work Flow Diagram for the final phase

Name	Initials
Dominik Stiller	DS
Sebastian Harrer	SH
Felix Schmidinger	FS
Joachim Bron	JB
Javier Alonso Garcia	JA
Pedro Alonso Dos Santos	PS
Adrian Befo	AB
Peter Grotz	PG
Timo de Kemp	TK
Thomas den Pavoordt	TP





Bibliography

- [1] Yuasa, S., and Isoda, H., "Carbon dioxide breathing propulsion for a Mars airplane," *25th Joint Propulsion Conference*, American Institute of Aeronautics and Astronautics, Monterey, CA, U.S.A., 1989. doi:10.2514/6.1989-2863.
- [2] Wickman, J., "In-Situ Mars Rocket and Jet Engines Burning Carbon Dioxide," *AIAA*, Vol. 99, No. 2409, 1999. doi:10.2514/6.1999-2409.
- [3] Pratt & Whitney, "F135-PW-600 - The World's Most Advanced Fighter Engine," , 2022.
- [4] Svoboda, C., "Turbofan engine database as a preliminary design tool," *Elsevier Science Ltd.*, 2004.
- [5] Torenbeek, E., *Synthesis of subsonic airplane design: an introduction to the preliminary design, of subsonic general aviation and transport aircraft, with emphasis on layout, aerodynamic design, propulsion, and performance*, Delft University Press ; Nijhoff ; Sold and distributed in the U.S. and Canada by Kluwer Boston, Delft : The Hague : Hingham, MA, 1982.
- [6] Selig, M. S., and Guglielmo, J. J., "High-Lift Low Reynolds Number Airfoil Design," *Journal of Aircraft*, Vol. 34, No. 1, 1997, pp. 72–79. doi:10.2514/2.2137.
- [7] Seshagiri, A., Cooper, E., and Traub, L. W., "Effects of Vortex Generators on an Airfoil at Low Reynolds Numbers," *JOURNAL OF AIRCRAFT*, Vol. 46, No. 1, 2009. doi:10.2514/1.36241.
- [8] Traub, L. W., Botero, E., Waghela, R., Callahan, R., and Watson, A., "Effect of Taper Ratio at Low Reynolds Number," *JOURNAL OF AIRCRAFT*, Vol. 52, No. 3, 2015. doi:10.2514/1.C032559.
- [9] Traub, L. W., "Aerodynamic Impact of Aspect Ratio at Low Reynolds Number," *JOURNAL OF AIRCRAFT*, Vol. 50, No. 2, 2013. doi:10.2514/1.C031980.
- [10] Gross, J., and Traub, L. W., "Experimental and Theoretical Investigation of Ground Effect at Low Reynolds Numbers," *JOURNAL OF AIRCRAFT*, Vol. 49, No. 2, 2012. doi:10.2514/1.C031595.
- [11] Somerville, A., Marino, M., Baxter, G., and Wild, G., "Understanding box wing aircraft: essential technology to improve sustainability in the aviation industry," *Aviation*, Vol. 20, No. 3, 2016. doi:10.3846/16487788.2016.1195076.
- [12] Vos, R., "Lecture Notes AE1222-II – A/C preliminary sizing(class I weight estimation method)," , Feb. 2021.
- [13] Raymer, D. P., French, J., Finger, D. F., Gomez, A., Singh, J., Pillai, R. G., Monjon, M. M., Marcos De Souza, J., and Levy, A., "The Raymer Manned Mars Airplane: A Conceptual Design and Feasibility Study," *AIAA Scitech 2021 Forum*, American Institute of Aeronautics and Astronautics, VIRTUAL EVENT, 2021. doi:10.2514/6.2021-1187.
- [14] Prouty, R. W., *Helicopter performance, stability, and control*, R.E. Krieger Pub. Co, Malabar, Fla, 1990.
- [15] Anderson, J. D., *Fundamentals of aerodynamics*, sixth edition ed., McGraw-Hill series in aeronautical and aerospace engineering, McGraw Hill Education, New York, NY, 2017.
- [16] Horiba, T., Maeshima, T., Matsumura, T., Koseki, M., Arai, J., and Muranaka, Y., "Applications of high power density lithium ion batteries," *Journal of Power Sources*, Vol. 146, No. 1-2, 2005, pp. 107–110. doi:<https://doi.org/10.1016/j.jpowsour.2005.03.205>.
- [17] Withrow, S., Johnson, W., Young, L. A., Cummings, H., Balaram, J., and Tzanatos, T., "An Advanced Mars Helicopter Design," *ASCEND 2020*, American Institute of Aeronautics and Astronautics, Virtual Event, 2020. doi:10.2514/6.2020-4028.
- [18] Koning, W. J., Johnson, W., and Allan, B. G., "Generation of mars helicopter rotor model for comprehensive analyses," Tech. Rep. ARC-E-DAA-TN50660, 2018.

- [19] Kaya, D., and Kutay, A., "Aerodynamic Modeling and Parameter Estimation of a Quadcopter Helicopter," *AIAA Atmospheric Flight Mechanics Conference*, 2014, p. 28.
- [20] Coleman, C. P., "A survey of theoretical and experimental coaxial rotor aerodynamic research," Tech. Rep. NASA-TP-3675, 1997.
- [21] "15 - Fibre-polymer composites for aerospace structures and engines," *Introduction to Aerospace Materials*, edited by A. P. Mouritz, Woodhead Publishing, 2012, pp. 338–393. doi:<https://doi.org/10.1533/9780857095152.338>.
- [22] Batrakov, A., Kusyumov, A., Mikhlov, S., and Pakhov, V., "Helicopter Fuselage Drag - Combined CFD and Experimental Studies," *EUCASS Proceedings Series*, Vol. 7, No. 2015, 2015, pp. 21–32. doi:<https://doi.org/10.1051/eucass/201507021>.
- [23] El-Gaaly, T., McMahan, B., and El Qursh, A., "Multi-Segment Zeppelin-Aided Robotic Rover For Ground-Based and Atmospheric Exploration," *Concepts and Approaches for Mars Exploration*, Vol. 4278, 2012.
- [24] Vega, G., Paeres, D., Forteza, E., Claudio, E., Marcial, D., and Araya, G., "Aerodynamic assessment of a drone dirigible-based carrier for search and research purposes," *AIAA SciTech Forum*, 2023. doi:10.2514/6.2023-1735.
- [25] Li, Y., Nahon, M., and Sharf, I., "Airship dynamics modeling: A literature review," *Progress in Aerospace Sciences*, Vol. 47, No. 3, 2011, pp. 217–239. doi:[10.1016/j.paerosci.2010.10.001](https://doi.org/10.1016/j.paerosci.2010.10.001).
- [26] Bardera, R., Sor, S., and García-Magariño, A., *Aerodynamics of Mars 2020 Rover Wind Sensors*, IntechOpen, 2020. doi:[10.5772/intechopen.90912](https://doi.org/10.5772/intechopen.90912).
- [27] Ma, R., Zhong, B., and Liu, P., "Optimization design study of low-Reynolds-number high-lift airfoils for the high-efficiency propeller of low-dynamic vehicles in stratosphere," *Science China Technological Sciences*, Vol. 53, No. 10, 2010, pp. 2792–2807. doi:[10.1007/s11431-010-4087-0](https://doi.org/10.1007/s11431-010-4087-0).
- [28] Group, J. I., *Jane's all the world's aircraft 2021-2022*, 112th ed., Jane's, Coulsdon, 2021.
- [29] Haberle, R. M., Clancy, R. T., Forget, F., Smith, M. D., and Zurek, R. W. (eds.), *The Atmosphere and Climate of Mars*, 1st ed., Cambridge University Press, 2017. doi:[10.1017/9781139060172](https://doi.org/10.1017/9781139060172).
- [30] Koning, W. J., "Airfoil Selection for Mars Rotor Applications," Tech. Rep. ARC-E-DAA-TN70055, 2019.
- [31] Hirshorn, S. R., "NASA Systems Engineering Handbook," Tech. Rep. NASA SP-2016-6105 Rev2, 2016.
- [32] Butenugro, J. A., Bahrami, M., Abenojar, J., and Martínez, M. A., "Recent Progress in Carbon Fiber Reinforced Polymers Recycling: A Review of Recycling Methods and Reuse of Carbon Fibers," *Materials*, Vol. 14, No. 21, 2021, p. 6401. doi:[10.3390/ma14216401](https://doi.org/10.3390/ma14216401).
- [33] Burroughs, L. R., "Study of helicopter transmission system development testing," Tech. rep., Jun. 1968.
- [34] Keonian, E., Sumerlin, W., Tall, M., Bussolini, J., and Baker, B., "Reliability of Avionics Systems." Tech. rep., Jul. 1971.
- [35] Leishman, J., "Rotorcraft Brownout Advanced Understanding, Control, and Mitigation," Tech. rep., Oct. 2014.
- [36] Eshima, S., and Nabity, J., "Failure Mode and Effects Analysis for Environmental Control and Life Support System Self-Awareness," 2020.
- [37] Dejogn, C., Wolbrink, A., and Larcher, J., "In-flight medical incapacitation and impairment of airline pilots." *Aviation, Space and Environmental Medicine*, Vol. 77, 2006, pp. 1077–9.
- [38] Brundtland, G. H., *Report of the World Commission on environment and development: Our Common Future*, UN, 1987.